

Interaction of Confined Polaritons in Microcavity Structures

Présentée le 23 mars 2021

Faculté des sciences de base
Laboratoire en semiconducteurs avancés pour la photonique et l'électronique
Programme doctoral en photonique

pour l'obtention du grade de Docteur ès Sciences

par

Morteza NAVADEH TOUPCHI

Acceptée sur proposition du jury

Prof. O. Martin, président du jury
Dr M. Portella Oberli, Dr D. Oberli, directeurs de thèse
Prof. L. Vina, rapporteur
Prof. M. Wouters, rapporteur
Prof. C. Galland, rapporteur

Dedicated affectionately to my parents

ABSTRACT

A polariton is a quasiparticle formed from the coupling of a confined photon in a cavity to electronic excitation, like exciton in a semiconductor. This dissertation reports on series of experiments in confined polariton interaction by design, fabrication, and characterization of semiconductor microcavity structures operating in strong or weak coupling regime.

In the first part of the thesis, we mainly concentrate on the optical study of the 2D microcavity sample, including spin-dependent lower-upper polariton cross interactions by pump-probe spectroscopy technique, supported by theoretical analyses and numerical simulations based on Gross-Pitaevskii equations. In particular, we present a scattering resonance behavior via an exciton molecule (biexciton) when polaritons from both the upper and lower branches with anti-parallel spins are involved through a polaritonic cross Feshbach resonance. This demonstration will permit the control of the polariton interbranch scattering.

The second part of the thesis is dedicated to the design and fabrication of the potentials where the photonic part of polaritons is confined laterally by adjusting the thickness of the cavity layer locally in so-called mesa structures. By engineering a periodic lattice of mesas on a two-dimensional microcavity, it is possible to couple confined polariton modes of nearby mesas to establish an optical lattice analogous to the crystalline semiconductors' electronic band structures. We especially demonstrate the localization of light with a lasing mode at the edge of the Brillouin zone in a two-dimensional triangular lattice. We produce a self-trapping of light by optically inducing a local breaking of the strong-coupling regime of excitons to photons. In the weak coupling regime, we control the confined modes by the shape of the generated defect. We also reveal a controllable localization degree and experimental signature of the Anderson localization in microcavity polaritons by inducing positional disorder in the triangular lattice.

The last part is devoted to the fabrication of sub-micron size mesas to enhance polariton interaction by confining them tightly and discuss the quantum correlation of polaritons by a Hanbury Brown and Twiss (HBT) setting toward polariton blockade.

Key Words: semiconductor, microcavity, polariton, exciton, biexciton, Feshbach resonance, pump-probe spectroscopy, localization, photon lasing, Anderson localization, polariton blockade, second-order correlation, light-matter interaction, strong coupling, weak coupling, fabrication.

RÉSUMÉ

Un polariton est une quasi-particule formée par le couplage d'un photon confiné dans une cavité à une excitation électronique, comme l'exciton dans un semi-conducteur. Cette thèse rend compte d'une série d'expériences sur l'interaction des polaritons confinés par la conception, la fabrication et la caractérisation de structures de microcavités de semi-conducteurs fonctionnant en régime de couplage fort ou faible.

Dans la première partie de la thèse, nous nous concentrons principalement sur l'étude optique de l'échantillon de microcavité 2D, y compris les interactions croisées entre les polaritons inférieurs et supérieurs dépendant du spin par la technique de spectroscopie pompe-sonde, soutenue par des analyses théoriques et des simulations numériques basées sur les équations de Gross-Pitaevskii. En particulier, nous présentons un comportement de résonance de diffusion via une molécule d'exciton (biexciton) lorsque les polaritons des branches supérieure et inférieure avec des spins antiparallèles sont impliqués par une résonance de Feshbach croisée polaritonique. Cette démonstration permettra de contrôler la diffusion interbranche des polaritons.

La deuxième partie de la thèse est consacrée à la conception et à la fabrication des potentiels où la partie photonique des polaritons est confinée latéralement en ajustant localement l'épaisseur de la couche de la cavité dans des structures dénomées mésas. En concevant un réseau périodique de mésas sur une microcavité bidimensionnelle, il est possible de coupler les modes de polaritons confinés des mésas proches pour établir un réseau optique analogue aux structures de bandes électroniques des semi-conducteurs cristallins. Nous démontrons en particulier la localisation de la lumière avec un mode d'émission laser au bord de la zone de Brillouin dans un réseau triangulaire bidimensionnel. Nous produisons un auto-piégeage de la lumière en induisant optiquement une rupture locale du régime de couplage fort des excitons aux photons. Dans le régime de couplage faible, nous contrôlons les modes confinés par la forme du défaut généré. Nous révélons également un degré de localisation contrôlable et une signature expérimentale de la localisation d'Anderson dans les polaritons de microcavité en induisant un désordre positionnel dans le réseau triangulaire.

La dernière partie est consacrée à la fabrication de mésas de taille sous-micrométrique pour améliorer l'interaction des polaritons en les confinant étroitement et discute de la corrélation quantique des polaritons par un réglage de Hanbury Brown and Twiss (HBT) vers le blocage des polaritons.

Mots clés : semi-conducteur, microcavité, polariton, exciton, biexciton, résonance de Feshbach, spectroscopie pompe-sonde, localisation, laser à pho-

tons, localisation Anderson, blocage de polariton, corrélation de second ordre, interaction lumière-matière, couplage fort, couplage faible, fabrication.

ACKNOWLEDGEMENTS

I feel fortunate to have been supervised by Benoit Deveaud; thank him for his support and guidance and for giving me the opportunity to work in his lab at EPFL. I would like to express my gratitude and appreciation for Marcia Portella-Oberli and Daniel Oberli, my supervisor and cosupervisor, whose guidance, endless support, and encouragement have been precious throughout this study. I am appreciative to all the members of the LOEQ for providing an intellectually stimulating and beneficial ambiance. I cordially acknowledge my thesis jury members, Luis Vina, Michiel Wouters, Christophe Galland, and Olivier Martin, for accepting my thesis. I would like to express my very great appreciation to Claire-Lyse Rouiller for her wise counsel and kindness.

I'm eternally grateful to my parents for their boundless love and ongoing support throughout my life.

Finally, to my friends and to all who have been a part of my getting there: Amir, Sogol, Ali(s), Soheil, Mehrnaz, Fatemeh, Nima, Hossein, and numerous others who deserve my eminent gratitude.

Lausanne, Autumn 2020

CONTENTS

1	INTRODUCTION	1
2	SEMICONDUCTOR CAVITY QED WITH STRONG COUPLING	3
2.1	Microcavity	3
2.2	Optical Transitions in Semiconductors	6
2.3	Excitons	7
2.3.1	Wannier Excitons in Quantum Wells	7
2.4	Strong Coupling Regime: Exciton-Polaritons	8
3	THE THEORETICAL FRAMEWORK OF POLARITONS INTERACTION	11
3.1	Hamiltonian in Exciton-Photon Basis	11
3.2	Interaction Hamiltonian in Polariton Basis	13
3.3	Spin-Dependent Interaction	14
4	SAMPLE FABRICATION	17
4.1	InGaAs Quantum Well Microcavity	17
4.2	Lateral Confinement	18
4.3	Fabrication Procedures	18
4.3.1	Photolithography	19
4.3.2	Electron-beam Lithography	19
4.3.3	Etching	21
5	POLARITONIC CROSS FESHBACH RESONANCE	23
5.1	Sample	23
5.2	Pump-Probe Experiment	24
5.3	Polaritonic Feshbach Resonance	25
5.4	Polaritonic Cross Feshbach Resonance	26
5.4.1	Experimental Results	27
5.4.2	Theoretical Model	32
5.5	Perspectives	36
5.5.1	Many-body Physics with Polaron Quasiparticles	36
5.5.2	Generation of Entangled Photon Pairs	37
6	LOCALIZATION IN POLARITONIC LATTICES	41
6.1	Sample and Experimental Setup	41
6.1.1	Sample	41
6.1.2	Experimental Setup	43
6.2	Theoretical Model	44
6.3	Sample Characterization	45
6.4	Localized Photon Lasing	49
6.5	Anderson Localisation in Microcavity Polaritons	56
6.6	Perspectives	61
6.6.1	Optically Controlled Photonic Defect	61
6.6.2	Exploration of New Physics with Disorder Localization	62

6.6.3	Polariton Multistability	62
7	QUANTUM CORRELATIONS OF CONFINED POLARITONS	65
7.1	Polariton Blockade	65
7.2	Sample	68
7.2.1	Characterization	69
7.3	Polaritons Quantum Correlation	73
7.4	Experimental Results	75
8	CONCLUSION	79
	BIBLIOGRAPHY	81

NOTATION

FREQUENTLY USED SYMBOLS

a_B^*	Bohr radius
\hat{a}_L^\dagger (\hat{a}_L)	lower polariton creation (annihilation) operator
\hat{a}_U^\dagger (\hat{a}_U)	upper polariton creation (annihilation) operator
\hat{b}^\dagger (\hat{b})	biexciton creation (annihilation) operator
\hat{c}^\dagger (\hat{c})	photon creation (annihilation) operator
\mathcal{C}	Hopfield coefficient
E	energy
\mathcal{E}_b	biexciton energy
E_{BXX}	biexciton binding energy
\mathcal{E}_c	cavity photon energy
E_g	gap energy
\mathcal{E}_{LP}	lower polariton energy
\mathcal{E}_{UP}	upper polariton energy
\mathcal{E}_x	exciton energy
E_0^S	energy of the S photon mode in an isolated mesa
E_0^P	energy of the P photon mode in an isolated mesa
F	amplitude of classical light field
\mathcal{F}	cavity finesse
f_{ext}	external field excitation
g	exciton-exciton interaction
g'	strength of excitation induced dephasing
g_{+-}	exciton-exciton interaction with anti-parallel spins
g_{bx}	exciton-biexciton coupling
g_{pae}	photon assisted exchange scattering
\mathcal{I}	inverse participation ratio (IPR)
\mathbf{k}	photon and polariton wavevector
L_c	cavity space thickness
m	rest mass
m_c	confined photon effective mass ($10^{-5}m_e$ in GaAs microcavity)
m_e	electron rest mass

m_h	hole mass
m_{LP}	lower polariton effective mass
m_{UP}	upper polariton effective mass
m_x	exciton mass
n_c	cavity spacer refractive index
n_1, n_2	refractive index
n^{pu}	pump photon density
n_R	exciton reservoir population
\hat{n}	photon number operator
\hat{p}^\dagger (\hat{p})	polariton creation (annihilation) operator
P	continuous-wave pump
P_0	condensation threshold power
Q	quality factor
\mathcal{R}	mirror reflectivity
R	exciton reservoir polariton exchange rate
U	strength of exciton-exciton interaction
U_{pp}	strength of polariton-polariton interaction
$V(r)$	potential landscape
V_m	mode volume
\mathcal{X}	Hopfield coefficient
\hat{x}^\dagger (\hat{x})	exciton creation (annihilation) operator
α_B	absorption variation
γ_B	biexciton linewidth
γ_c	photon decay rate
γ_{LP}	lower polariton decay rate
γ_p	polariton linewidth
γ_R	exciton reservoir decay rate
γ_S	tunneling energy associated to S orbital
γ_{UP}	upper polariton decay rate
γ_U	upper polariton linewidth
γ_x	exciton decay rate
γ_x^*	exciton pure dephasing rate
Γ_x	exciton population decay rate
γ_{\parallel}	tunneling energy associated with the P orbital parallel to link direction

γ_{\perp}	tunneling energy associated with the P orbital perpendicular to link direction
$\gamma_0, \gamma_1, \gamma_2$	corrective energies for photonic modes in isolated mesas
γ_3	tunneling energy associated to the coupling P_x and P_y orbital
δ	cavity-exciton detuning
$\delta\lambda_{DBR}$	reflection bandwidth
$\delta\nu_c$	linewidth of the cavity mode
$\Delta E_{U,\downarrow}$	upper polariton energy shift
ΔE_X	exciton energy shift
$\Delta\omega_L$	laser-polariton detuning
λ_c	vacuum wavelength
μ	reduced mass of the electron and hole
σ^+, σ^-	photon's circular polarizations
τ	time delay
Ω_{qm}	external and cavity fields coupling strength
Ω_R	Rabi splitting

PHYSICAL CONSTANTS

c	speed of light in vacuum, $c = 299\,792\,458\,\text{m s}^{-1}$
m_e	electron mass, $m_e = 9.1093837015(28) \times 10^{-31}\,\text{kg}$
h	Plank constant, $h = 4.135667696 \times 10^{-15}\,\text{eV s}$
ε_0	vacuum electric permittivity, $\varepsilon_0 = 8.8541878128(13) \times 10^{-12}\,\text{F m}^{-1}$

(CODATA 2018 [1])

INTRODUCTION

*I have perceived a lightning flash from Tūr. Perchance, I
will bring you a brand of glowing embers.*

— Hafez

Based on an old myth, Lucifer ("light-bringer" in Latin) fall from heaven after stealing God's peculiar creation, the Light. From ancient Greece until the quantum gold rush, humankind experienced and learned to use and control light. A myriad of technologies is based on light employment or light-matter interaction like lasers and LEDs. A polariton is the quantum of the electromagnetic field in a dielectric with mixed light and matter nature [2, 3]. In 1992, Weisbuch and Ulbrich evidenced for the first time polaritons in a GaAs planar semiconductor microcavity by increasing light-matter coupling strength with embedded quantum well inside a cavity [4]. Polaritons are composite bosons, and the hybrid light-matter nature of these quasiparticles provides nonlinear behavior due to excitonic interactions and extremely light mass because of their photonic component [5].

The excitonic interaction induces nonlinearity, which is crucial for effects such as polariton parametric amplification [6–8], polariton bistability [9] and optical switching [10]. Polaritons behave in certain limits like a non-interacting Bose gas; thus, they are considered to realize quantum condensed phases in solids. Bose-Einstein condensate of two-dimensional polaritons was demonstrated for the first time in CdTe microcavity [11]. Afterward, in GaAs [12] and at room temperature, in GaN [13] microcavity.

New research directions were sought in order to confine polaritons in a lower dimension applying diverse techniques, such as zero-dimensional micropillars [14] and one-dimensional arrays [15].

This thesis is devoted to the study of confined polariton interaction in a microcavity. The fabrication of mesa structures creates the potential for confining polaritons. The pump-probe technique, near- and far-field spectroscopy, and second-order correlation measurements are used to investigate the samples.

Chapter 2 gives a summary of the interaction between exciton and photon modes in a semiconductor microcavity. The exciton-photon coupling in the weak and strong coupling regime. We provide the fundamental properties of the excitons and the microcavity.

In chapter 3, we discuss the theoretical and experimental groundwork of spin dependant Polaritons interaction. We start by presenting the interaction Hamiltonian in the exciton-photon basis following with the polariton Hamiltonian describing their mutual interactions. We obtain the equations of motions

for the exciton-photon and polariton basis of excitonic Bloch equations (EBE) and Gross-Pitaevskii equations (GPE). We end the chapter given the spinor polariton interactions, including the biexciton state.

Chapter 4 is dedicated to the fabrication of high-quality semiconductor heterostructures and microcavity samples using standard cleanroom procedures.

In chapter 5, we study the spinor polariton interactions using polarization-dependent pump-probe spectroscopy. We discuss the upper and lower polaritons scattering via the biexciton, namely polaritonic cross Feshbach resonance. The experimental results are analyzed with the Gross-Pitaevskii equations, considering the biexciton effect. We conclude the chapter with a presentation of future studies using polaritonic cross Feshbach resonance.

In chapter 6, we present coupled polaritons in a triangular lattice landscape. The first part is about the localization due to the breaking of translational symmetry in a regular lattice. In the second part, we present localization by introducing controlled lattice disorder. The experimental results are examined and related to the prediction of the theory. The chapter ends with a perspective about future studies one polariton localization in polaritonic lattice landscapes.

Chapter 7 is devoted to tightly confined polaritons. We describe the engineered microcavity structures with sub-micron size mesas for strong confinement of polaritons. Finally, we explain the second-order correlation measurement toward the polariton blockade.

Finally, in chapter 8, we address a concluding remark.

SEMICONDUCTOR CAVITY QED WITH STRONG COUPLING

This chapter is devoted to giving a background to the interaction between exciton and photon modes in a semiconductor microcavity, namely semiconductor cavity quantum electrodynamics (QED). The strength of the interaction defines the exciton-photon coupling in two regimes: the weak coupling and the strong coupling regime. In the first section, we give the fundamental properties of the microcavity. In the second and third sections, we present the basic concepts of semiconductor excitons. We end the chapter with the description of photon-exciton interaction in the strong coupling regime.

2.1 MICROCAVITY

A microcavity is a wavelength sized optical resonator that confines light at a particular wavelength. This confinement allows semiconductor microcavity devices to interact strongly with the matter. The resonant optical modes in a microcavity have specific line-shapes, wavelength spacings, and other features. To form a confined standing wave, a longitudinal resonant mode has to have an integral number of half wavelengths that fit into the microcavity.

Since the mirrors of the resonator are not quite reflecting, the photon will stay in the resonator for a certain amount of time. Hence, the linewidth of the cavity mode ($\delta\nu_c$, the full width at half maximum linewidth in frequency domain) is defined by this photon decay rate (γ_c) where $\delta\nu_c = \gamma_c/2\pi$. A quantity related to the linewidth of the cavity is the finesse (\mathcal{F}), determined as the frequency separation between successive longitudinal cavity modes to the linewidth of a cavity mode and is connected to the mirrors reflectivities \mathcal{R} by [16]

$$\mathcal{F} = \frac{\pi\sqrt{\mathcal{R}}}{1-\mathcal{R}} \quad (2.1)$$

The finesse gives a measure of how much the cavity is close to the ideal case with delta-like resonances. Another essential feature of microcavities is the mode volume V_m , which is defined as the integral over the field intensities at different positions, normalized to unity at the maximum of the field. The figure of merit for the cavities used in cavity QED is given by Q/V_m (or Q^2/V_m for some cases), where $Q = \nu_c/\delta\nu_c$ is the quality factor of the cavity. High Q-factor increases the photon storage time, which is good per se, but in some

applications decreases the speed of operation, which is vital for information processing.

A primary requirement for strong coupling is to have a small cavity mode volume V_m , considering the fact that single-photon Rabi frequency scales as $1/\sqrt{V_m}$. This requirement pushes toward fabricating cavity with a smaller length. Nevertheless, the cavity decay rate scales inversely with the length. Hence, as cavity size decreases, the cavity finesse must increase concomitantly; accordingly, mirrors with ultra-high reflectivity are needed.

The reflectivity of metallic mirrors is limited to 99%. Preferably to obtain ultra-high reflectivity, distributed Bragg reflectors (DBRs) with reflectivity of more than 99.999% are used. DBRs are consisted of multilayers of several pairs of alternating refractive indexes of n_1 and n_2 ($n_2 > n_1$). Each DBR mirror is designed for the desired wavelength of reflection λ_c (vacuum wavelength), and the principal requirement is that the thickness of each layer is a quarter of the desired wavelength of reflection ($\lambda_c/4n_{1,2}$). In this case, the constructive interference magnifies reflection, whereas destructive interference mitigates the transmitted field. The reflectivity of each mirror depends on the number of replicated pairs and the refractive index difference between the two layers. DBR is reflective over a range of wavelengths named the stopband $\delta\lambda_{DBR}$ (reflection bandwidth), which depends on the refractive index contrast between two materials.

$$\delta\lambda_{DBR} = \frac{4\lambda_c}{\pi} \arcsin\left(\frac{n_2 - n_1}{n_2 + n_1}\right) \quad (2.2)$$

The complete microcavity structure is made of two DBRs separated by a dielectric material, called “spacer” and the whole device can be considered as a 1D photonic crystal including a central defect.

We use transfer matrix formalism [17] to elucidate the principle of the microcavity, including a GaAs cavity spacer with a center wavelength at 835 nm made up of 20 DBR pairs of GaAs/AlAs with refractive indexes of 3.556 and 2.948, respectively at 10 K. The reflectivity spectrum of a single DBR is illustrated in fig. 2.1(a). A drop in reflectivity at 818 nm corresponds to the absorption of GaAs. In fig. 2.1(b) we simulate full microcavity (λ -cavity). The microcavity highlights a dip in the reflectivity spectrum at the cavity resonance wavelength in which transmission is obtained. The width of this drop is the cavity linewidth and enables us to define the Q-factor which is about 4×10^4 . The confined electromagnetic field inside the microcavity can be seen by plotting its amplitude at the resonant wavelength fig. 2.1(c). Since the spacer layer has a higher refractive index, its maximum is in the center. Although the spacer layer confines one optical wavelength, most of the electric field penetrates the DBR layers. Defining the field penetration depth at the resonant wavelength inside both DBRs by [18]

$$L_{DBR} = \frac{\lambda_c}{2n_c} \frac{n_1 n_2}{n_2 - n_1} \quad (2.3)$$

where n_c is the refractive index of the cavity spacer. Commonly L_{DBR} is about $2\mu m$, which is much larger than cavity spacer thickness $L_c = \lambda_c/n_2 \approx 0.234\mu m$. In a microcavity with DBRs, the cavity resonance can be adjusted by varying the spacer thickness keeping the stopband defined by the DBRs. This feature is useful for cavity detuning and also for designing patterned cavities.

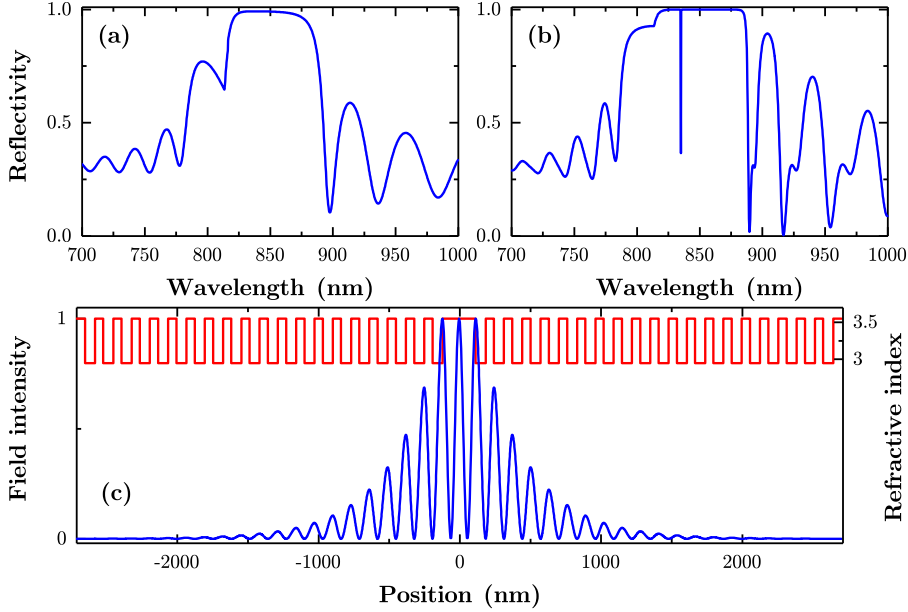


FIGURE 2.1: **Calculated reflectivity and electric field intensity using transfer matrix formalism.** (a) Reflectivity spectrum of a single 20 DBR pairs of GaAs/AlAs. (b) The reflectivity of a full microcavity (λ -cavity) highlighting a dip in the reflectivity spectrum at the cavity resonance wavelength (835 nm). (c) In z-direction, the variation of the refractive index (red) and the electric field intensity (blue).

We can decompose the photon wavevector \mathbf{k} into the in-plane \mathbf{k}_{\parallel} and perpendicular \mathbf{k}_{\perp} components, respecting the DBRs so that $\mathbf{k}^2 = \mathbf{k}_{\parallel}^2 + \mathbf{k}_{\perp}^2$. \mathbf{k}_{\perp} represents the mode quantization in the cavity by having $|\mathbf{k}_{\perp}| = 2\pi n_c/\lambda_c$. The energy of a photon in a cavity with $|\mathbf{k}_{\perp}| \gg |\mathbf{k}_{\parallel}|$ approximation reads [18]

$$E_c(\mathbf{k}_{\parallel}) = \frac{\hbar c}{n_c} \sqrt{|\mathbf{k}_{\parallel}|^2 + |\mathbf{k}_{\perp}|^2} \simeq E_c(\mathbf{k}_{\parallel} = 0) + \frac{\hbar^2 |\mathbf{k}_{\perp}|^2}{2m_c} \quad (2.4)$$

Where $E_c(\mathbf{k}_{\parallel} = 0) = \hbar c/\lambda_c$ and $m_c = \hbar n^2/c\lambda_c$ is the effective mass of a confined photon typically on the order of $10^{-5}m_e$ (m_e is the electron rest mass) for GaAs microcavities. Eq. (2.4) shows a parabolic dispersion for confined photons.

2.2 OPTICAL TRANSITIONS IN SEMICONDUCTORS

A semiconductor is a material whose electrical conductivity lies in between metals and insulators. In a crystal, a lot of atoms with discrete electronic levels are congregating in a periodic structure to form bands. There is also the range of energies that an electron may not have, which calls gaps (E_g in fig. 2.2). Since the Fermi level falls in the bandgap in semiconductors, by sufficient excitation, an electron from the valence band moves to the conduction band and it leaves a net positive charge in the valence band, which calls a hole. The wavevector for which the bandgap is minimum divides semiconductors into direct bandgap and indirect bandgap types. If the wavevectors of electrons and holes are similar in the conduction and valence band, the semiconductor is direct bandgap like GaAs (fig. 2.2 at the Γ -point), and if they are not, it is indirect bandgap like silicon.

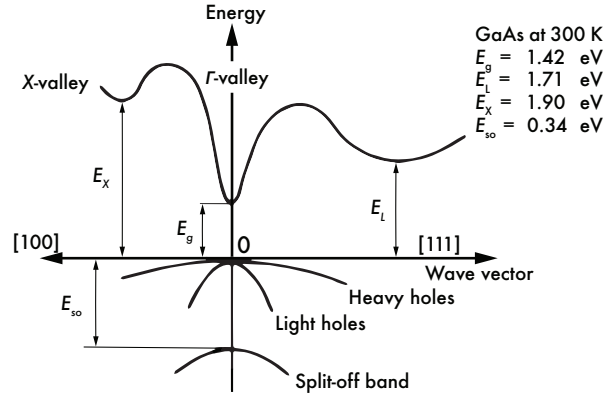


FIGURE 2.2: **Bulk GaAs band structure.** Scheme of the band structure of bulk GaAs semiconductor along the $[111]$ and $[100]$ momentum-space directions at 300 K. The conduction band is located above the degenerate heavy-hole and light-hole bands. The figure is reproduced from [19].

Fig. 2.2 shows the bandstructure of bulk GaAs. The lowest conduction band has an s-type symmetry ($l = 0$) with the total angular momentum of $J = l + s = 1/2$, which is twofold degenerate. In the valence band, two bands converging at the Γ -point. These bands are identified as the heavy-hole and light-hole; the more concave one with a smaller value of $(d^2E/dk^2)^{-1}$ (it is proportional to the effective mass), is the light hole band, and the other one is the heavy hole band. The valence band orbitals have p-type symmetry ($l = 1$). The spin-orbit interaction splits the p-type state into the valence band $J = l + s = 3/2$ ($J_z = \pm 3/2$ heavy hole and $J_z = \pm 1/2$ light hole with fourfold degeneracy) and $J = l - s = 1/2$ (split-off band with twofold degeneracy). An interband optical excitation moves an electron to an s orbital of the conduction band, leaving a hole in a p orbital of the valence band.

2.3 EXCITONS

Upon adequate excitation energy, a Coulomb correlated electron-hole pair is created in a semiconductor called an exciton. This neutral quasiparticle has a close analogy to the hydrogen atom with a corresponding Bohr radius and binding energy. There are two major types of excitons Wannier-Mott and Frenkel. The latter has much larger binding energy and a much smaller Bohr radius than the former, which is the case in semiconductors like GaAs and GaN. Wannier-Mott excitons can be described by a two-body Schrödinger equation similar to the hydrogen-like atoms with the electron and hole effective masses and a screened Coulomb interaction. To solve this equation, one can assume the envelope wave function as the product of wave functions of the center of masses and the relative motion of the electron and the hole. The center of the masses equation is like a free particle with a total mass of electron and hole ($m_x = m_e + m_h$) and gives a parabolic dispersion. The equation of the relative motion is equal to the hydrogen atom problem, which offers a series of n quantized states [18, 20].

$$E_n^{3D}(\mathbf{k}) = E_g + \frac{\hbar^2 |\mathbf{k}|^2}{2m_x} - \frac{E_b^{3D}}{n^2} \quad (2.5)$$

The Bohr radius and the binding energy in the 3D case are defined as following where $\mu = (m_e^{-1} + m_h^{-1})^{-1}$ is the reduced mass of the electron and hole.

$$a_B^* = \frac{\hbar^2 \epsilon^2}{\mu e^2} \quad (2.6)$$

$$E_b^{3D} = \frac{\mu e^4}{2\epsilon^2 \hbar^2} = \frac{\hbar^2}{2\mu a_B^{*2}} \quad (2.7)$$

The electron and hole finally recombine and emit a photon with identical energy of exciton that is lower than the bandgap.

Excitons can have a total angular momentum of ± 1 and ± 2 of conduction and valence bands. They can couple to photons while having similar total angular momentum to circular polarization of light (± 1), and hence they called bright excitons, whereas the other excitons are called dark.

2.3.1 Wannier Excitons in Quantum Wells

A quantum well is a semiconductor heterostructure with varying bandgaps, where conduction and valence bands form a potential well. Free carriers or excitons are confined in one dimension (the growth direction defined as z -direction) and free to move in the other two dimensions (x - y plane). Quantum well structure is engineered by embedding a thin layer (few nanometers) of

a semiconductor among two thicker layers of another semiconductor with a larger bandgap. The quantized energies of the exciton in the quantum well are [21]

$$E_n^{2D}(\mathbf{k}) = E_g + \frac{\hbar^2 |\mathbf{k}|^2}{2m_x} - \frac{E_b^{3D}}{(n + 1/2)^2} \quad (2.8)$$

The lowest exciton state has four times the binding energy and half of the Bohr radius of a similar state in bulk. More importantly, the oscillator strength, which is a measure of coupling strength between light and an oscillating dipole (exciton), is increased by a factor of four in a quantum well due to changes in the exciton Bohr radius and the electron-hole overlap [22].

2.4 STRONG COUPLING REGIME: EXCITON-POLARITONS

To introduce a strong coupling between exciton and photon, a quantum well is placed at the antinode of the cavity electric field of a high Q-factor microcavity. A new quantum state arises if their mutual interaction outweighs the system's dissipation, called exciton-polariton.

To fulfill energy and momentum conservation, the linear photon dispersion should cross the parabolic exciton dispersion. In a microcavity with embedded quantum well, translational symmetry is broken along the growth axis, indicating that momentum conservation applies only to the in-plane wave vector. Therefore an exciton with a certain \mathbf{k}_{\parallel} interacts with a continuum of photons with the identical in-plane wave vector and any possible values of the orthogonal wave vector \mathbf{k}_z . Hamiltonian of the coupled exciton-photon system in the second quantization formalism under rotating wave approximation in \mathbf{k} space reads

$$\hat{\mathcal{H}} = \iint \frac{d^2 \mathbf{k}}{(2\pi)^2} \{ \mathcal{E}_x(\mathbf{k}) \hat{x}_{\mathbf{k}}^{\dagger} \hat{x}_{\mathbf{k}} + \mathcal{E}_c(\mathbf{k}) \hat{c}_{\mathbf{k}}^{\dagger} \hat{c}_{\mathbf{k}} + \frac{\Omega_R}{2} [\hat{x}_{\mathbf{k}}^{\dagger} \hat{c}_{\mathbf{k}} + \hat{c}_{\mathbf{k}}^{\dagger} \hat{x}_{\mathbf{k}}] \} \quad (2.9)$$

Where \mathcal{E}_x and \mathcal{E}_c are exciton and photon energy, $\hat{x}_{\mathbf{k}}^{\dagger}(\hat{c}_{\mathbf{k}}^{\dagger})$ and $\hat{x}_{\mathbf{k}}(\hat{c}_{\mathbf{k}})$ are exciton (photon) creation and annihilation operators at a given \mathbf{k} respectively and they satisfy Bose commutation relations

$$[x_i, x_j^{\dagger}] = \delta_{ij}, [x_i, x_j] = 0 \quad (2.10)$$

Ω_R is called Rabi splitting and represents the coupling strength of the exciton-photon [23]. The new eigenstates of the system are called upper polariton (UP) and lower polariton (LP) with eigenenergies

$$E_{UP,LP}(\mathbf{k}) = \frac{1}{2} [\mathcal{E}_c(\mathbf{k}) + \mathcal{E}_x(\mathbf{k}) \pm \sqrt{\delta^2 + \Omega_R^2}] \quad (2.11)$$

Where $\delta = \mathcal{E}_c(\mathbf{k}) - \mathcal{E}_x(\mathbf{k})$ is the cavity detuning. The Hamiltonian 2.9 is diagonalised with a unitary transformation of [2]

$$\begin{pmatrix} \hat{a}_{L,k} \\ \hat{a}_{U,k} \end{pmatrix} = \begin{pmatrix} \mathcal{X} & \mathcal{C} \\ -\mathcal{C} & \mathcal{X} \end{pmatrix} \begin{pmatrix} \hat{x}_k \\ \hat{c}_k \end{pmatrix} \quad (2.12)$$

Where \mathcal{C} and \mathcal{X} are the so-called Hopfield coefficients with $\mathcal{C}^2 + \mathcal{X}^2 = 1$. They are real coefficients such that $\mathcal{X} > 0$, $\mathcal{C} < 0$ and are given by

$$|\mathcal{X}|^2 = \frac{1}{2} \left(1 + \frac{\delta}{\sqrt{\delta^2 + \Omega_R^2}} \right), \quad |\mathcal{C}|^2 = \frac{1}{2} \left(1 - \frac{\delta}{\sqrt{\delta^2 + \Omega_R^2}} \right) \quad (2.13)$$

$|\mathcal{X}|^2$ and $|\mathcal{C}|^2$ show respectively the excitonic and photonic fraction of the lower polariton mode that varies with cavity detuning δ . The LP and UP energy dispersion versus the in-plane wavevector with the associated Hopfield coefficients are shown in fig. 2.3 for cavity-exciton detunings of $\delta(\mathbf{k}_{\parallel} = 0) > 0$, $\delta(\mathbf{k}_{\parallel} = 0) = 0$ and $\delta(\mathbf{k}_{\parallel} = 0) < 0$. The LP and UP effective mass follow accordingly as

$$\frac{1}{m_{LP}} = \frac{|\mathcal{X}|^2}{m_x} + \frac{|\mathcal{C}|^2}{m_c}, \quad \frac{1}{m_{UP}} = \frac{|\mathcal{C}|^2}{m_x} + \frac{|\mathcal{X}|^2}{m_c} \quad (2.14)$$

The decay rates of LP and UP are given by their respective excitonic and photonic part on the exciton and cavity photon decay rates

$$\gamma_{LP} = \gamma_x |\mathcal{X}|^2 + \gamma_c |\mathcal{C}|^2, \quad \gamma_{UP} = \gamma_x |\mathcal{C}|^2 + \gamma_c |\mathcal{X}|^2 \quad (2.15)$$

γ_x and γ_c are exciton and cavity photon decay rates, respectively.

By considering the finite lifetime of the cavity photon and excitons in quantum well and adding the corresponding decay rates to the photon ($\mathcal{E}_c(\mathbf{k}) - i\gamma_c$) and exciton ($\mathcal{E}_x(\mathbf{k}) - i\gamma_x$) energies phenomenologically, eq. (2.11) becomes [23]

$$E_{UP,LP}(\mathbf{k}) = \frac{1}{2} [\mathcal{E}_c(\mathbf{k}) + \mathcal{E}_x(\mathbf{k}) - i(\gamma_x + \gamma_c) \pm \sqrt{(\delta + i(\gamma_x - \gamma_c))^2 + \Omega_R^2}] \quad (2.16)$$

At the resonance between bare exciton and photon modes ($\delta = 0$), the energy splitting equals Ω_R , and the equal linewidth of a lower and upper polariton is defined by the arithmetic average of the exciton and cavity photon damping rates eq. (2.15). The strong coupling condition in cavity QED occurs when a finite real energy splitting is obtained $\Omega_R > |\gamma_c - \gamma_x|$ [23, 24] and it is experimentally observable when the Rabi splitting is larger than polariton linewidths $\Omega_R > (\gamma_c + \gamma_x)/2$ [25]. On the contrary, when $\Omega_R < |\gamma_c - \gamma_x|$, the square root in eq. (2.16) is purely imaginary, and the system is in weak-coupling regime.

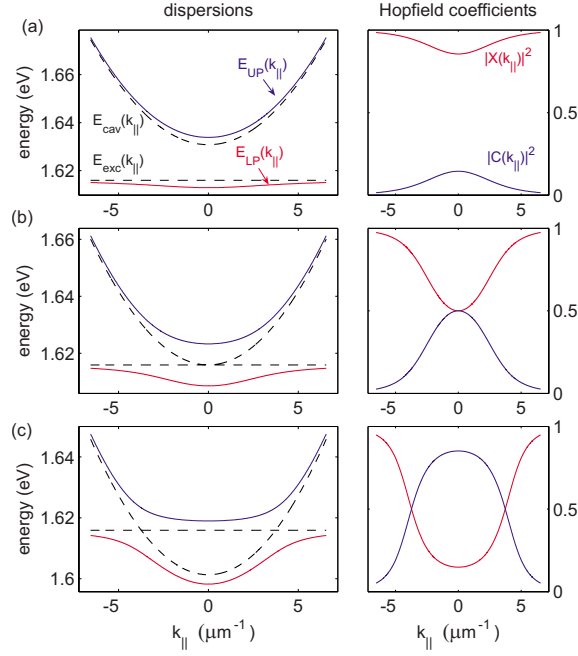


FIGURE 2.3: **LP and UP dispersion with the associated Hopfield coefficients for cavity-exciton detuning.** (a) $\delta(\mathbf{k}_{\parallel} = 0) > 0$, (b) $\delta(\mathbf{k}_{\parallel} = 0) = 0$ and (c) $\delta(\mathbf{k}_{\parallel} = 0) < 0$ [18].

In this dissertation, we will study semiconductor microcavity with exciton-photon in the strong coupling regime to study polariton interactions as well in the weak coupling regime to explore the lasing effect as in VCSELs (vertical-cavity surface-emitting lasers).

THE THEORETICAL FRAMEWORK OF POLARITONS INTERACTION

In this chapter, we discuss the theoretical and experimental groundwork of spin dependant Polaritons interaction. Quantum well excitons have two spin projection (up and down); consequently, polaritons have the same feature due to correspondence between exciton's spin and photon's polarization. Therefore, polariton-polariton spinor interaction proceeds with parallel and anti-parallel spins. We start by presenting the interaction Hamiltonian in the exciton-photon basis following with the polariton Hamiltonian describing their mutual interactions. We end the chapter given the spinor polariton interactions.

3.1 HAMILTONIAN IN EXCITON-PHOTON BASIS

In order to represent the interaction, it is crucial to start with the Hamiltonian of the system. The single particle energy and the linear coupling term between exciton and photon in real space reads.

$$\hat{\mathcal{H}}_0 = \int d\mathbf{r} \{ \mathcal{E}_x(\mathbf{k}) \hat{x}^\dagger \hat{x} + \mathcal{E}_c(\mathbf{k}) \hat{c}^\dagger \hat{c} + \frac{\Omega_R}{2} [\hat{x}^\dagger \hat{c} + \hat{c}^\dagger \hat{x}] \} \quad (3.1)$$

The interaction Hamiltonian including the exciton-exciton interaction and the phase space filling on the exciton-photon basis in real space defines as

$$\hat{\mathcal{H}}_{int} = \int d\mathbf{r} \{ \frac{1}{2} g \hat{x}^\dagger \hat{x}^\dagger \hat{x} \hat{x} - g_{pae} (\hat{c}^\dagger \hat{x}^\dagger \hat{x} \hat{x} + \hat{x}^\dagger \hat{x}^\dagger \hat{x} \hat{c}) \} \quad (3.2)$$

$\hat{x}_k^\dagger (\hat{c}_k^\dagger)$ and $\hat{x}_k (\hat{c}_k)$ are exciton (photon) creation and annihilation operators, respectively, and they satisfy Bose commutation relations

$$\begin{aligned} [\hat{x}_i, \hat{x}_j^\dagger] &= \delta_{ij}, [\hat{x}_i, \hat{x}_j] = 0 \\ [\hat{c}_i, \hat{c}_j^\dagger] &= \delta_{ij}, [\hat{c}_i, \hat{c}_j] = 0 \end{aligned} \quad (3.3)$$

The representation in real space enables us to simplify summing over all possible momentum exchanges. The interaction coefficient g represents an exciton-exciton interaction due to Coulomb exchange scattering, which touches the exchange of an electron or a hole [26–28], while g_{pae} denotes

photon assisted exchange scattering due to the fermionic composite nature of the excitons [8, 28, 29].

$$\hat{\mathcal{H}}_{pump} = \int d\mathbf{r} \Omega_{qm}(F\hat{c}^\dagger + \hat{c}F^*) \quad (3.4)$$

This Hamiltonian illustrates the resonant pumping of the system by a classical light field of amplitude F and coupling strength of Ω_{qm} between the external and cavity fields [8].

To find the time evolution of the system, the equations of motion of the operators $\hat{x}, \hat{x}^\dagger \hat{x}$ and \hat{c} with the Heisenberg equation $i\hbar\dot{\hat{x}} = [\hat{x}, \hat{\mathcal{H}}]$ should be calculated. Where $\hat{\mathcal{H}} = \hat{\mathcal{H}}_0 + \hat{\mathcal{H}}_{int} + \hat{\mathcal{H}}_{pump}$ and the operator \hat{x} must be replaced by $\hat{x}, \hat{x}^\dagger \hat{x}$ and \hat{c} . We represent the mean fields as

$$P(t) = \langle \hat{x} \rangle, N(t) = \langle \hat{x}^\dagger \hat{x} \rangle, E(t) = \langle \hat{c} \rangle \quad (3.5)$$

Which we refer to them as Polarization, Population, and photon field, respectively. Following the common mean-field approximation [30] $\langle \hat{x}^\dagger \hat{x} \hat{x} \rangle \simeq \langle \hat{x}^\dagger \hat{x} \rangle \langle \hat{x} \rangle$ and $\langle \hat{x}^\dagger \hat{x}^\dagger \rangle = \langle \hat{x} \hat{x} \rangle = 0$.

Eventually, we obtain excitonic Bloch equations (EBE) ¹

$$\begin{aligned} i\hbar\dot{N} &= -i\Gamma_x N - 2i\left(\frac{\Omega_R}{2} - 2g_{pae}N\right) \Im(PE^*) \\ i\hbar\dot{P} &= (\mathcal{E}_x - i\gamma_x + gN)P + \left(\frac{\Omega_R}{2} - 2g_{pae}N\right)E \\ i\hbar\dot{E} &= (\mathcal{E}_c - i\gamma_c)E + \left(\frac{\Omega_R}{2} - g_{pae}N\right)P - f_{ext} \end{aligned} \quad (3.6)$$

Where the external excitation field $f_{ext} = -\Omega_{qm}F$. The exciton density-dependent interaction terms' role is explicit: The photon assisted term, which represents phase space-filling, induces a reduction of the Rabi coupling while the exciton-exciton interaction term causes renormalization of exciton energy. γ_c and Γ_x represent photon and exciton population decay rate respectively. The general form of the dephasing rate of the exciton is given by

$$\gamma_x(N) = \Gamma_x/2 + g'N + \gamma_x^* \quad (3.7)$$

γ_x is dephasing rate of excitons and γ_x^* is the exciton pure dephasing rate. g' is the strength of excitation induced dephasing (EID) term, which depends on exciton density and leads to a density dependent exciton linewidth. In the coherent limit ($\gamma_x^* = g' = 0$), the time evolution of the population is given by the square of the magnitude of polarization. Hence, we can reduce EBE equations to two coupled exciton-photon Gross-Pitaevskii equations (GPE)

$$\begin{aligned} i\hbar\dot{x} &= (\mathcal{E}_x - i\gamma_x + g|x|^2)x + \left(\frac{\Omega_R}{2} - 2g_{pae}|x|^2\right)c \\ i\hbar\dot{c} &= (\mathcal{E}_c - i\gamma_c)c + \left(\frac{\Omega_R}{2} - g_{pae}|x|^2\right)x - f_{ext} \end{aligned} \quad (3.8)$$

The polarization and the photon field are replaced by x and c , respectively.

¹ $\Im(\mathcal{Z})$ is imaginary part of \mathcal{Z} .

3.2 INTERACTION HAMILTONIAN IN POLARITON BASIS

We use the Hopfield transformation as in the equation 2.12 to rewrite the Hamiltonian 3.2 in Polariton basis. The first term of the Hamiltonian becomes

$$\hat{\mathcal{H}}_{int}^{xx} = \int d\mathbf{r} \, g \left\{ \frac{1}{2} |\mathcal{X}|^4 \hat{a}_L^\dagger \hat{a}_L^\dagger \hat{a}_L \hat{a}_L + \frac{1}{2} |\mathcal{C}|^4 \hat{a}_U^\dagger \hat{a}_U^\dagger \hat{a}_U \hat{a}_U \right. \quad (3.9)$$

$$\left. + 2|\mathcal{C}|^2 |\mathcal{X}|^2 \hat{a}_L^\dagger \hat{a}_U^\dagger \hat{a}_L \hat{a}_U + \dots \right\} \quad (3.10)$$

The interaction between polariton comes from their excitonic fraction pondered by the Hopfield coefficients. Likewise, the second term of the interaction Hamiltonian transforms into

$$\hat{\mathcal{H}}_{int}^{pae} = \int d\mathbf{r} \, 2g_{pae} \{ |\mathcal{X}|^3 |\mathcal{C}| \hat{a}_L^\dagger \hat{a}_L^\dagger \hat{a}_L \hat{a}_L - |\mathcal{X}| |\mathcal{C}|^3 \hat{a}_U^\dagger \hat{a}_U^\dagger \hat{a}_U \hat{a}_U \quad (3.11)$$

$$+ 2|\mathcal{C}| |\mathcal{X}| (|\mathcal{C}|^2 - |\mathcal{X}|^2) \hat{a}_L^\dagger \hat{a}_U^\dagger \hat{a}_L \hat{a}_U + \dots \} \quad (3.12)$$

Based on equation 3.9, the exciton-exciton interaction due to Coulomb exchange scattering is repulsive for both upper and lower polariton modes. Differently, the photon-assisted exchange scattering is repulsive for lower polariton mode but attractive for the upper one (look at the signs in equation 3.11), which induces a decrease of the Rabi energy splitting. Equations 3.10 and 3.12 are contributing to the mutual interaction between lower and upper polariton modes. These cross interactions between lower and upper polaritons will be considered in detail in chapter 5. We can neglect the upper polariton state when a spectrally narrow pump resonantly excites only the lower polariton mode. Thus, reduced lower polariton Hamiltonian reads

$$\hat{\mathcal{H}}_{int}^{LP} = \int d\mathbf{r} \, \left\{ \frac{1}{2} g |\mathcal{X}|^4 \hat{a}_L^\dagger \hat{a}_L^\dagger \hat{a}_L \hat{a}_L + 2g_{pae} |\mathcal{X}|^3 |\mathcal{C}| \hat{a}_L^\dagger \hat{a}_L^\dagger \hat{a}_L \hat{a}_L \right\} \quad (3.13)$$

If we consider quasi-mode coupling Hamiltonian between the external field and the lower polariton mode with coupling strength $\Omega_{LP} = \Omega_{qm} |\mathcal{C}|$ (like in equation 3.4), the Heisenberg equation for the lower polariton mode gives Gross-Pitaevskii equation as

$$i\hbar \dot{a}_L = \left(\mathcal{E}_{LP} - i\gamma_L + g |\mathcal{X}|^4 |a_L|^2 + 4g_{pae} |\mathcal{X}|^3 |\mathcal{C}| |a_L|^2 \right) a_L - f_{ext} \quad (3.14)$$

To derive this equation, the coherent limit approximation is applied. $f_{ext} = -\Omega_{LP} F$ and γ_L is the dephasing rate of the lower polariton branch eq. (2.15).

3.3 SPIN-DEPENDENT INTERACTION

So far, we didn't consider the spin-degree of freedom in the interactions. In this section, we include the spin in the exciton-exciton interactions. As mentioned before, excitons in a quantum well can take two possible spins up and down, that can couple to the cavity photon with corresponding circular polarization. Furthermore, the coupling of two excitons with opposite spins is a new quasi-particle form called biexciton. The creation (\hat{b}^\dagger) and annihilation (\hat{b}) operator of the biexciton with energy of \mathcal{E}_b , satisfy Bose commutation rules.

Photon-assisted exchange scattering is independent of any Coulomb process, and it arises from the saturation of the exciton oscillator strength. The Pauli exclusion principle forbids the creation of another exciton at a distance shorter than the Bohr radius with the same spin. Thus the photon-assisted exchange scattering occurs between excitons and photons with parallel spins.

$$\hat{\mathcal{H}}_0 = \sum_{\sigma=\{\uparrow,\downarrow\}} \int d\mathbf{r} \{ \mathcal{E}_x \hat{x}_\sigma^\dagger \hat{x}_\sigma + \mathcal{E}_c \hat{c}_\sigma^\dagger \hat{c}_\sigma + \mathcal{E}_b \hat{b}^\dagger \hat{b} + \frac{\Omega_R}{2} (\hat{x}_\sigma^\dagger \hat{c}_\sigma + \hat{c}_\sigma^\dagger \hat{x}_\sigma) \} \quad (3.15)$$

$$\begin{aligned} \hat{\mathcal{H}}_{int} = \sum_{\sigma=\{\uparrow,\downarrow\}} \int d\mathbf{r} \frac{1}{2} \{ & g \hat{x}_\sigma^\dagger \hat{x}_\sigma^\dagger \hat{x}_\sigma \hat{x}_\sigma + g_{+-} \hat{x}_\sigma^\dagger \hat{x}_{-\sigma}^\dagger \hat{x}_{-\sigma} \hat{x}_\sigma \\ & - 2g_{pae} (\hat{c}_\sigma^\dagger \hat{x}_\sigma^\dagger \hat{x}_\sigma \hat{x}_\sigma + \hat{x}_\sigma^\dagger \hat{x}_\sigma^\dagger \hat{x}_\sigma \hat{c}_\sigma) \\ & + g_{bx} (\hat{b} \hat{x}_\sigma^\dagger \hat{x}_{-\sigma}^\dagger + \hat{x}_\sigma \hat{x}_{-\sigma} \hat{b}^\dagger) \} \end{aligned} \quad (3.16)$$

Where g_{bx} is exciton-biexciton coupling, and g_{+-} renders exciton-exciton interaction with anti-parallel spins. The Heisenberg equation of motion for the exciton, photon, and biexciton with the coherent limit assumption reads

$$\begin{aligned} i\hbar \dot{x}_\uparrow &= (\mathcal{E}_x - i\gamma_x + g|x_\uparrow|^2 + g_{+-}|x_\downarrow|^2) x_\uparrow \\ &+ g_{bx} b x_\downarrow^* + \left(\frac{\Omega_R}{2} - 2g_{pae}|x_\uparrow|^2 \right) c_\uparrow \\ i\hbar \dot{c}_\uparrow &= (\mathcal{E}_c - i\gamma_c) c_\uparrow + \left(\frac{\Omega_R}{2} - g_{pae}|x_\uparrow|^2 \right) x_\uparrow - f_{ext} \\ i\hbar \dot{b} &= (\mathcal{E}_b - i\gamma_b) b + g_{bx} x_\uparrow x_\downarrow \end{aligned} \quad (3.17)$$

Where γ_b is the biexciton linewidth. To study the effect of the biexciton on the lower-polariton mode, consider the spin-dependent Hamiltonian in the lower-polariton basis.

$$\begin{aligned} \hat{\mathcal{H}}_{int}^{LP} = \sum_{\sigma=\{\uparrow,\downarrow\}} \int d\mathbf{r} \{ & \left(\frac{1}{2} g |\mathcal{X}|^4 + 2g_{pae} |\mathcal{X}|^3 |\mathcal{C}| \right) \hat{a}_{L,\sigma}^\dagger \hat{a}_{L,\sigma}^\dagger \hat{a}_{L,\sigma} \hat{a}_{L,\sigma} \\ & + g_{+-} |\mathcal{X}|^4 \hat{a}_{L,\sigma}^\dagger \hat{a}_{L,-\sigma}^\dagger \hat{a}_{L,-\sigma} \hat{a}_{L,\sigma} \\ & + \frac{1}{2} g_{bx} |\mathcal{X}|^2 (\hat{b} \hat{a}_{L,\sigma}^\dagger \hat{a}_{L,-\sigma}^\dagger + \hat{a}_{L,\sigma} \hat{a}_{L,-\sigma} \hat{b}^\dagger) \} \end{aligned} \quad (3.18)$$

Then, the equations of motion for lower polariton in the spin-dependent case are

$$\begin{aligned}
 i\hbar\dot{a}_{L,\uparrow} &= \left(\mathcal{E}_{LP} - i\gamma_L + g|\mathcal{X}|^4|a_{L,\uparrow}|^2 + 4g_{pae}|\mathcal{X}|^3|C||a_{L,\uparrow}|^2 + g_{+-}|\mathcal{X}|^4|a_{L,\downarrow}|^2 \right) a_{L,\uparrow} \\
 &\quad + g_{bx}|\mathcal{X}|^2 b a_{L,\downarrow}^* - f_{ext} \\
 i\hbar\dot{b} &= (\mathcal{E}_b - i\gamma_b)b + g_{bx}|\mathcal{X}|^2 a_{L,\uparrow} a_{L,\downarrow}
 \end{aligned} \tag{3.19}$$

In the case of polaritons with parallel spins, the polariton interaction is repulsive ($g > 0$), and the energy of the lower polariton is renormalized to higher energy. Regarding the interaction between polaritons with antiparallel spins, it appears to be attractive ($g^{+-} < 0$) [31]. This interaction constant g^{+-} represents a background exciton-exciton interaction with antiparallel spins due to unbound continuum states referred to continuum correlations [32]. The biexciton interaction g_{bx} represents the polariton biexciton bound state's interaction. When the energy of the lower polariton is about half of the biexciton energy, a scattering resonance happens. At this resonance, an enhancement of the attractive anti-parallel spin polariton interaction and transformation to repulsive one occurs. The polaritonic Feshbach resonance was demonstrated in lower polariton scattering with biexciton [31]. In chapter 5, we will extend the interactions to lower-upper polariton to a biexciton and present the conditions and the demonstration of cross Feshbach resonance.

SAMPLE FABRICATION

In previous chapters, we reviewed the basics of light-matter interaction in the microcavities. This chapter is about the fabrication of high-quality semiconductor heterostructures and microcavity samples.

4.1 INGAAS QUANTUM WELL MICROCAVITY

*F*abrication of Fabry-Pérot resonators with a lot of different layers requires highly stable deposition conditions and precise control of the beam flux. Molecular beam epitaxy (MBE) is an epitaxial growth process involving the reaction of different thermal beams of atoms or molecules with a crystalline surface under ultra-high vacuum conditions. The quality of MBE grown epitaxial layers, especially in GaAs, has the state of the art criteria compared to the other methods [33].

GaAs and InAs have similar band structure qualitatively, but InAs has lower bandgap energy and larger lattice constant. Ternary compound material $\text{In}_x\text{Ga}_{1-x}\text{As}$, where x denotes the fraction of replaced In as Ga in the composition, empowers us to tune the bandgap by altering the x value. The larger lattice parameter of $\text{In}_x\text{Ga}_{1-x}\text{As}$ to the GaAs imposes compressive strain in the plane. Meanwhile, a large amount of In increases defects, and inhomogeneous linewidth of the exciton [34] and decreases the absorption of the emitted photons by quantum well in the surrounding GaAs. To address this concern, we use 4% of In and a rotating sample holder during the growth process to achieve lattice matching over the whole substrate [35]. The rotation of the sample holder introduces a homogeneous growth rate and reduces thickness variation on the wafer and leads to a thickness gradient that is nearly linear from the center of the wafer to the outer edge. This wedge grants us to tune the cavity energy by changing the excitation position on the sample.

The samples used in this dissertation consist of a microcavity made with a GaAs λ -spacer layer between two distributed Bragg reflector (DBR) mirrors consisting of pairs of GaAs/AlAs layers. A single InGaAs quantum well is placed in the middle of the spacer layer (fig. 4.1). The In content and the number of DBR pairs are mentioned for different samples in each chapter.

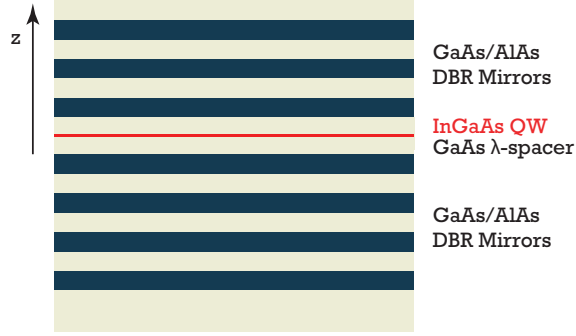


FIGURE 4.1: **Scheme of the semiconductor microcavity sample.** The growth axis is along the z -direction.

4.2 LATERAL CONFINEMENT

Polaritons in planar microcavity are free to move in the plane of the quantum well perpendicular to the growth axis. The confinement of polaritons in reduced dimensionality structures causes new features of polaritons and enhances control and interaction of them. Several techniques were developed to trap polaritons either by acting on the excitonic part like using external stress [36] or the photonic part like micropillars [37]. One feasible approach to engineer the potential where polaritons are created and confine them spatially is to alter the thickness of the cavity layer locally in so-called mesa structures. The mesa is formed by etching of the spacer layer of the half cavity after a photolithography or electron-beam lithography process with the desired layout. Photons in a mesa (more extended cavity) have lower energy concerning the neighboring part, and this means a trap for photons and thus polaritons [38]. This mesa confines the cavity photons with a diameter of 400 nm till few microns and typically 6 nm height, the lateral confinement causes the quantization of the lower and upper polariton modes in several states [39].

4.3 FABRICATION PROCEDURES

To fabricate the sample, preliminary, we design patterns with a layout editor program, and then based on the resolution that we are interested in, we can employ either photolithography or electron-beam lithography to expose structures on the half cavity (on the spacer layer without the top DBR mirror) directly or with a mask.

4.3.1 Photolithography

One fast way to expose the desired layout indirectly on the sample is to use a Cr mask. By this method, first of all, we form a pattern on a layer of light-sensitive material (photoresist), and then by selective etching, we transfer it into the underlying film (fig. 4.2). Eventually, by using a UV light and exposing the mask on top of the sample, the patterns are transferred onto the half cavity sample. The smallest feature size in this process is 650 nm.

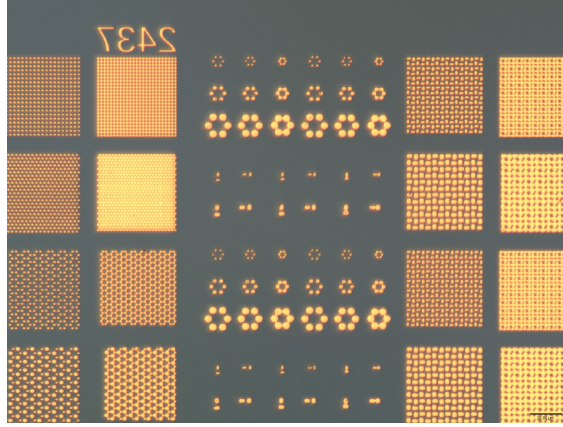


FIGURE 4.2: Image of the fabricated Cr mask used for the photolithography means.

4.3.2 Electron-beam Lithography

The most precise and high-resolution way to expose custom shapes on the half cavity sample is to use electron-beam lithography. In this method, the focused electron beam scans the sample by the electromagnetic deflection system and draw the patterns on an electron sensitive layer (we use HSQ, which is a negative tone resist with very high resolution). Like photolithography, after developing, we can remove either the exposed or non-exposed areas selectively with sub 10 nm resolution. The advantages of the electron-beam lithography are resolution and accuracy. The machine provides the length scales that are not achievable with any other lithography techniques. It can be optimized by using some strategies such as changing spot size, dose, or using different scanning procedures, but it is slower than the photolithography method.

After fabricating a single mesa successfully, we went through building an array of them or a lattice structure. The concept is to introduce interaction in a photonic crystal via polaritons. We have made different patterns like square, triangular, and disordered lattices (fig. 4.3) for various utilization.

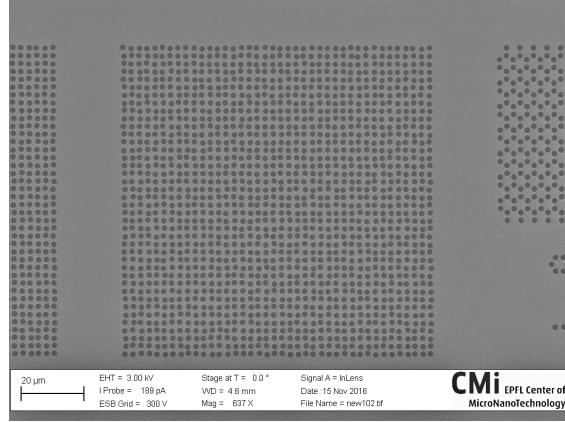


FIGURE 4.3: **SEM image of the exposed random array pattern on a developed half cavity using E-beam lithography.**

The quest for harnessing the single-polariton quantum nonlinearity in the zero-dimensional polaritonic systems, impel us to fabricate sub-micron mesa structures considering the polariton nonlinearity is scanty. Polariton-polariton interaction causes a blueshift; thus, if the blueshift is larger than the linewidth of the driving field, the presence of one polariton can hinder the absorption of another one, and the system enters the polariton blockade regime [40, 41]. To fulfill this purpose, we have designed and made a range of mesa with a width of 400 nm to 1 µm with 20 nm elevation to increase the polariton-polariton interaction (fig. 4.4).

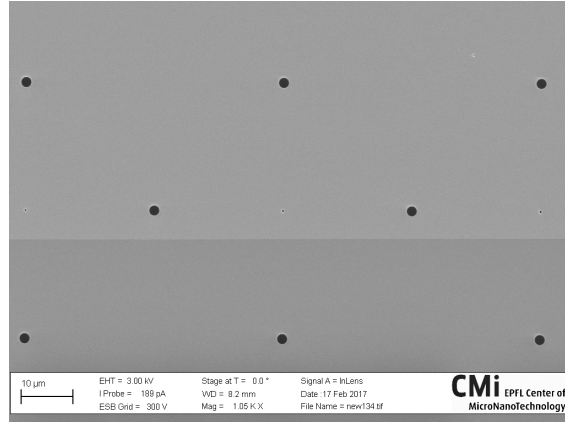


FIGURE 4.4: **SEM image of the sub-micron mesa on a developed half cavity using E-beam lithography. 500 nm mesa (at the center) is surrounded by 2µm mesas.**

4.3.3 Etching

The scheme of the fabrication process and the wet etching is represented in fig. 4.5. The half cavity sample consists of bottom DBR, embedded quantum well in a spacer layer, 1.8 nm of AlAs as an etch stop layer, and 6 nm or 20 nm of GaAs on top of that. After the lithography process is finished fig. 4.5 (a), we develop the sample fig. 4.5 (b). Then we perform the wet etching of GaAs with a 1:500 $\text{NH}_4\text{OH} : \text{H}_2\text{O}_2$ solution for 15 seconds fig. 4.5 (c). After cleaning with water, the sample is left in the air for 3 minutes to oxidize the AlAs layer. Then the AlAs layer is removed by soaking the sample into 1:1 $\text{HCl} : \text{H}_2\text{O}$ solution for one second. Lastly, the remaining photoresist is removed fig. 4.5 (d), and the sample is cleaned in the oxygen plasma chamber. We have, in this stage, the mesa structures on the spacer layer. Finally, the sample is transferred to the MBE machine to continue the growth of the top part of the sample to obtain the full microcavity fig. 4.6.



FIGURE 4.5: **Scheme of the fabrication process.** The MBE grown half-cavity: the bottom DBR and the λ -spacer layer with a single QW, with the e-beam resist on top. (a) e-beam resist deposition and e-beam exposure of the patterns. (b) developing the e-beam resist (c) wet etching (d) removing the AlAs etch-stop and e-beam resist layers.

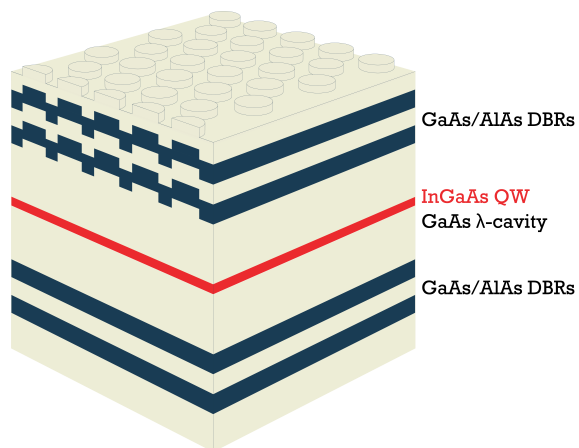


FIGURE 4.6: **Schematic of the patterned sample.** Schematic drawing of the sample with a triangular patterned structure.

The spinor character of polariton interactions offers a broad range of physics to explore; for instance, polarization multistability [42], spin switching [10], spin memory [43], and spinor stochastic resonance [44]. The formation of a molecular bound state or a biexciton, which consists of two excitons with opposite spins, performs a role in the spinor polariton interaction [27, 45]. The scattering resonance between polaritons and biexciton, named polaritonic Feshbach resonance [31], allows the modification of lower-polariton self-interactions from attractive to repulsive when tuning the energy of the two polaritons in the vicinity of the biexciton resonance. Likewise, the cross interaction between lower and upper polariton [46] gives rise a polaritonic cross Feshbach resonance [47], which opens the road for a new tool for tuning polariton interactions and go forward into quantum correlated polariton physics [48–51].

This chapter is devoted to the demonstration of polaritonic cross Feshbach resonance. The following sections concentrate on the polariton scattering via the biexciton through femtosecond polarization-dependent pump-probe spectroscopy. Initially, we describe the sample used to carry out this study, and we explain the experimental setup of the pump-probe spectroscopy. Next, we present the experimental results and theoretical model based on the spin-dependent Gross-Pitaevskii equation, including the biexciton effect. The content henceforth is adapted from the following paper [47]. Some paragraphs are reported (quasi-)verbatim.

- *Polaritonic Cross Feshbach Resonance*
M. Navadeh-Toupchi, N. Takemura, M.D. Anderson, D.Y. Oberli, and M.T. Portella-Oberli
Phys. Rev. Lett. **122**, 047402 (2019)

5.1 SAMPLE

The sample [52] under study is a III-V GaAs based microcavity with a single 8 nm $\text{In}_{0.04}\text{Ga}_{0.96}\text{As}$ quantum well embedded between top and bottom DBRs with 20 and 26.5 pairs of GaAs/AlAs, respectively fig. 5.1. The exciton energy is 1.4868 eV, and the Rabi splitting is 3.45 meV. The sample is kept at a temperature of 4 K. Since the sample is wedged, we can tune the cavity-exciton detuning by varying the laser spot across the sample. The lower and upper polaritons energy as a function of

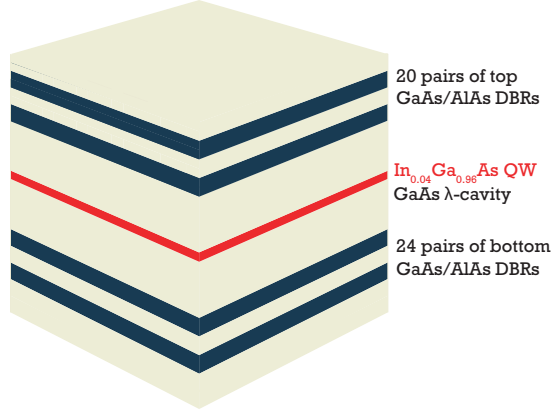


FIGURE 5.1: **The semiconductor microcavity sample scheme.** Two GaAs/AlAs DBRs intercalate a single $\text{In}_{0.04}\text{Ga}_{0.96}\text{As}$ quantum well.

cavity detuning (fig. 5.2) is obtained by observing the transmitted beam under resonant excitation of the 2D-semiconductor microcavity.

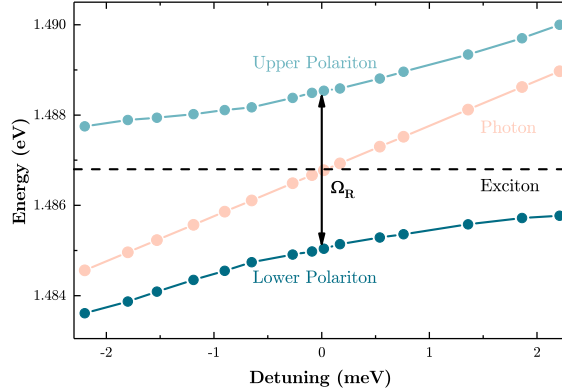


FIGURE 5.2: **Lower and upper polaritons modes of the 2D sample.** Lower (dark blue line) and upper (light blue line) polariton energy at $k = 0$ as a function of the cavity detuning. The Rabi splitting at zero detuning and bare photon (light orange line) and exciton (dash line) energies are shown.

5.2 PUMP-PROBE EXPERIMENT

Since a quantum well exciton has two spin projections of spin-up and spin-down, they coupled with photon by circular polarization σ^+ and σ^- , respectively. Therefore we can categorize polariton-polariton interaction with parallel and anti-parallel spins. The experimental arrangement of polarization-

dependent pump-probe spectroscopy consists of an almost degenerate pump and probe beams with $k_{\text{pump}} = 0$ $k_{\text{probe}} \simeq 0 \mu\text{m}^{-1}$ wave vectors, and finally, the probe beam is selected spatially by a pinhole and is sent to the spectrometer.

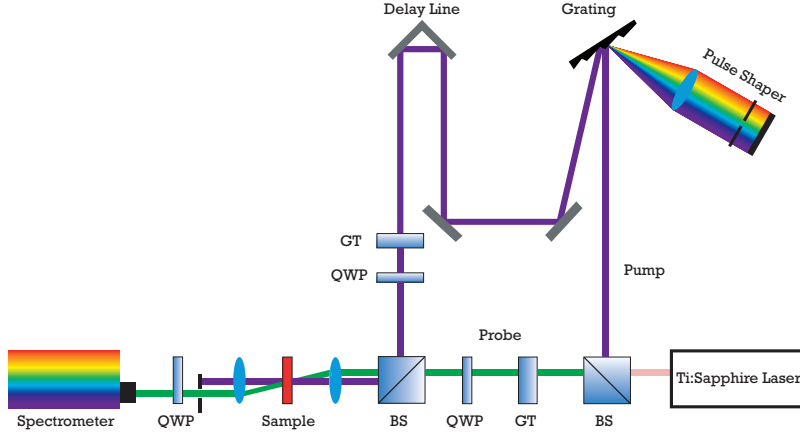


FIGURE 5.3: **Scheme of the pump-probe setup.** With the following abbreviation. BS: beam splitter, GT: Glan-Taylor Polarizer, QWP: quarter wave plate.

In fig. 5.3, the experimental setup of the pump-probe experiment is shown. Broadband (35-100 fs) TSUNAMI Ti:sapphire laser with 80 MHz repetition rate is employed. The laser beam is split into two beams of pump and probe by a beam splitter. The single grating pulse shaper remolds the broadband pump pulse (14 meV) into a narrowband pulse (to 0.5 meV), which is used to excite only the lower polariton mode and prevents the formation, by upper polariton relaxation, of an exciton population in the reservoir. In this configuration, we utilize quarter-wave plates to change the pump's and probe's polarization to the counter circular polarization of σ^+ and σ^- , respectively. The pump and probe pulses reach the sample at the time t_{pump} and t_{probe} . The time delay $\tau = t_{\text{probe}} - t_{\text{pump}}$ is defined between two pulses and sets by an optical delay stage. $\tau > 0$ ($\tau < 0$) means that the pump (probe) arrives before the probe (pump) pulse. The spectrum of the probe beam is measured in the transmission configuration.

5.3 POLARITONIC FESHBACH RESONANCE

An exciton molecule or biexciton can be defined as a bound state of two excitons with opposite spins. Because there is a one-to-one correspondence between the spin of an exciton and the polarization of the cavity photon, the spin of a polariton is described as either right or left circularly polarized photonic component.

A Feshbach resonance emerges when two interacting free particles resonantly couple to a molecular bound state. Near the resonance, the strength of the interaction between the particles is modified, and its sign changes at resonance. Since the demonstration of atomic Feshbach resonances [53], they have been widely used to control the interaction of atoms in Bose-Einstein condensates, and they have been the key to many breakthroughs in many-body quantum physics [54–57].

A polaritonic Feshbach resonance was demonstrated [31] in a semiconductor system when two lower polaritons were efficiently coupled to the biexciton. As analogous to atomic Feshbach resonance in which the energy between unbound atomic states and bound molecular state is tuned with an applied magnetic field, the energy of two polaritons with opposite spins can be tuned through the cavity detuning near the biexciton bound state energy which is slightly below the exciton energy. The experiment is done through spectrally resolved broadband femtosecond pump-probe spectroscopy. A circularly polarized pump pulse resonantly excites lower and upper polariton branches. Then, the energy shift and amplitude variation of the lower polariton resonance is measured by the transmitted counter polarized probe beam. Thus, the interaction strength was tuned by involving just lower polaritons.

5.4 POLARITONIC CROSS FESHBACH RESONANCE

A similar enhancement of the scattering strength occurs when the energy sum of the lower and upper polaritons with opposite spins matches the biexciton energy by a polaritonic cross Feshbach resonance (fig. 5.4). This demonstration will allow the control of the polariton interbranch scattering. It may initiate studies of many-body physics with polaron quasiparticles [50] and lead to the generation of entangled photon pairs via the biexciton [48, 49].

We use spectrally resolved circularly polarized pump-probe spectroscopy. The lower polaritons are excited resonantly with a circularly polarized (σ^+) narrow-band pump pulse generating a spinor lower polariton population. The cross interaction between the upper and lower polariton is probed with a counter-circular polarized (σ^-) probe pulse. We spectrally probe the energy and intensity of the upper polariton peak by measuring the transmission spectrum of the probe pulse (fig. 5.5).

The cross Feshbach resonance occurs at a negative cavity detuning energy equal to the binding energy of the biexciton (fig. 5.5 (b)), where the total energy of one lower plus one upper polariton equals the biexciton energy (fig. 5.5 (c)).

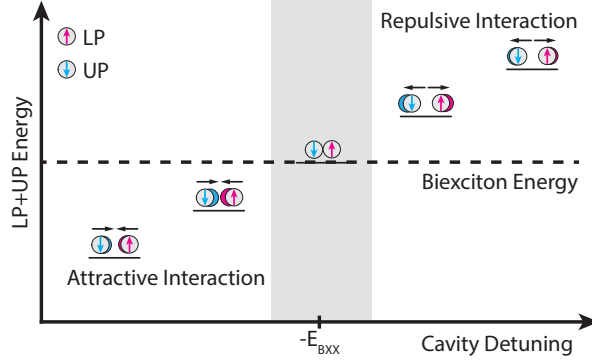


FIGURE 5.4: **The cross Feshbach resonance.** Two interacting lower polariton (LP) and upper polariton (UP) with antiparallel spin scatter to a biexciton state resonantly. Near the resonance, the interaction strength is enhanced, and its character changes from attractive to repulsive. The gray shaded area shows the cavity detuning range where scattering to the biexciton is significant. E_{BXX} is the biexciton binding energy.

5.4.1 Experimental Results

The experiment's central intention is to measure the energy renormalization induced by the polariton interaction by the transmitted probe's energy shift. The strength of the interaction between upper and lower polariton is determined from the renormalized energy shift of the upper polariton resonance due to the lower polaritons' presence. A blueshift appears if the interaction is repulsive; otherwise, it shows a redshift, which manifests an attractive interaction. The pump spot size is larger than the probe to ensure the probing of a constant carrier density. The probe intensity is one-tenth of the pump $n^{pu} = 2.8 \times 10^{11} \text{ photon pulse}^{-1} \text{ cm}^{-2}$. The pump pulse energy is adjusted to the energy of the lower polariton resonance for each detuning. The probe spectrum and intensity are measured in transmission as a function of the detuning and the delay τ between the pump and probe pulses.

In fig. 5.6, we compare the transmitted probe spectrum of the upper polariton resonance for different cavity detunings, measured at zero pump-probe delay, with or without the pump. We can follow the variations in the upper polariton's energy shift in the presence of an anti-parallel spin lower polariton population. A change of detuning from negative to positive corresponds to an energy shift of the upper polariton. It is first a redshift, then switching to a blueshift and recovering to a zero value. The signal's amplitude decreases, and the linewidth of the signal increases with detuning until -0.9 meV.

In Fig. fig. 5.7 (a), we plot as a function of cavity detuning the energy shift and, in fig. 5.7 (b), the change of absorbance of the transmitted probe signal at zero time delay, $\ln(I_{\text{probe}}/I_{\text{pump-probe}})$ where I_{probe} and $I_{\text{pump-probe}}$ refer to the

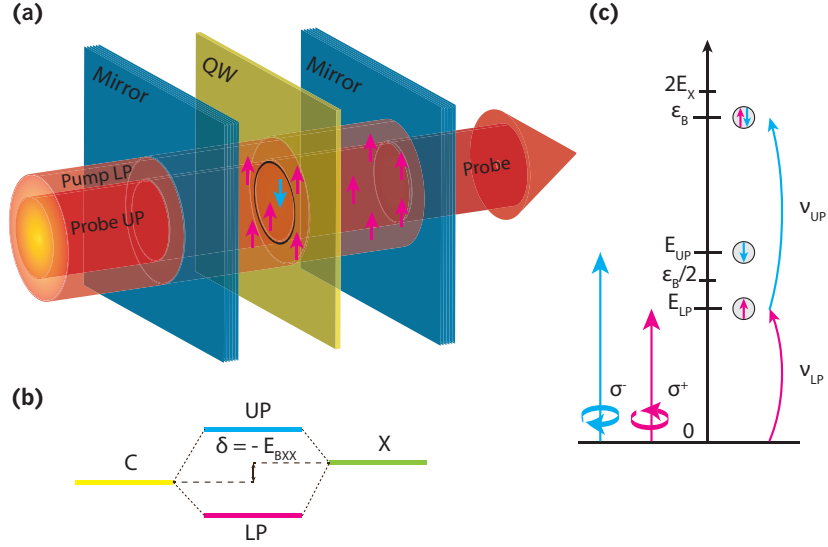


FIGURE 5.5: **A schematic representation of the experimental condition.** (a) Schematic view of the embedded quantum well in a semiconductor microcavity and pump-probe experiment configuration. (b) The cross Feshbach resonance occurs at the cavity detuning between the exciton state (X) and the cavity mode (C) given by $\delta = -E_{BXX}$. (c) Under this condition, an upper polariton with a spin down (\downarrow) and a lower polariton with a spin up (\uparrow) scatter resonantly to the biexciton state ($\downarrow\uparrow$). E_X , ϵ_B , E_{UP} and E_{LP} are respectively, exciton, biexciton, upper-polariton and lower-polariton energy. ν_{LP} (ν_{UP}) and σ^+ (σ^-) are, respectively, the energy and polarization of the pump (probe) pulse.

maximum intensity of probe signal either alone or in the presence of the pump pulse. The signature of the cross Feshbach resonance is clearly evidenced at -0.9 meV detuning through the change of sign of the energy shift, demonstrating the switching of the nature of the interactions between lower and upper antiparallel spin polaritons from attractive to repulsive. Correspondingly, the maximum reduction of the signal intensity at this detuning shows the resonant conversion of the upper and lower antiparallel spin polariton pair into a biexciton. This optimum cavity detuning also provides a direct measure of the biexciton binding energy E_{BXX} (see inserts in fig. 5.7 (a) and (b)) which has the value of $E_{BXX} = 0.9$ meV. Its value, $E_{BXX} = 0.9$ meV, lies in the expected range within the three-dimensional limit (0.15meV) and the two-dimensional limit (1.4 meV) given for an infinity deep confinement potential. The latter limit is estimated using a ratio of 0.22 between the biexciton and the exciton binding energies [58] and experimental value of the exciton binding energy of 6.5 meV [59]. There are different biexciton binding energies reported

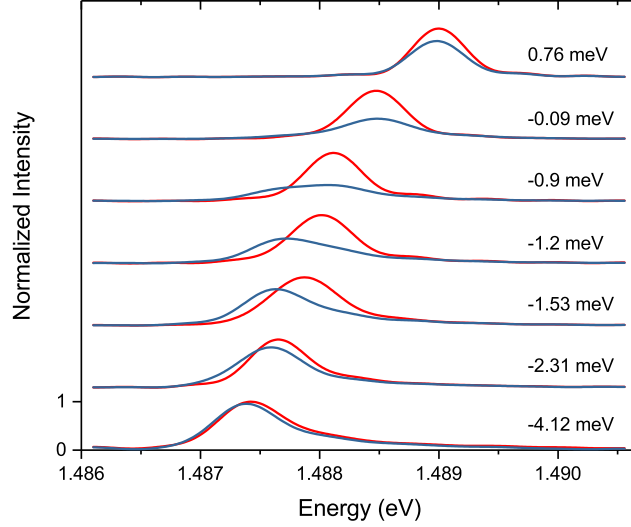


FIGURE 5.6: **Transmitted probe pulse at different detunings.** Transmitted probe spectra at upper polariton peak with (blue) and without (red) the presence of the anti-parallel spin lower polariton population for different cavity detunings at $\tau = 0$.

in the earlier studies of polaritonic Feshbach resonance, as large as 3 meV [31] and 2.3 meV [32]. This difference could be traced back to the pump excitation conditions [60]. In the former case, the pump pulse is a broadband pulse, which favors the generation of an excitonic reservoir. In the latter case, the pump pulse was spectrally narrowed, however as the experiments are performed in positive detunings, an excitonic reservoir can be formed. Moreover, at a positive cavity detuning, the lower polaritons are more exciton-like, increasing their interactions and significantly lower polariton energy renormalization. In our work, the experiment is performed with a spectrally narrow pump pulse at negative cavity detunings; under these conditions, we prevent an excitonic reservoir formation [60]. Additionally, the generated lower polaritons are more photon-like. In this configuration, an effect of energy renormalization either due to lower polariton-polariton interaction or due to their interactions with an excitonic reservoir is suppressed. We speculate that the latter mechanism was likely responsible for the larger value of the biexciton's binding energy [31, 32].

The increased depletion rate of the upper polariton population is quantified by the absorbance (fig. 5.7 (b)). The depletion rate caused by the upper-polariton-lower-polariton scattering to the biexciton at resonance corresponds

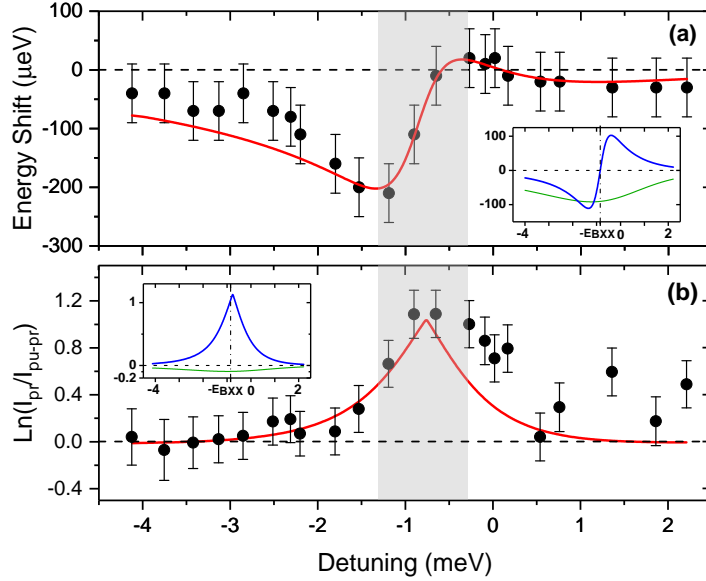


FIGURE 5.7: **Energy and intensity variation of UP.** Energy shift (a) and intensity variation (b) of the upper polariton peak in the presence of the anti-parallel spin lower polariton population as function of cavity detuning. The dots and the solid lines are the experimental and numerical simulation results, respectively. The gray shaded area shows the detuning range where scattering to the biexciton is effective. Inserts : The two contributions of background (green) and biexciton scattering (blue) to the upper polariton energy shift (a) and absorbance (b) as a function of detuning.

to the relative change of probe transmission at the energy of the upper polariton mode that is equal to $0.35 (= 1 - r.e^{-1.1})$, where 1.1 is the maximum of the measured absorbance change and $r = 2$ is the ratio of the upper polariton linewidths with and without the pump pulse. This means that about 35% of the transmitted photon flux of the probe pulse at the energy of the upper polariton gives rise to the creation of biexcitons at the cross Feshbach resonance.

The cross Feshbach resonance dynamic is studied by measuring the time-integrated transmission spectrum of the delayed probe pulse to the arrival of the pump pulse. In fig. 5.8, we present the probe spectrum centered on the upper polariton peak as a function of the pump-probe delay, for a detuning of $\delta = -1.2 \text{ meV}$, in the vicinity of the cross Feshbach resonance. These features are also highlighted in fig. 5.9, in which we show the transmitted probe spectra measured at zero delay with and without the pump beam. We observe

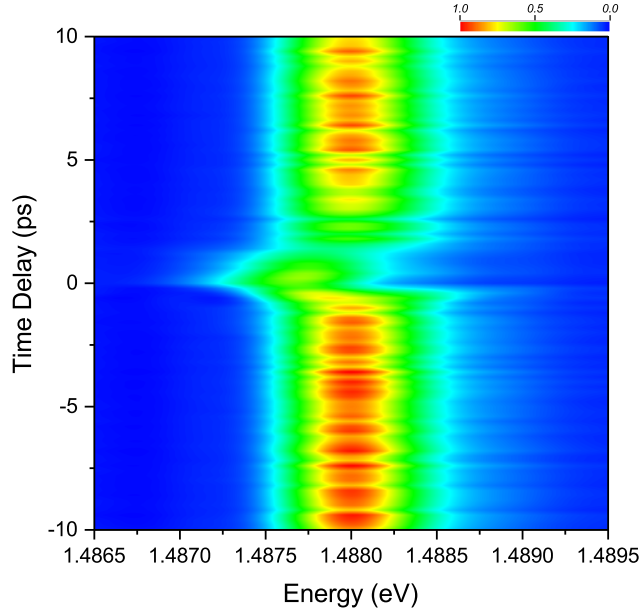


FIGURE 5.8: **Dynamic of the cross Feshbach resonance.** Transmitted probe spectra around the upper polariton energy (1.488 eV) as a function of pump-probe delay at $\delta = -1.2$ meV. The signal intensity fluctuations along the time delay correspond to shot noise.

an energy shift of the upper polariton peak and a reduction of its amplitude around a zero delay, which characterizes the cross Feshbach resonance. The dynamic is clearly revealed by the dependence of the energy shift with delay. The energy shift reaches its maximum value at zero delay. This corresponds to the largest scattering rate of an upper polariton with a lower polariton to the biexciton state occurring as expected when the optical pulses have the largest temporal overlap. The energy shift varies more rapidly at negative delays than it does at positive delays. The dynamic of the signal at negative delays is governed by the decoherence rate of the upper polariton polarization generated by the probe pulse. In contrast, the dynamic at positive delays is governed by the lifetime of the lower polariton population created by the pump. This lifetime is determined in part by the scattering rate between a lower and an upper polariton with opposite spins to the biexciton and, for the other part, by the escape rate of the photon from the microcavity.

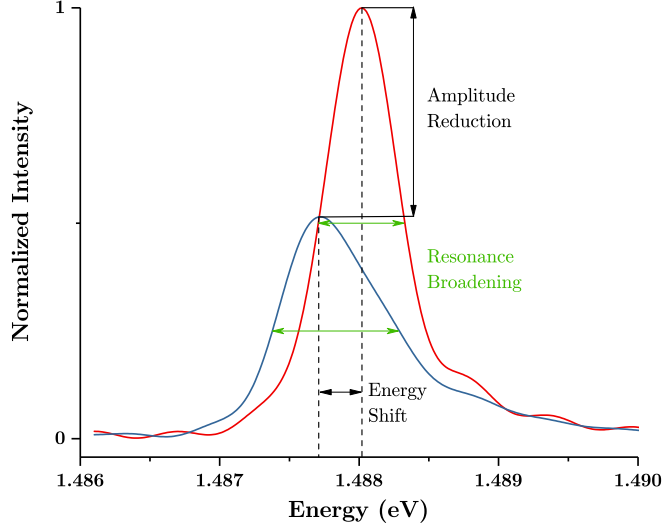


FIGURE 5.9: **Resonance variation with the pump pulse presence.** Transmitted probe spectra at zero delay with (blue line) and without the pump beam (red line) at the cavity detuning $\delta = -1.2 \text{ meV}$ in the vicinity of the cross Feshbach resonance.

5.4.2 Theoretical Model

The theoretical model we use to analyze our experimental results is rooted in the model developed for lower polariton interactions in a Feshbach resonance vicinity, described in detail in [32]. The model is based on the Bogoliubov theory; the scattering resonance of polaritons with a biexciton is studied within a mean-field two-channel model. We have introduced the exciton-photon basis Hamiltonian which involves the exciton-biexciton coupling eqs. (3.15) and (3.16). Assuming that the pump pulse excites the lower polariton branch with spin-up and the probe is resonant to the upper-polariton mode with spin-down by considering only the LP and UP cross interactions, we can rewrite the Hamiltonian in polariton basis as

$$\hat{\mathcal{H}}_0 \simeq \int dr \{ \mathcal{E}_{LP} \hat{a}_{L,\uparrow}^\dagger \hat{a}_{L,\uparrow} + \mathcal{E}_{UP} \hat{a}_{U,\downarrow}^\dagger \hat{a}_{U,\downarrow} + \mathcal{E}_b \hat{b}^\dagger \hat{b} \} \quad (5.1)$$

$$\hat{\mathcal{H}}_{int} \simeq \int dr \{ g_{+-} \chi^2 \mathcal{C}^2 \hat{a}_{U,\downarrow}^\dagger \hat{a}_{L,\uparrow}^\dagger \hat{a}_{L,\uparrow} \hat{a}_{U,\downarrow} + g_{bx} \chi |\mathcal{C}| (\hat{b} \hat{a}_{U,\downarrow}^\dagger \hat{a}_{L,\uparrow}^\dagger + \hat{a}_{U,\downarrow} \hat{a}_{L,\uparrow} \hat{b}^\dagger) \} \quad (5.2)$$

$$\hat{\mathcal{H}}_{qm} \simeq \int d\mathbf{r} \{ -\Omega_{qm} |\mathcal{C}| (\hat{a}_{L,\uparrow}^\dagger \mathbf{F}_\uparrow + \mathbf{F}_\uparrow^* \hat{a}_{L,\uparrow}) + \Omega_{qm} \mathcal{X} (\hat{a}_{U,\downarrow}^\dagger \mathbf{F}_\downarrow + \mathbf{F}_\downarrow^* \hat{a}_{U,\downarrow}) \} \quad (5.3)$$

Finally, we obtain the Gross-Pitaevskii equation for the upper polariton and the biexciton as

$$\begin{aligned} i\hbar \dot{a}_{U,\downarrow}(\mathbf{x}, t) = & \left(\mathcal{E}_U - i\gamma_U + g^{+-} \mathcal{X}^2 |\mathcal{C}|^2 |a_{L,\uparrow}(\mathbf{x}, t)|^2 \right) a_{U,\downarrow}(\mathbf{x}, t) \\ & + g^{bx} X_0 |\mathcal{C}_0| b(\mathbf{x}, t) a_{L,\uparrow}^*(\mathbf{x}, t) + f_{ext,\downarrow}(\mathbf{x}, t) \end{aligned} \quad (5.4)$$

$$i\hbar \dot{b}(\mathbf{x}, t) = (\mathcal{E}_b - i\gamma_B) b(\mathbf{x}, t) + g^{bx} \mathcal{X} |\mathcal{C}| a_{U,\downarrow}(\mathbf{x}, t) a_{L,\uparrow}(\mathbf{x}, t) \quad (5.5)$$

$$f_{ext,\sigma}(\mathbf{x}, t) = \Omega_{qm} \mathcal{X} F_\sigma(\mathbf{x}, t) \quad (5.6)$$

We consider a continuous-wave (CW) pump excitation resonant with the lower polariton and a CW probe beam with energy ε probing the upper polariton ($\tilde{\varepsilon} = \varepsilon - \varepsilon_U$). We assume that the wave functions can be written as mixtures of finite modes within these assumptions, the wave functions are written as

$$\begin{aligned} a_{U,\downarrow} &= a_{U,\downarrow}^{pr} = u_\downarrow(\tilde{\varepsilon}) e^{-i(\tilde{\varepsilon} + \varepsilon_U)t/\hbar} e^{ikx} \\ a_{L,\uparrow} &= a_{L,\uparrow}^{pu} e^{-i\varepsilon_L t/\hbar} \\ b &= m(\tilde{\varepsilon}) e^{-i(\tilde{\varepsilon} + \varepsilon_L + \varepsilon_U)t/\hbar} e^{ikx} \\ f_{ext}^{pr} &= |F_\downarrow^{pr}| e^{-i(\tilde{\varepsilon} + \varepsilon_U)t/\hbar} e^{ikx} \end{aligned} \quad (5.7)$$

By substituting eq. (5.7) in eqs. (5.4) to (5.6) we have

$$\begin{pmatrix} \tilde{\varepsilon} - g^{+-} \mathcal{X}^2 \mathcal{C}^2 |\psi_{L,\uparrow}^{pu}|^2 + i\gamma_U & -g^{bx} \mathcal{X} |\mathcal{C}| \psi_{L,\uparrow}^{pu*} \\ -g^{bx} \mathcal{X} |\mathcal{C}| \psi_{L,\uparrow}^{pu} & \tilde{\varepsilon} - (\varepsilon_B - \varepsilon_L - \varepsilon_U) + i\gamma_B \end{pmatrix} \begin{pmatrix} u_\downarrow(\tilde{\varepsilon}) \\ m(\tilde{\varepsilon}) \end{pmatrix} = \begin{pmatrix} |F_\downarrow^{pr}| \\ 0 \end{pmatrix} \quad (5.8)$$

Eventually, the analytical solution for $u_\downarrow(\tilde{\varepsilon})$ at $k = 0$ holds

$$u_\downarrow(\tilde{\varepsilon}) = \left(\tilde{\varepsilon} - (g^{+-} \mathcal{X}^2 \mathcal{C}^2 |\psi_{L,\uparrow}^{pu}|^2) + i\gamma_U - \frac{(g^{bx})^2 \mathcal{X}^2 \mathcal{C}^2 |\psi_{L,\uparrow}^{pu}|^2}{\tilde{\varepsilon} - (\varepsilon_B - \varepsilon_L - \varepsilon_U) + i\gamma_B} \right)^{-1} \quad (5.9)$$

eq. (5.9) real and imaginary parts give the upper polariton branch's energy shift ($\Delta E_{U,\downarrow}$) and the absorption variation (α_B).

$$\Delta E_{U,\downarrow} = g^{+-} \mathcal{X}^2 \mathcal{C}^2 |\psi_{L,\uparrow}^{pu}|^2 + (g^{bx})^2 \mathcal{X}^2 \mathcal{C}^2 |\psi_{L,\uparrow}^{pu}|^2 \frac{\varepsilon_U + \varepsilon_L - \varepsilon_B}{(\varepsilon_L + \varepsilon_U - \varepsilon_B)^2 + \gamma_B^2} \quad (5.10)$$

$$\alpha_B = (g^{bx})^2 \mathcal{X}^2 \mathcal{C}^2 |\psi_{L,\uparrow}^{pu}|^2 \frac{\gamma_B}{(\varepsilon_L + \varepsilon_U - \varepsilon_B)^2 + \gamma_B^2} \quad (5.11)$$

γ_B is the biexciton linewidth, and the $|\psi_{L,\uparrow}^{pu}|^2 = \mathcal{C}^2 n^{pu}$ is the lower polariton density generated by the pump.

In eq. (5.10), the first and second terms contribute to the upper polariton's energy shift by LP-UP antiparallel spin background interaction and scattering to the biexciton state, successively. There are also two contributions to the change of absorbance of the upper polariton mode. The first one originates from the LP-UP scattering to the biexciton, given by eq. (5.11). The second contribution results from the negative background term that corresponds to an attractive interaction between upper and lower polariton modes of opposite spins. This interaction results in an effective energy redshift of the exciton, $\Delta E_X = g^{+-} \mathcal{X}^2 n^{pu}$, and then in an effective increase of the cavity detuning $\delta' = \delta - \Delta E_X$, which implies a larger photonic fraction of the upper polariton mode [61]. The dependence of this absorbance variation with detuning is thus given by $\alpha_B = 2 \ln[\mathcal{X}(\delta)/\mathcal{X}(\delta')]$. Where \mathcal{X} is the Hopfield coefficient and given by eq. (2.13).

In fig. 5.7 (a) and fig. 5.7 (b), we plot the detuning dependence given by the above expressions for the energy shift and the absorbance, respectively, with the experimental results. The best fit with the theoretical model was obtained with $E_{BXX} = 0.9 \text{ meV}$, $g_{bx} = 0.86 \text{ meV} / \sqrt{n^{pu}}$, $\gamma_B = 0.5 \text{ meV}$ and $g^{+-} = -0.62 \text{ meV} / n^{pu}$. The fits reproduce the resonance features with a perfect agreement with the experimental results. In the inserts of fig. 5.7, we compare the contributions of the background and the biexciton scattering to the energy shift (insert (a)) and the absorption (insert (b)) of the upper polariton mode. The green and blue lines correspond to the energy shift and absorbance using the parameters mentioned earlier, but by setting, $g_{bx} = 0$ and $g^{+-} = 0$, respectively. The biexciton scattering contribution (in blue color) to the energy shift and the absorbance clearly shows the dispersion shape with a centered resonance on the biexciton energy. The negative background contribution (in green color) only accounts for the Hopfield coefficient's dependence with detuning. From this comparison, we infer that the cross Feshbach resonance's principal effect is arising at a cavity detuning equal to the biexciton binding energy. The weak contribution of the background effect to the absorbance and the resonance position centered at a cavity detuning equals the biexciton binding energy is a strong signature of the cross Feshbach

resonance. From the fits' quality, we conclude that the observed resonance is indeed caused by the scattering of a pair of upper and lower polaritons into the biexciton state. The fits provide an excellent and quantitative description of the primary resonance features across the detunings range, apart from a small absorption deviation at the positive detunings. The measured absorption change is more significant than prediction based on a single scattering channel (the biexciton state), indicating the existence of additional scattering channels above the biexciton energy that corresponds to the energy continuum of two-exciton states [62], which sets at zero detuning.

The coupling between polaritons and biexcitons depends on the lower polariton population. This coupling does not overcome the biexcitons' damping rate in the low-density regime of the lower polariton. In this weak interaction (perturbative) regime, the cross Feshbach resonance (fig. 5.7) appears with a dispersive shape and a width due to the biexciton lifetime. However, in the high lower-polariton density regime, when the coupling overcomes the biexcitons' damping rate, the system will enter the strong interaction regime, and polaritons biexcitons states manifest an anticrossing [31, 63]. In our experiments, the transition from weak to strong interaction regime could be reached by increasing the pump power, which was not achievable under our experimental conditions using an optical pulse shaper.

In a recent theoretical paper [63], the authors present a many-body theory for interacting polaritons with a Bose-Einstein condensate of polaritons in another spin state. They evidence the cross Feshbach resonance in the upper polariton branch when the biexciton energy equals two free lower plus upper polaritons. They model our experiments, and the numerical results fit the upper polariton energy shift as a function of the cavity detuning accurately. The position and width of the resonance are reproduced with only two free parameters: the biexciton binding energy -0.7 meV and the biexciton decay of 0.4 meV, which all agree with our results.

In conclusion, we have done pump-probe spectroscopy with a counter-circular polarization arrangement to study the polariton interactions. A narrow-band pump pulse is exciting lower polariton mode, and a transmitted broadband probe pulse conveys the signatures of the optical resonance, strength, and sign of the energy shift induced by the pump. We attribute the scattering process's origin between polariton modes with opposite circular polarization to a biexciton bound state. Additionally, we have investigated the biexciton's critical role in interbranch polariton interaction with the opposite spins. We found the energy shift and enhancement of the probe spectra's absorption. This behavior can be incorporated with a scattering resonance of the lower and upper polaritons to the biexciton state or polaritonic cross Feshbach resonance. For the interpretation, a spin-dependent Hamiltonian, including the coupling between excitons and biexciton, has been implemented.

5.5 PERSPECTIVES

The demonstration of polaritonic cross Feshbach resonance will permit the control of the polariton interbranch scattering. It may initiate studies of many-body physics with polaron quasiparticles and lead to entangled photon pairs' generation via the biexciton.

5.5.1 *Many-body Physics with Polaron Quasiparticles*

The behavior of an impurity interacting with a quantum bath gives insight into quantum many-body systems' physics. For instance, the coupling between electrons and lattice phonons leads to the existence of quasiparticles termed polarons [64]. Recently, the Feshbach resonance has been implemented to tune the interaction strength between a mobile impurity and a Bose gas of cold atoms in order to realize a Bose polaron in a strongly interacting regime [65, 66]. This is illustrated in fig. 5.10. The strength of the attractive and repulsive interaction of the impurity atoms (orange dots) with the condensate (blue background) is represented, respectively, by the decrease and increase condensate density (intensity of blue) around the impurity. The Feshbach resonance with the bound impurity-BEC's atom molecule is the position in which the abrupt change from attractive to repulsive interaction occurs.

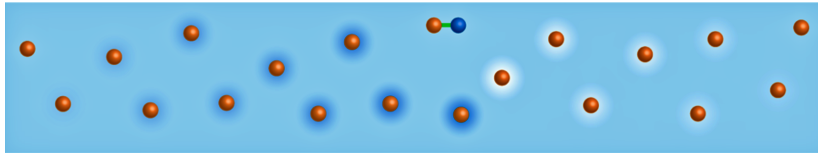


FIGURE 5.10: **An impurity interacting with a quantum bath.** The cartoon shows impurity atoms (orange) in a Bose-Einstein condensate (BEC) (blue); the intensity of the background color indicates the change in the BEC density due to the presence of impurity atoms. The bound impurity-BEC's atom molecule shows the position of the Feshbach resonance. Reproduced from [65].

The cross polariton interaction system may share similar polaron properties of an atomic impurity interacting with a Bose gas, where the upper polariton mode replaces the impurity atom, and the coherent population of lower polariton is substituted for the Bose gas. In a recent theoretical paper [50], the authors model, beyond the mean-field theory, the quantum impurity picture with two- and three-point quantum many-body correlations. From the experimental point of view, they model a pump-probe experiment: the pump generates a Bose gas of a spin-up lower-polariton population, and the probe brings either a lower or upper spin-down polariton impurity. They explore the Feshbach and (cross) Feshbach resonances with the biexciton and triexciton

molecular states to show the multipoint correlations' emergence as splitting in the impurity spectrum. With the experimental demonstration of cross Feshbach resonance, we can go forward into quantum correlated polariton physics. We envisage polariton systems with longer-lived Feshbach molecules to favor the correlations and the experimental observation of the splitting in the impurity spectrum. Also, extending the control of cross polariton interaction in a system constitutes polaritons in an electron gas [51].

5.5.2 Generation of Entangled Photon Pairs

Different schemes for generating entangled photon pairs in semiconductors have been the subject of several theoretical studies [48, 49, 67, 68]. The most effective one relies on the generation of biexcitons by interbranch polariton scattering. Despite the great interest attracted by non-classical light sources for quantum information processing [69] and quantum cryptography [70] an implementation via the biexciton in an optical microcavity is still pending.

The demonstration of the cross Feshbach resonance opens the way to implement the generation of entangled photon pairs. The principle for their creation is the following. A biexciton is generated by the scattering of one lower and one upper polariton with opposite spins. It decays into two lower polaritons with opposite momenta and spins, which emit an entangled photon pair in polarization and momentum. This process is optimal at exciton-cavity detuning comparable to the biexciton binding energy in which the energy of the lower plus upper polaritons equalizes the biexciton energy. This is the condition for the cross Feshbach resonance. Based on the theoretical prediction for generating a pair of entangled photons [49], the proposed scheme is represented in fig. 5.11. Figure 5.11 illustrates the advantage of using interbranch polariton scattering in the cross Feshbach resonance. The entangled photon pairs leave the microcavity with a large momenta far away from the incoming beams, which form the lower and upper polaritons at $k = 0$. This situation will permit the entangled photon pairs to be isolated from the transmitted laser beams on the microcavity.

The efficiency of this generation process of a pair of entangled photons with opposite momenta and spins is determined in part by the rate of the scattering process that generates a biexciton and, in the other part, by the dissociation rate of the biexciton into two outgoing polaritons with opposite spins. From the observation of the cross Feshbach resonance, we infer that the generation of entangled photon pairs in semiconductor microcavities could be very efficient. The depletion rate of the upper polariton-lower polariton scattering to the biexciton corresponds to the relative change of probe transmission at the upper polariton mode's energy. We found that about 35% of the transmitted probe photons were converted into biexcitons at the cross Feshbach resonance. Different dissociation channels of the biexciton state were identified and described in [71]. They have made a quantitative evaluation of the rate for

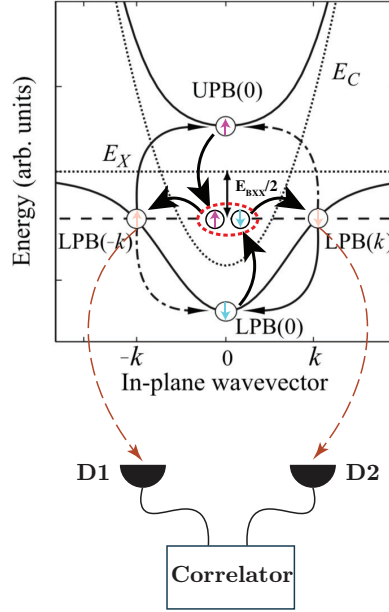


FIGURE 5.11: **Scheme for generation and detection of entangled photon pairs.** At the cross Feshbach resonance, in which the upper-lower polaritons scattering is optimal, a pair of entangled photons is generated. The arrows represent the cross-interaction processes. This figure is adapted from [49]. Two avalanche photo detectors (APD) of D1 and D2 and correlation measurement are represented.

each of the relevant channels and concluded that the dissociation into two lower polaritons with opposite momenta was about equally probable to the dissociation into two interface polariton modes; the dissociation efficiency into a pair of one lower and one upper polariton being nearly two orders of magnitude weaker. Assuming then that the dissociation of the biexcitons is about equally distributed between pairs of lower polaritons and pairs of interface polaritons [71], we estimate that one-half of the excited biexcitons lead to outgoing pairs of entangled lower polaritons. The estimated flux of entangled photon pairs is then about 1.7×10^8 pairs per cm^2 per incident pulse. The flux of outgoing entangled photon pairs is further reduced by the square of the radiative efficiency of the lower polariton mode having a large momentum ($2.6 \mu\text{m}^{-1}$), which amounts to 7% when accounting for the non-radiative scattering of polaritons by acoustic phonons [72]. Our estimation of the generation rate (1.2×10^7 pairs per cm^2 per incident pulse) makes the proposed scheme based on the cross-Feshbach resonance quite attractive for the generation of entangled photon pairs in momentum and polarization.

By resonantly exciting the lower polariton modes at large momenta, in a reversed generation scheme, outgoing upper and lower polaritons' production

becomes entangled in energy and polarization. This scheme's main drawback lies in a strongly reduced dissociation rate of the biexciton into pairs of upper and lower polaritons, which is predicted to be smaller by two orders of magnitude compared to the dissociation rate into lower polariton pairs [71]. This reduction is partially compensated by a higher radiative efficiency of a pair of lower and upper polaritons at $k = 0$ (about 50%). To realize a bright source of entangled photons, high radiative efficiency will also enhance the photon pairs correlation's visibility. It ultimately might favor the generation system based on a pair of entangled photons in energy and polarization.

In this chapter, we present coupled polaritons in a lattice landscape. By engineering a periodic lattice of mesas on a two-dimensional microcavity, it is possible to couple confined polariton modes of nearby mesas to establish an optical lattice similar to the crystalline semiconductors' electronic band structures. Such lattices can be patterned by employing conventional lithography and etching techniques, which empower us to fabricate arbitrary potentials with robust localization and adaptable nearest-neighbor coupling. On-chip polaritons appeared as an excellent method to realize and study strong bosonic nonlinearities (due to their excitonic part) beyond ultralow temperatures.

This chapter contains two separate studies on photonic localization in a triangular lattice made of mesas. The first part is devoted to the localization due to the breaking of translational symmetry in a regular lattice. In the second part, we present localization by introducing controlled lattice disorder. We start the chapter by describing the sample following by the experimental setup used in both investigations. Next, the experimental sample characterization with a theoretical model is presented. Then, we demonstrated the localization of a photon lasing in the regular polaritonic lattice. Finally, disorder-inducing localization is reported. We give the outlook with a conclusion eventually. The content henceforth is adapted from the following papers [73, 74]. Some paragraphs are reported (quasi-)verbatim.

- *Localized Photon Lasing in a Polaritonic Lattice Landscape*
M. Navadeh-Toupchi, F. Jabeen, D.Y. Oberli, and M.T. Portella-Oberli
Phys. Rev. Applied **14**, 024055 (2020)
- *Anderson localisation in steady states of microcavity polaritons*
T.J. Sturges, M.D. Anderson, A. Buraczewski, M. Navadeh-Toupchi, A.F. Adiyatullin, F. Jabeen, D.Y. Oberli, M.T. Portella-Oberli, and M. Stobińska
Scientific reports **9**, 1–6 (2019)

6.1 SAMPLE AND EXPERIMENTAL SETUP

6.1.1 Sample

Polariton confinement in reduced dimensionality structures causes new characteristics. Several techniques were developed to trap polaritons either by acting on the excitonic [75, 76] or photonic [38, 77] component. One possible way to engineer the potential where

polaritons are created and confine them spatially is to change the thickness of the cavity layer locally in so-called mesa structures [38]. The trap consists of a mesa in the spacer layer, etched on the top of a microcavity spacer. This mesa confines the cavity photon for sizes of a few microns in width, and typically six nanometers in-depth. The quantization of the lower and upper polariton modes in several states is caused by the lateral confinement [39].

The layout of the sample used to investigate is explained in fig. 6.1. The sample is grown by molecular-beam epitaxy on a GaAs substrate. It is a microcavity made with a GaAs λ -spacer layer, and two distributed Bragg reflector (DBR) mirrors consisting of 20 (24) pairs of GaAs/AlAs layers for the top (bottom) mirror. The spacer layer is patterned before the growth of the second DBR of the cavity [39]. The triangular array is done through an electron-beam lithography and etching process. The photon traps consist of shallow mesas with a local elevation of 6 nm and a diameter of 2 μm at the spacer layer's surface. This potential leads to a local reduction of the microcavity resonance frequency and a photonic confinement potential of 9 meV. The mesas are equally separated by a distance of 2.5 μm from the center to center. The confined photon wave function penetrates the barrier, causing evanescent photonic coupling between neighboring mesas, which induces a photonic energy band structure. A single $\text{In}_{0.04}\text{Ga}_{0.96}\text{As}$ quantum well is placed at the electromagnetic field's antinode in the middle of the spacer layer. The strong coupling between the exciton and photonic modes gives rise to a band structure made of the upper and lower polariton bands corresponding to a Rabi splitting of $\Omega_R = 3.4 \text{ meV}$. The exciton energy is $E_X = 1.4814 \text{ eV}$. The measured exciton-cavity detuning has a value of 1.5 meV; it is defined as the energy difference between the lowest photonic band and the exciton at the Brillouin zone center.

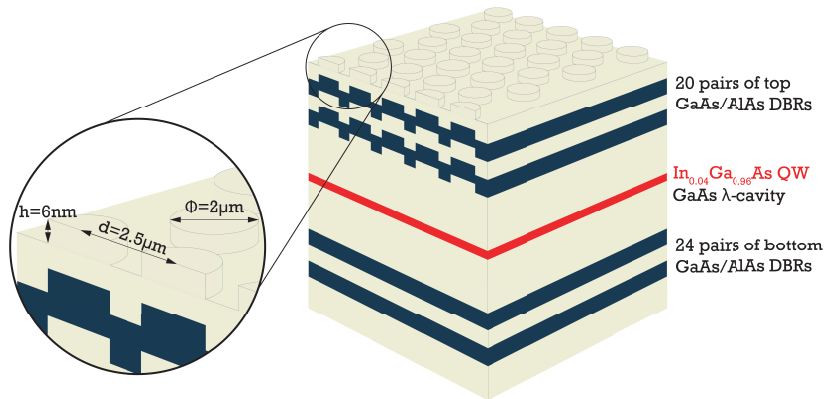


FIGURE 6.1: **Schematic of the patterned sample.** Schematic drawing of the sample representing the patterned and epitaxial layer structure; DBR stands for distributed Bragg reflector. The inset shows the mesa configuration.

6.1.2 Experimental Setup

We excite the sample nonresonantly with a CW laser at 660 nm with a spot size of either 25 μm or 3 μm measured as the full width at half maximum. The experimental setup is shown in fig. 6.2. The laser beam is focused on the top side of the sample utilizing a microscope objective ($\times 50$) with a numerical aperture of 0.42. To increase the spot size, the laser is sent to an additional lens placed at a distance for which its focal plane coincides with the back Fourier plane of the microscope objective to reduce the laser spot size in the Fourier plane. The laser beam is modulated at a 0.6 kHz frequency with a chopper operating with a duty cycle of 6% to avoid the sample's thermal heating.

The sample's emission is collected in the reflection configuration with the same objective used for the excitation; it is then focused with a 400 mm focal length lens on a CCD camera for imaging in real space; the integrated emission in energy results in a magnification of 100.

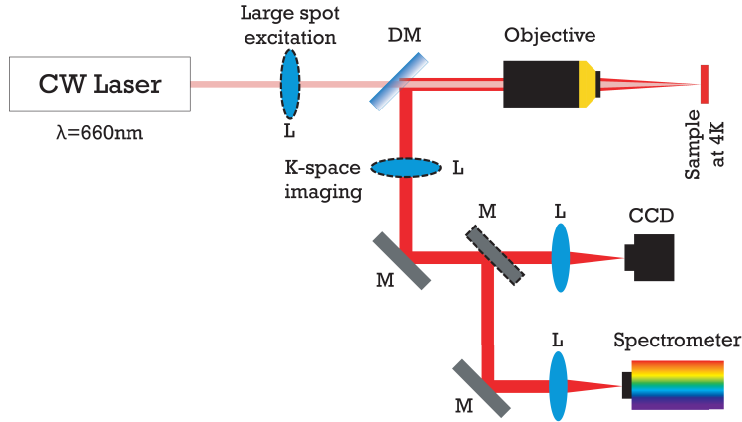


FIGURE 6.2: **Schematic of the experimental setup.** Layout of the experimental setup: DM, dichroic mirror; M, mirror; L, lens. Movable parts (lenses and mirror) are drawn with dashed lines.

The spectrally resolved emission is obtained either in the near field or in the far-field by imaging the sample surface plane or the Fourier plane of the microscope objective on the spectrometer's entrance slit coupled to a CCD camera. We measure the spatial and the momentum distribution of the emission as a function of energy recorded along the x-direction and the $\Gamma - K$ direction in the Brillouin zone, respectively. The reciprocal space imaging is used for accessing the polariton and photonic dispersion curves. The experiments are performed with different excitation pump powers.

The sample is placed in a cryostat with a continuous-flow of liquid helium operating at 4 K. The cryostat is mounted on a three-dimensional translation stage for tuning its position, with a base structure conceived to reduce the

vibrations and the thermal drifts. The helium dewar is kept suspended by the optical table, which significantly reduces the sample's vibrations from the ground. To monitor the stability of the measurements, we image the sample surface with the excitation laser spot on a CCD camera as described above. We control then the stability of the laser-spot position concerning the mesa pattern during the experiment. The sample remains stable without drifting from its initial position during minutes, which is long enough for the typical data acquisition time.

6.2 THEORETICAL MODEL

Since light and matter coupling form polaritons, both the photonic and the excitonic part can be confined. The excitons are localized in the plane of the quantum well. The excitonic effects such as exciton binding and oscillator strength are enhanced in the reduced dimensions, as described in chapter 2.

Micropillars were proposed in the first design to confine the photonic part by etching the microcavity after growth [37]. Weak coupling regime and polariton lasing have been published in the before-mentioned structures [14, 78]. In this dissertation, we confine the photonic part of the polaritons laterally by creating a slightly thicker cavity on the spacer layer, which we call mesa. The thicker cavity decreases the cavity photon energy and behaves as a trap for cavity photons and, consequently, polaritons. Thanks to the low aspect ratio in mesas, the lateral roughness and losses are less than the micropillars and allowing us to reach sub-micron mesas (the subject of chapter 7 in this dissertation).

We use a simple tight-binding approach to describe the microcavity polariton modes in a triangular lattice made of isolated mesas. As the lattice period is larger than the mesa diameter, the coupling between next-nearest-neighbor mesas is weak. We consider only the photonic modes with the lowest energies in a single mesa: the lowest energy state (referred as the S-orbital mode) has an angular momentum equal to zero; the next excited state is doubly degenerate (referred as the two P-orbital modes), and is associated to an angular momentum equal to one. The expressions for the energy dispersion of the S and P photonic bands of the triangular lattice are, respectively, given by [79, 80]

$$E^S = E_0^S - \gamma_0 - \gamma_S \left\{ 4 \cos \frac{a}{2} k_x \cos \frac{a}{2} \sqrt{3} k_y + 2 \cos a k_x \right\} \quad (6.1)$$

$$E_{1,2}^P = \frac{(E_1 + E_2)}{2} \mp \sqrt{(E_1 - E_2)^2 + 4E_3^2} \quad (6.2)$$

where

$$E_1 = E_0^P - \gamma_1 + 2\gamma_{\parallel} \cos a k_x + \left(\gamma_{\parallel} - 3\gamma_{\perp} \right) \cos \frac{a}{2} \sqrt{3} k_y \cos \frac{a}{2} k_x \quad (6.3)$$

$$E_2 = E_0^P - \gamma_2 - 2\gamma_\perp \cos ak_x + \left(3\gamma_\parallel - \gamma_\perp\right) \cos \frac{a}{2} \sqrt{3} k_y \cos \frac{a}{2} k_x \quad (6.4)$$

$$E_3 = -\gamma_3 \sin \frac{a}{2} \sqrt{3} k_y \sin \frac{a}{2} k_x \quad (6.5)$$

E_0^S and E_0^P are the energies of the S and P photon modes of an isolated mesa; γ_\parallel and γ_\perp are the tunneling energies between nearest mesas associated with the P orbitals oriented either parallel or perpendicular to the link direction; γ_S is the tunneling energy associated with the coupling of S orbitals between nearest mesas fig. 6.3; γ_3 is the tunneling energy associated with the coupling between P_x and P_y orbitals centered on nearest mesas; γ_0 , γ_1 and γ_2 are corrective energies for the photonic modes in isolated mesas.

The dispersion relations of the photonic P bands are simply given by the expressions for E_1 and E_2 along specific directions of the Brillouin zone, e.g., $\Gamma - K$ for which k_y is equal to zero or $\Gamma - M$ for which k_x is equal to zero. The corresponding polaritonic S and P bands are obtained in the strong-coupling limit between excitons and photons assuming the same Rabi-coupling energy for the two photonic modes (S and P modes). The corresponding polariton modes can be calculated as

$$E^{S,UP,LP}(k) = \frac{1}{2} \left[E_x + E^S(k) \pm \sqrt{\Omega_R^2 + (E^S(k) - E_x)^2} \right] \quad (6.6)$$

$$E_{1,2}^{P,UP,LP}(k) = \frac{1}{2} \left[E_x + E_{1,2}^P(k) \pm \sqrt{\Omega_R^2 + (E_{1,2}^P(k) - E_x)^2} \right] \quad (6.7)$$

6.3 SAMPLE CHARACTERIZATION

To characterize the sample emission in the strong- and weak-coupling regimes, we perform the experiments by focusing the laser beam to a spot size of 25 μm . We measure the planar part of the microcavity's photoluminescence at a low excitation laser power of 10 mW in the far-field configuration. Figure 6.4 (a) displays the planar microcavity's dispersion surrounding the sample's patterned region at a photon-exciton detuning of 8.4 meV. We observe the 2D lower polariton flat dispersion (mostly an excitonic mode) and the upper polariton parabolic dispersion, which is mostly a photonic mode, over a range in k -space going from $-3 \mu\text{m}^{-1}$ to $3 \mu\text{m}^{-1}$, which is defined by the numerical aperture of the microscope objective. We repeat the measurement at different positions of the sample in order to vary the detuning between the cavity photon and exciton energy; in fig. 6.4 (b), we plot the energy of the lower

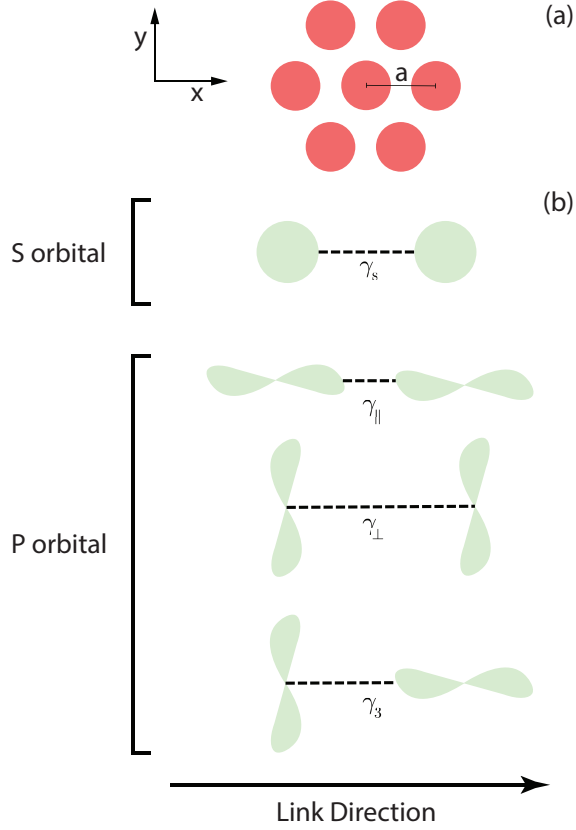


FIGURE 6.3: **Tunneling between the nearest mesas.** The sketch of nearest mesas separated by the distance a in (a) and in (b) of the tunneling energies between nearest mesas associated with the coupling of S orbitals (γ_s), with the P orbitals oriented either parallel ($\gamma_{||}$) or perpendicular (γ_{\perp}) to the link direction; γ_3 is the tunneling energy associated with the coupling between P_x and P_y orbitals centered on the nearest mesas.

polariton (LP) and upper polariton (UP) at $k = 0$ varying the sample position. From these experiments, we obtain exciton energy of $E_x = 1.4814 \text{ eV}$ and a Rabi energy of $\Omega_R = 3.4 \text{ meV}$ by eq. (2.11).

We measure the photoluminescence of the patterned part of the sample with different excitation laser power. The photoluminescence at low excitation power gives directly in k space the image of the energy dispersion of the polariton modes with the system in the strong coupling, which reveals the LP and UP energy bands fig. 6.5 (a). The relaxation of polaritons results in the population being distributed in the LP and UP energy S band with the highest intensity emission from the LP band. The weak emission of UP at higher energy originating from the P bands can be perceived. This feature is

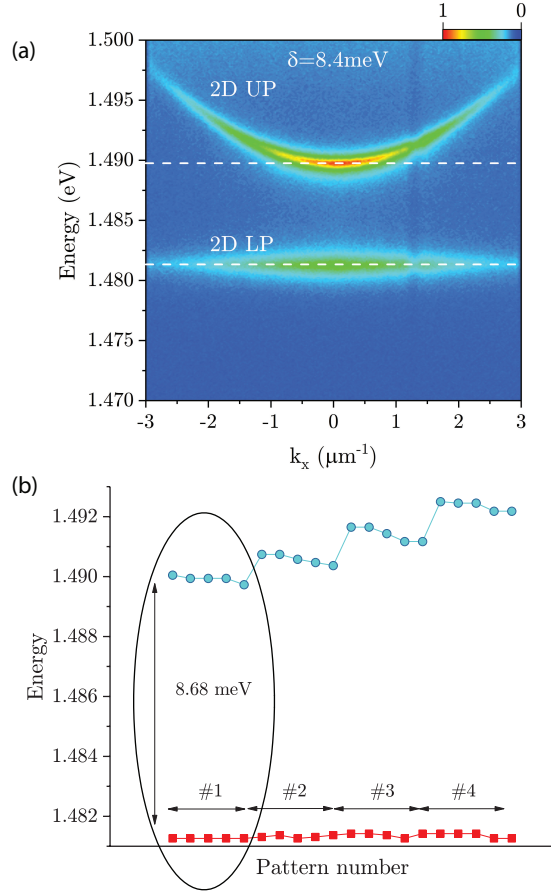


FIGURE 6.4: **Characterization of the planar microcavity.** (a) Dispersion of the planar microcavity at cavity detuning of 8.4 meV with the excitonic-like lower polariton (2D LP) and photonic-like upper-polariton (2D UP) dispersion. (b) LP and UP energy at $k = 0$ measured at different cavity positions or different cavity detuning.

better observed for UP bands because of the positive detuning of the sample. Under high excitation power when the strong coupling breaks down, we assess the energy dispersion of the photonic bands fig. 6.5 (b). We observe the emission from the S and P photonic bands, which are formed, respectively, by evanescent coupling of s and p photon states confined in the mesas. At a higher energy, the emission from the two-dimensional photonic continuum is perceived as a faint emission around 1.492 eV. The calculated polaritonic and photonic S and P bands are plotted, respectively, in fig. 6.5 (a) and fig. 6.5 (b). We use the following values of the parameters for the fittings: $\gamma_S = 0.12$ meV, $E_0^S - \gamma_0 = 1.48370$ eV, $E_0^P - \gamma_1 = 1.48781$ eV, $E_0^P - \gamma_2 = 1.48803$ eV, $\gamma_{\parallel} =$

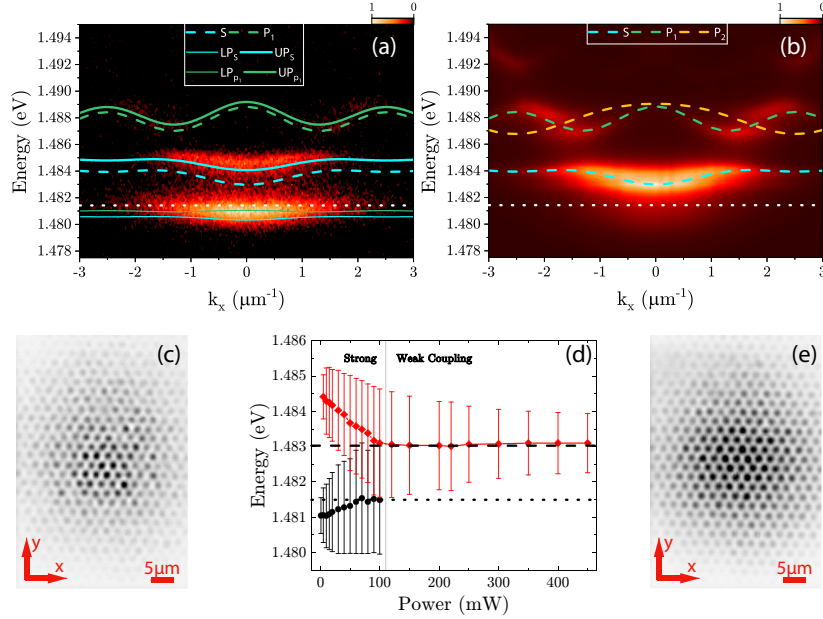


FIGURE 6.5: **Triangular photonic lattice under nonresonant laser excitation with a $25\ \mu\text{m}$ spot size.** The emission spectra recorded along the $\Gamma - K$ direction of the Brillouin zone at excitation power of 5 mW (a) and 450 mW (b), respectively, in the strong- and weak-coupling regime. The calculated LP and UP S and P dispersion bands (photonic bands) are plotted with solid lines (dashed lines). The intensity profile of the energy-integrated emission measured in the strong- (c) and the weak- (e) coupling regime. (d) Energy and linewidth of the S -band emission at $k = 0$ as a function of pump power for the lower (black) and upper (red) polariton in the regime of strong coupling and for the photon in the weak-coupling regime. The linewidth of the modes is represented as an error bar. The dotted (dashed) line indicates the exciton (S photon mode at $k = 0$) energy.

$0.40\ \text{meV}$ and $\gamma_{\perp} = 0.067\ \text{meV}$. However, the second P band is not observed for still unclear reasons. It is worth mentioning that the tunneling energy parallel to the link direction is much larger than the one perpendicular to the link as expected from the more considerable overlap of the P orbitals aligned along the link joining nearest mesas with respect to the P orbitals oriented orthogonal to the link.

We obtain the intensity profiles of the polaritonic and photonic lattice landscape by imaging in real space, the energy integrated emission of the sample in the strong- fig. 6.5 (c) and weak-coupling fig. 6.5 (e) regimes, respectively. The regular triangular patterned structure can be observed both in the polaritonic and in the photonic lattice landscape. In fig. 6.5 (d), we plot the

energy of the LP and UP S-band emission at $k = 0$ as a function of pump power. With increasing pump power, we evidence a blueshift of the LP, a redshift of the UP, and a broadening of their linewidth (represented by error bars). We eventually observe the shrinkage of the Rabi coupling and the photonic mode dispersion's emission, with its linewidth narrowing accordingly. These findings evidence the features characterizing the breakdown of the exciton-photon strong coupling. In nonresonant excitation, electrons and holes are generated at high energy and relax down to form excitons and polaritons. The exciton-exciton interactions induce decoherence, and accordingly, linewidth broadening of polaritons [30]. The exciton oscillator strength weakens when the carrier density is increased due to Coulomb screening and phase-space filling [81]. These effects reduce the coherent coupling between exciton and photon until its breakdown. We notice that the strong coupling persists in the excitation area's periphery, where the carrier density is much weaker. Therefore, the photon dispersion's measured linewidth appears broader than in the case of the bare photonic emission.

6.4 LOCALIZED PHOTON LASING

A photonic crystal [82] is a periodically modulated structure with photonic dispersion similar to the electronic band structure in a crystal presenting multiple bands separated by band gaps. In a crystal, the band curvature defines positive and negative effective masses. The photonic dispersion shapes, in the same way, determine the normal and anomalous dispersion. The photon dynamics can be controlled by the interplay between the dispersion, diffraction, and the nonlinearity in these photonic systems [83]. In the lattice of evanescently coupled waveguides, localized spatial solitons [84–87] are generated when on-site nonlinearity balances the diffraction arising from linear coupling among adjacent waveguides [84, 88]. Therefore, photonic bandgap systems' dispersion, which relates the photon energy, and wave-vector of propagating light, can be controlled. The realization of band-edge lasers [89–93] is possible thanks to small group velocity near the Brillouin zone's edge. The localization of light can also be induced by locally perturbing the modulated structure's periodicity, which generates a defect state [82]. A two-dimensional photonic crystal defect provides a resonant microcavity for achieving lasing [94–96].

The semiconductor microcavity forms the basis for flexible photonic platforms where the engineered potential landscapes give rise to substantial transport properties and appealing physics and applications [97]. The two-dimensional polaritonic lattices [98] are periodically modulated microcavities in transverse directions with translational invariance regarding the longitudinal direction. The lower and upper polaritons' dispersion corresponds to a band structure separated by the Rabi coupling energy. Their dispersion is composed of S and P bands, which originate from the spatial overlap of s and p levels from polaritons confined in all three spatial directions on adjacent mesas.

Polariton propagates in the transverse direction according to the energy-band dispersion. The band structure has a strong influence on the polariton condensation process. At the edge of the Brillouin zone with effective negative mass, the repulsive polariton interaction with a spatially localized excitonic reservoir produces an energy blueshift of the condensate into the gap, and it generates a localized gap soliton state [99–101]. The localized condensate state can also depend on the spatial position of the excitation [102]. In the regime of weak coupling between excitons and photons, photonic resonator crystals using two-dimensional coupled arrays of vertical-cavity surface-emitting lasers (VCSELs) have led to a coherent supermode emission located at the edge of the Brillouin zone [103–105]. The achievement of single-mode lasing was made possible by introducing a defect cavity in VCSEL photonic structures [106–109].

Our approach to localize light is to induce a breakdown of the exciton-photon strong coupling within a spatially limited region to destroy the photonic crystal symmetry. Inside this region, photonic modes' energy is different from those of the polariton modes outside of it. Thus, photon propagation to the outer area is inhibited, inducing a self-trapping of light. We use the scheme based on optically inducing a local breaking of the strong-coupling regime of polaritons to generate the photonic lattice defect by quenching any photon propagation outside this local region. The reduction of the losses by propagation can facilitate a phase transition to photon lasing, as observed in VCSELs. Due to the interplay between gain and propagation losses, the lasing from localized photon modes can be favored as a hybrid patterned system of photons and polaritons.

To establish the localization of photon lasing emission, we perform the experiments by focusing the laser onto a spot size of $3\ \mu\text{m}$ and by centering it on top of a mesa. We measure the emission spectra of the sample in momentum and real space for different excitation powers. Figure 6.6 displays the energy-resolved emission in momentum and real space for four excitation powers of 3 mW, 70 mW, 90 mW, and 130 mW. In Figure 6.7 (a), we plot integrated emission intensity as a function of laser power, ranging from 1.478 eV to 1.490 eV. By increasing the excitation power, the system undergoes a succession of two-phase transitions, first breaking the strong coupling of the exciton photon. This can be observed by the polaritonic (fig. 6.6 (a)) and photonic dispersion (fig. 6.6 (b)) when the system is in the strong- and weak-coupling regime, respectively. Then the system evolves in the weak-coupling regime until it finally attains the laser phase transition due to the onset of the stimulated emission of photons into the cavity photon mode. This is observed by the superlinear transition in the input-output light above the threshold power P_{th} in fig. 6.7 (a). Two effects come into play with carrier density, the energy blueshift of the exciton states due to the repulsive nature of the interactions and the renormalization of the bandgap in reaching the Mott transition to the phase transition from the exciton gas to electron-hole plasma [110]. The

photon lasing takes place when the gain for the photon modes exceeds their losses.

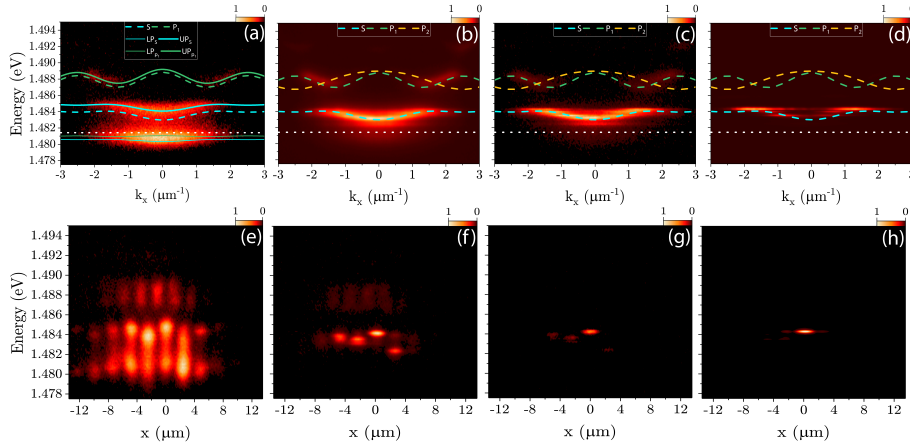


FIGURE 6.6: **Emission spectra under nonresonant excitation with a 3 μm spot size.**

The energy-resolved emission measured in momentum space along the $\Gamma - K$ direction (a)–(d) and the corresponding spectra measured in real space along the x -direction (e)–(h) for four excitation powers: (a), (e) $P = 3$ mW in strong coupling, (b), (f) $P = 70$ mW in weak coupling, (c), (g) $P = 90$ mW, the lasing threshold power and (d), (h) $P = 130$ mW in the lasing regime. The calculated energy dispersion of lower and upper polaritons for the S and P bands (solid lines) and the corresponding photonic bands (dashed lines) are plotted in (a)–(d).

In fig. 6.7 (b), we plot the emission's energy as function of laser power at $k = 0$ of the LP and UP modes in the strong-coupling case and the cavity photon in the weak-coupling case. In the lasing regime, we plot the energy of the confined lasing modes (fig. 6.6 (c) and (d)). We show the specific features characterizing the three regimes with rising excitation power: the energy renormalization of the LP and UP modes with their linewidth broadening in the strong coupling, the linewidth narrowing of the photon-mode emission across the weak-coupling regime, and three modes with a sharp linewidth characterizing a laser emission. Also, a blueshift in the laser emission is evidenced by the increasing pump power and the carrier density, which originates from a decrease in the active region's refractive index.

The different regimes' characteristics are highlighted by the emission spectra in momentum and real space in fig. 6.6 for different excitation powers, respectively, in fig. 6.6 (a) – fig. 6.6 (d) and fig. 6.6 (e) – fig. 6.6 (h). The energy dispersion of the LP and UP bands and that of the photonic bands are plotted, respectively, in fig. 6.6 (a) for the strong- coupling regime and in fig. 6.6 (b) – fig. 6.6 (d) for the weak- coupling regime, including the calculated polaritonic and photonic S and P bands. In real space, the emission shows an extended

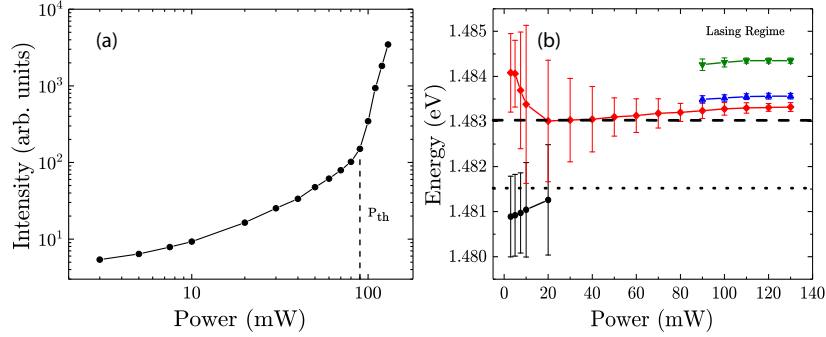


FIGURE 6.7: **Photon lasing in triangular polaritonic lattice under nonresonant excitation with a $3\ \mu\text{m}$ spot centered on top of a mesa.** (a) Integrated emission intensity as a function of excitation power. The lasing phase transition is evidenced by the threshold in the power dependence (P_{th}). (b) The emission energy at $k = 0$ of the lower (black) and upper (red) polariton in strong coupling and of the cavity photon (red) in the weak coupling; in the lasing regime, the energy of the confined lasing modes. Their linewidth is represented as error bars. The dotted (dashed) horizontal line is drawn at the exciton (photon) energy at $k = 0$.

distribution in the strong-coupling regime (fig. 6.6 (e)), which reveals the propagation of polaritons outside the excitation region. In the weak-coupling regime toward the laser phase transition, however, the spatial extension of the emission decreases (fig. 6.6 (f) and fig. 6.6 (g)) and discrete photonic modes eventually appear in k space (fig. 6.6 (c)). The laser emission emerges with distinct modes, and ultimately the main emission arises at the edge of the Brillouin zone (fig. 6.6 (d)) like a gap soliton, the emission of which is becoming localized mainly on one single mesa (fig. 6.6 (h)).

Near the edge of the Brillouin zone, the dispersion becomes anomalous (negative band curvature); therefore, a self-defocusing nonlinearity is needed to localize a mode. The carrier density generated by the pump excitation $I(r)$ induces a local change of the GaAs refractive index, n_0 through the Kerr effect: $n(r) = n_0 + n_2 I(r)$. Inside the energy gap of GaAs, the Kerr coefficient $n_2 < 0$ is negative [111]; thus, when $I(r)$ is increased, the local refractive index decreases and hence an effect of self-defocusing occurs. Consequently, a localized defect like state arises near the edge of the Brillouin zone. The local reduction of the refractive index induces the energy blueshift fig. 6.7 (b) into the bandgap fig. 6.6 (d). This confined gap state is known in photonic crystals as a gap soliton.

We can identify two stages to the localization of the photonic modes: the first one corresponds to the photonic defect's creation, by the local breakdown of the strong-coupling regime, which causes a self-trapping of the photons, and the second one to the onset of lasing. In order to better evidence this

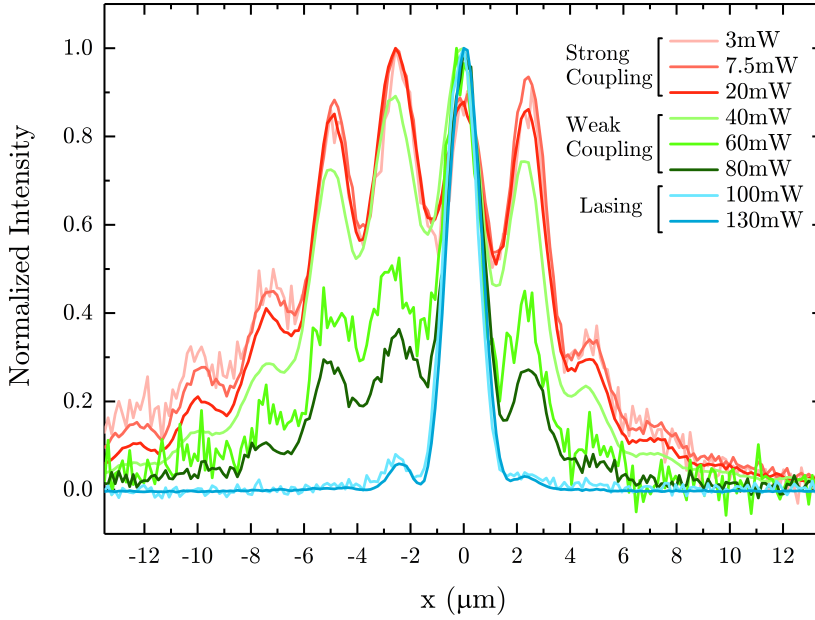


FIGURE 6.8: **The evolution of the emission's spatial distribution under nonresonant excitation at different powers.** The $3\ \mu\text{m}$ laser spot is on the mesa at $x=0$.

sequential localization, we represent in fig. 6.8 the evolution of the emission's spatial distribution as the excitation power increases across the three regimes; strong coupling, weak coupling, and lasing regimes. At the lowest excitation power, the emission occurs over a large number of mesas distributed around the central excitation spot (mesa at $x=0$). The expansion away from the excitation spot corresponds to the polaritons' expansion over a range, determined by the polariton lifetime and the polaritons distribution in k -space. In the intermediate power range corresponding to the weak-coupling regime, the emission's spatial distribution shrinks down as the excitation power is raised. This shrinkage of the spatial distribution corresponds to the photonic defect's evolution within the region experiencing the weak coupling. At a power of 60 mW, still well below the lasing threshold power, one observes a drastic reduction of the emission intensity from all the mesas surrounding the excitation spot, which evidences photons' self-trapping. This is a manifestation of the local increase of the photon density, which is largest next to the excitation spot. In the last stage, as the power reaches the lasing threshold, the spatial extent of the emission collapses onto the central mesa (the mesa at $x=0$ position).

The breaking of the strong-coupling regime inside a small excitation area perturbs the lattice's periodicity and generates a defect. The arrangement and the number of mesas in this defect area define the extent of the photonic

modes. The decrease of propagation losses outside this region favors the increase of the photon density by spontaneous emission due to electron-hole recombination, optimizing the buildup of the photon-mode gain. We validate the photon lasing action's dependence on the induced defect by controlling the optical excitation position on the patterned sample experimentally.

The excitation position's impact on the generation of the defect and the lasing emission is evidenced in fig. 6.9. The number of mesas composing the defect, which we outline in yellow in fig. 6.9 (a), fig. 6.9 (c), and fig. 6.9 (g), is found to strongly depend on the position of the laser spot (identified as a red circle). It lies either on top of a mesa (fig. 6.9 (a)) or among three (fig. 6.9 (c)) or four (fig. 6.9 (g)) mesas. In fig. 6.9 (b), we display the spatial distribution of the total emission intensity integrated in energy when the excitation spot is on top of a mesa (corresponding to the conditions of fig. 6.6 (d) and fig. 6.6 (h)). the predominant emission arises then from one mesa surrounded by six weakly emitting mesas. The defect's spatial shape involves seven mesas altogether, it is the hexagon formed by the six nearest-neighbor mesas surrounding the mesa from which most of the lasing-mode emission originates. We highlight the defect extension by a hexagon that contains the mesas emitting in the weak-coupling regime (fig. 6.9 (b)). In fig. 6.9 (d) and fig. 6.9 (h), we display the spatial distribution of the total emission intensity similarly when the excitation position is displaced off a mesa and is surrounded by either three (fig. 6.9 (d)) or four (fig. 6.9 (h)) mesas. We observe distinct emission patterns spread over several mesas. We reproduce the emission zone and the mesas' arrangement involved in the defect formation by superposing the hexagons built from the six nearest- neighbor mesas of each mesa constituting the group of three (green) and four (blue) mesas in fig. 6.9 (c) and fig. 6.9 (g). Therefore, the generated defect shapes differ from one to the others [fig. 6.9 (a), fig. 6.9 (c) and fig. 6.9 (g)]. We represent in fig. 6.9 (d) and fig. 6.9 (h) the contour of the defect zone with the emitting mesas inside.

We plot the corresponding measured energy of the lasing emission in momentum (fig. 6.9 (e) and fig. 6.9 (i)) and real (fig. 6.9 (f) and fig. 6.9 (j)) space, for which the emission pattern of mesas in real space and their momentum distribution can be associated. We can identify mainly two lasing supermodes originating from the mesas' coupling inside the defect region. From this comparison, we infer that the defect's configuration during its generation ultimately defines the emission mode and its characteristic spatial distribution. With these results, we highlight the possibility of controlling the defect geometry and, ultimately, the lasing mode.

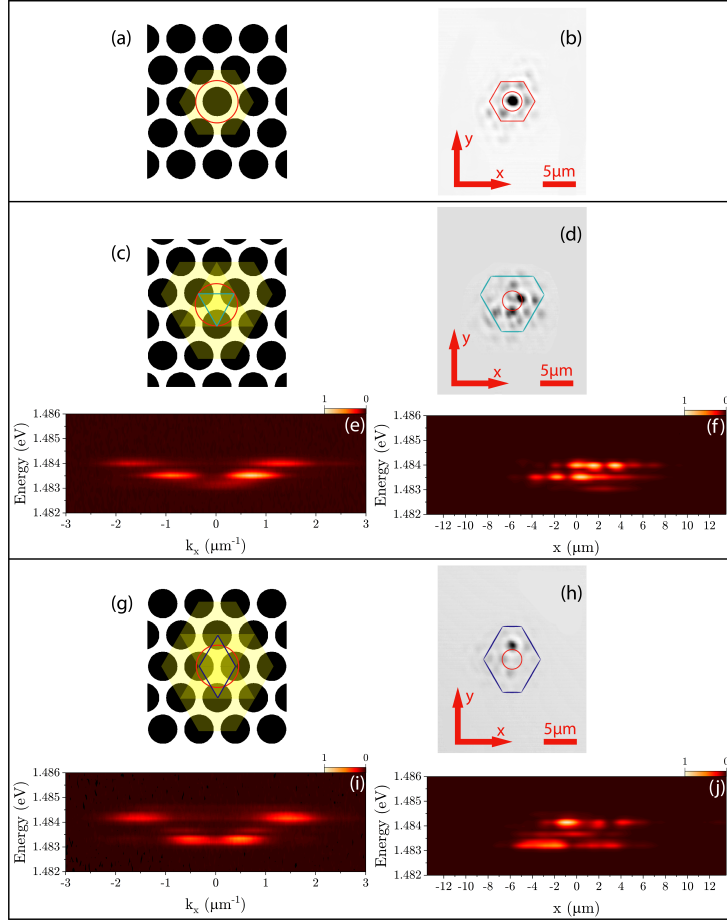


FIGURE 6.9: Photon lasing and the induced defect with the optical excitation's position. Triangular photonic lattice representation with the excited area for three different positions of the laser spot of $3\ \mu\text{m}$ size: (a) excitation on top of a mesa (red circle), (c) among three mesas (green triangle), and (g) among four mesas (blue lozenge). The hexagons drawn in yellow are composed of the excited mesas and their six nearest neighbors; they define the region in which the defect is generated. (b), (d), (h) correspond to the energy-integrated emission in real space. The emission spectra are measured in momentum space along the $\Gamma - K$ direction (e), (i), and in real space along the x -direction (f), (j) for the excitation conditions defined respectively in (c), (g). For the excitation condition defined in (a), the spectra are shown in fig. 6.6 (d) and fig. 6.6 (h). Excitation power $P = 130\ \text{mW}$. A red circle represents the position of the excitation spot. In (b), (d), and (h), the defect is highlighted by the contour zone enveloping the emitting mesas.

6.5 ANDERSON LOCALISATION IN MICROCAVITY POLARITONS

The concept of Anderson localization [112] in solid-state physics predicts that the electrons become immobile when located in a disordered lattice, and the material behaves as an insulator instead of a conductor. The effect's origin is the interference among multiple electron scatterings by random defects in the lattice potential. The extended electronic Bloch wave function alters to an exponentially localized one if the randomness is strong enough [113]. A similar phenomenon is predicted for multiple scattering of electromagnetic waves; unlike electrons, photons do not interact with each other [114–118].

We present an experimental signature of the Anderson localization of microcavity polaritons under non-resonant excitation and provide a systematic study of disorder strength dependence. We reveal a controllable localization degree, characterized by the inverse participation ratio (IPR), by tuning the positional disorder of interacting two-dimensional mesas' arrays in a set of eight triangular lattices with increasing levels of static disorder. The static off-diagonal disorder is introduced by adding a random displacement to each lattice site with maximum controllable amplitude. The localization is characterized by the inverse participation ratio and is shown to increase as a function of disorder strength monotonically. This constitutes the realization of disorder-induced localization in a driven-dissipative system.

The sample is the same as discussed in section 6.1.1. To introduce an off-diagonal disorder to the system, a random value offsets the cartesian coordinates of the mesas in the range $d[-\delta, \delta]$ where $0 \leq \delta \leq 1$ parameterizes the amount of disorder, and $d = 0.25 \mu\text{m}$ is the maximum possible displacement for the maximum disorder $\delta = 1$ (fig. 6.10). We consider eight different disorder levels from $\delta = 0$ to $\delta = 1$ in evenly spaced steps.

We excite the system non-resonantly with a 660 nm CW laser, focused on 25 μm spot size. We measure the sample's photoluminescence with a collection lens of numerical aperture 0.42NA and image the real-space integrated energy emission in a CCD.

The non-resonant excitation of the CW laser creates a reservoir of excitons that feed the polariton population. From the photoluminescence images of the perfect triangular arrays, fig. 6.11 (a), we see the confinement of polaritons predominantly within the mesas and an approximately homogeneous distribution among them.

The positional disorder modifies the eigenstates of the system from Bloch states towards spatially separated patches of localization. The effect of the disorder on the localization, or clustering, of the polariton population, can be seen in the photoluminescence images, fig. 6.11 (a–d).

To obtain a quantitative measure of the localization amount, we calculate the inverse-participation ratio (IPR). The IPR has previously been used to quantify Anderson localization in photonic systems [118] and is also applicable here. In essence, it is a measure of inhomogeneity, and for a homogeneous distribution,

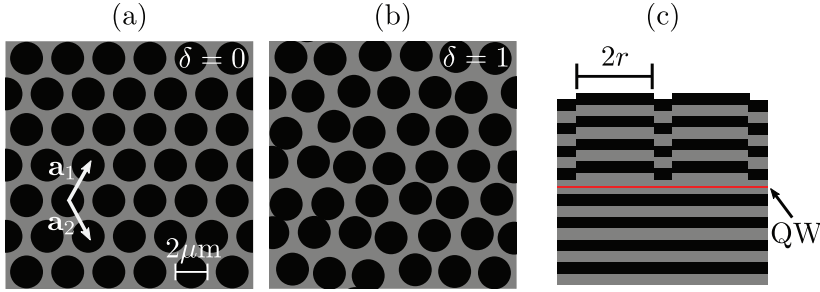


FIGURE 6.10: **Schematic of the triangularly patterned sample.** (a) no disorder $\delta = 0$ and (b) maximum disorder $\delta = 1$ with the lattice vectors $\mathbf{a}_{1,2} = (a/2)(1, \pm\sqrt{3})$. (c) A side view of the sample with epitaxial layers, DBRs, and the embedded quantum well (QW).

it is equal to unity. Thus, as Anderson localization's onset causes some mesas to contribute more significantly to the total photoluminescence, the IPR increases also. To exploit this measure, we first normalize the data to account for the Gaussian background fig. 6.12 and then calculate the average occupation $I_n = \int_{\text{mesa}_n} |\psi|^2 d\mathbf{r}$ of each mesa (labelled by n). We then obtain the IPR as

$$\mathcal{I} = N \left(\sum_{n=0}^N I_n^2 \right) / \left(\sum_{n=0}^N I_n \right)^2 \quad (6.8)$$

Figure 6.11 (i) shows the percentage change in the IPR from no disorder ($\delta = 0$) to maximum disorder ($\delta = 1$). We clearly see the increase in IPR with increasing disorder δ , which signals the onset of localization. The error bars correspond to the standard error after repeating the experiment on 12 different regions sampled from a larger lattice for each disorder strength. Besides, similar results have been reproduced for several different laser powers fig. 6.13. We recover the same monotonic increase in IPR with the position disorder.

We successfully modeled the experimental results with a generalized Gross-Pitaevskii equation [119] describing the evolution of the polariton wavefunction $\psi(\mathbf{r}, t)$

$$i\hbar \frac{\partial \psi}{\partial t} = \left[-\frac{\hbar^2 \nabla^2}{2m} + \frac{i\hbar}{2} (Rn_R - \gamma) + \hbar g |\psi|^2 + V \right] \psi \quad (6.9)$$

where m and γ are the effective mass and decay rate of the polaritons, g is the strength of polariton-polariton interactions, R is the reservoir-polariton exchange rate, and $V(r)$ is the potential landscape defined by the lattice. The reservoir $n_R(\mathbf{r}, t)$ is described by the rate equation

$$\frac{\partial n_R}{\partial t} = -(\gamma_R + R|\psi|^2) n_R + P \quad (6.10)$$

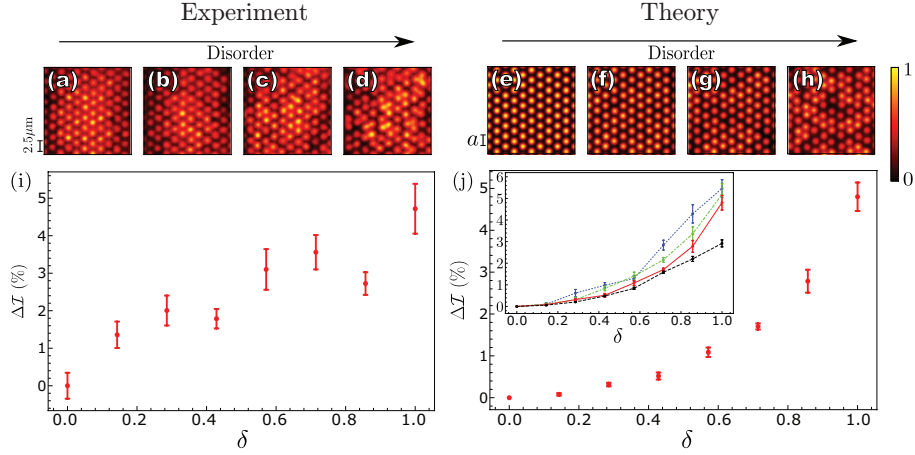


FIGURE 6.11: **Localization signature.** Figures (a–d) show the real-space photoluminescence images under weak ($P = 75 \text{ mW}$) nonresonant excitation, whereas figures (e–h) show the polariton density in the numerical model. In both cases, the results are normalized to account for the Gaussian pump distribution and the disorder levels are (a,e) $\delta = 0$, (b,f) $\delta = 0.284$, (c,g) $\delta = 0.572$, (d,h) $\delta = 1$. In the absence of disorder we see a more homogeneous distribution among the mesas, whereas disorder induces the onset of patches of localisation. Also shown are plots that reveal how the IPR increases with disorder for (i) experiment, and (j) theory. The polariton nonlinearity in (j) is $g = g_0 = 2.4 \times 10^{-3} \text{ meV} \cdot \mu\text{m}^2$. The inset of (j) shows the result for $g = -g_0$ (blue dotted line), $g = 0$ (green dot-dashed line), $g = g_0$ (red solid line), and $g = 10g_0$ (black dashed line). The simulation parameters are $m = 5 \times 10^{-5} m_e$, $\hbar R = 0.4 \text{ meV} \cdot \mu\text{m}^2$, $\hbar\gamma = 0.5 \text{ meV}$, $\hbar g = 2.4 \times 10^{-3} \text{ meV} \cdot \mu\text{m}^2$, $V_0 = 9 \text{ meV}$, $\hbar\gamma_R = 2 \text{ meV}$, and $P_0 = 2\gamma_R\gamma/R$. Here, V_0 is the maxima of the trapping potential, which we model as a radially symmetric sigmoid function for each mesa. In the experimental figures the cavity-exciton detuning is 2 meV

Where γ_R is the decay rate of the reservoir. The reservoir is populated by the continuous-wave pump $P(r)$, which we model as a Gaussian with amplitude P_0 . We use the Runge-Kutta method of fourth-order to evolve the dynamics until a stationary solution is achieved (approximately 50 ps). In fig. 6.11 (e–h), we show these simulations' results for periodic and increasingly disordered arrays. We can see the onset of patches of localization when a disorder is introduced. We calculate the IPR using eq. (6.8) in much the same way as is done for the experimental data and plot the results in fig. 6.11 (j). Despite the fact that this model is to simulate a condensate, which is not the case in our experiments, it qualitatively reproduces the experimental outcomes.

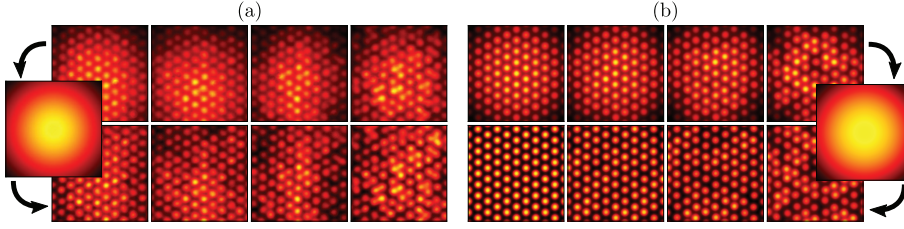


FIGURE 6.12: **Normalisation procedure.** We show (a) experimental photoluminescence and (b) simulation results, exactly corresponding to those shown in fig. 6.11. The top row shows the results before background renormalisation, whereas the bottom row exactly corresponds to the figure in the main text. The insets show the background used.

In the inset of fig. 6.11 (j) we show calculations performed for different polariton-polariton nonlinearities. The green dot-dashed line shows the linear regime ($g = 0$). In the present experiment, we are working in a weak non-linearity regime, which we model with a small g ($g > 0$) in the simulations (solid red line). Nonetheless, we observe that the repulsive interaction acts to suppress the localization; see the black-dashed line increasing the nonlinearity ten-fold. Also, we show that attractive interaction ($g < 0$) acts to enhance the localization (blue dotted line). Although a negative g is not possible with our experimental setup, such a regime could be accessed with spinor condensates tuned near the Feshbach resonance.

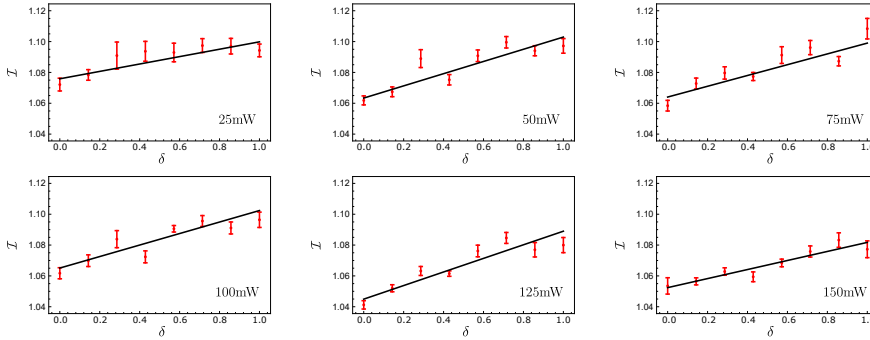


FIGURE 6.13: **IPR plots for different excitation powers.** Error bars are the Standard Error of the Mean (SEM). A straight line is fitted with the least errors method, weighted by $1/(SEM)^2$.

In order to investigate the ability to tune the localization, we show in fig. 6.14, the theoretical results performed by varying different parameters in the polariton system.

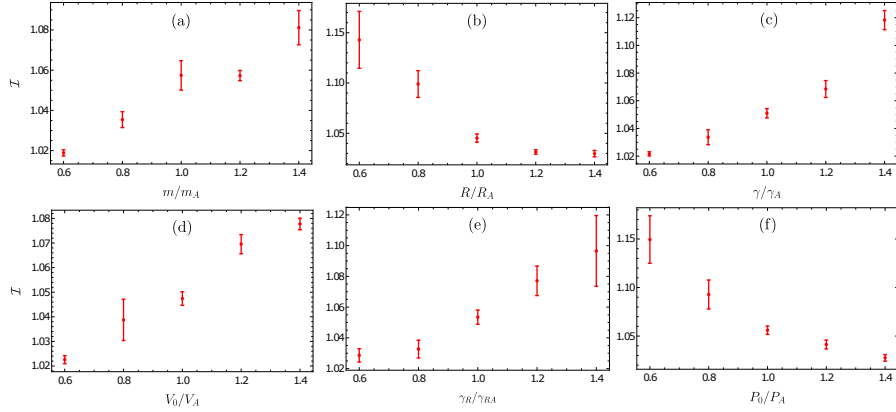


FIGURE 6.14: **IPR variation with parameters of Gross-Pitaevskii model.** In figures (a-f) we tune each of the shown parameters from 60% to 140% of that value used in the main model. $m_A = 5 \times 10^{-5} m_e$, $\hbar R_A = 0.4 \text{ meV} \cdot \mu\text{m}^2$, $\hbar \gamma_A = 0.5 \text{ meV}$, $\hbar g = 2.4 \times 10^{-3} \text{ meV} \cdot \mu\text{m}^2$, $V_A = 9 \text{ meV}$, $\hbar \gamma_{RA} = 2 \text{ meV}$, $P_A = 2 \gamma_R \gamma / R$, $d = 0.25 \text{ nm}$, and $L = 88 \mu\text{m}$.

In conclusion, we demonstrate photon lasing's realization integrated into a polaritonic lattice for which the lasing mode can be optically controlled. The scheme is based on the optical breaking of the translational symmetry through the local transition from the strong- to the weak-coupling regime of the exciton-photon system created inside a semiconductor microcavity patterned with a triangular lattice of mesas. In this way, we demonstrate self-trapping of light and localized photon lasing. The lasing modes originate from the photonic confinement and photon propagation interplay, which can be controlled by the excitation position. These results open the way for the realization of localized mode lasers of chosen geometry, in which the shape of the generated defect determines the lasing mode.

In the last part of the chapter, our results propose a signature of disorder-induced localization in the steady states of driven-dissipative systems, a regime entirely separate from the closed systems' prototypical case. We believe that the phenomenology stated here should be generally observable in other driven-dissipative systems. In addition, since both polaritons and localization are foreseen to have a high potential for applications in optoelectronic devices and quantum information, respectively, such a robust and controllable phenomenon could be of use in novel devices.

6.6 PERSPECTIVES

This chapter was devoted to studies on photonic localization in polariton lattices landscape. Based on our findings, we would like to give some viewpoints to new research on polariton localization physics.

6.6.1 *Optically Controlled Photonic Defect*

We demonstrate photon lasing's realization integrated into a polaritonic lattice for which the lasing mode can be optically controlled. The scheme is based on generating a photonic defect by breaking the translational symmetry optically through the local transition from the strong- to the weak-coupling regime of the exciton-photon system.

These results open the way for the realization of localized mode lasers with arbitrary geometry, in which the shape of the generated defect determines the lasing mode.

Our scheme can also be extended to realize orbital angular momentum microlasers [120] integrated into a two-dimensional semiconductor honeycomb-patterned microcavity. The emission chirality could be controlled by the position and polarization of the circularly polarized optical excitation, which spin-polarized the gain medium. This can be controlled on the ultrashort time scale imposed by the carriers' time relaxation, which of the order of picoseconds. Ultrafast switch and memory devices could be imagined using this approach.

We show localization in a triangular lattice, which can be generalized to other lattice configurations. However, the defect configuration will be modified due to the mesas' disposition that is part of the defect. For example, in a hexagonal (rectangular) lattice, we can envision a defect as either a hexagon (square), if the excitation is made in the center of one hexagon (square) or kind of "Y" ("+") if the excitation sits on top of a mesa.

It is feasible to develop drop and add filters [121, 122] and dynamic photon pinning [123] using optically controlled defect cavities and line-defect waveguides in two-dimensional polaritonic lattices. In the filters, propagating photons along with a line defect (as a waveguide), are trapped by a single-point defect optically created in a two-dimensional lattice when the photon frequency matches the defect frequency. An optically generated defect can pin traveling photons in a waveguide similar to a cavity. One might also conceive the realization of PT (parity and time-reversal) symmetry breaking with local optical control of gain and loss [124, 125].

6.6.2 *Exploration of New Physics with Disorder Localization*

We present an experimental signature of the Anderson localization of microcavity polaritons. We investigate the steady-state polariton distribution under non-resonant excitation in triangular lattices with increasing levels of static disorder.

To advance our work, it would be interesting to investigate the localization of strongly interacting polaritons. For example, one could explore the interplay between the disorder-induced localization seen herein and effects such as nonlinear localization observed for strongly driven microcavities [126]. Moreover, with larger polariton densities, it may be possible to extract signatures of many-body localization, which is roughly the persistence of Anderson localization in the presence of many-body interactions.

Polaritonic Feshbach resonances can be used to control the strength and character (attractive or repulsive) of the polariton interaction. It would be useful to generate a spin-polarized polariton population and investigate the antiparallel spin polariton population's localization. The role of the interaction on the disorder-induced localization can be considered in this way.

One could also explicitly examine the role of localization in driven-dissipative systems for preserving the memory of initial conditions, for instance, by preparing initially imbalanced population distributions with a highly inhomogeneous pumping, switching on a homogeneous pumping may influence the persistence of the initial state. Different pump polarizations could also be used to investigate the role of attractive and repulsive interactions in the effect of memory.

Resonant excitations could be used to generate a coherent polariton population. It would be appealing to shine the sample quasi resonantly with a large spot size CW laser beam and use a small spot size laser to trigger the polariton system in a bistable regime [10, 127]. The locally generated bistable area propagates further through the structure. In this way, one will selectively access the propagation and localization of polaritons in a given band. Using different excitation angles, we can scrutinize the dispersion effect on the propagation and localization of polaritons.

6.6.3 *Polariton Multistability*

We propose utilizing the spatial multistability [128] to study the propagation and localization of polaritons in distinct energy bands. It will be possible to examine the different spatial geometry in polaritons emission in separate bands thanks to spatial multistability. For instance, in honeycomb lattices, the real space polariton emission from the s-band and p-band correspond to hexagonal and kagome geometry, respectively [98]. Furthermore, the s-band is usually dispersive, and the p-band can become a flat band for which the states

are localized. We can then alter the propagation of polaritons and induce their localization in a multistable cycle.

We believe that the phenomenology reported here may open a new chapter for basic science explorations and could have a high potential for applications in optoelectronic devices and quantum information.

Microcavity polaritons emerging from the strong coupling between cavity photons and quantum well excitons are hybrid quasiparticles, which provide nonlinear behavior due to excitonic interactions. At the same time, the photonic component allows studying their quantum correlations through their emission to reach polariton blockade, for instance. The strong polariton-polariton interaction is crucial to achieving this regime in which the presence of one polariton blocks the entrance of a second one. One way to enhance interactions is to confine polaritons strongly. This chapter is devoted to polaritons tightly confined in a quantum box. We start by giving an overview of the photon blockade and the framework for the achievement of polariton blockade. Next, we describe the engineered microcavity structures with sub-micron size mesas for strong confinement of polaritons. Finally, we explain the experiment, including a Hanbury Brown and Twiss (HBT) set up for measuring photon correlations. We end the chapter with experimental results and conclusions.

7.1 POLARITON BLOCKADE

Photon blockade, proposed three decades ago [41], is a nonlinear optical effect in which the photon-photon interactions mediated by the nonlinear medium warrant that only one photon exists in a single-mode cavity. The photon blockade effect was extended to various schemes using a single intracavity atom by exploiting a multi-state electromagnetic induced transparency [129–132] and using a two-state atom coupled to a cavity mode [133, 134]. Photon blockade was experimentally observed in the regimes of strong atom-cavity coupling [135] and a quantum dot strongly coupled to a photonic crystal resonator [136–138], and in microwave regime with a single superconducting artificial atom strongly coupled to a transmission line resonator [139]. The effect is even generalized to the use of matter waves instead of optical waves with the prediction of atom blockade effect [140], in which only one atom could occupy the cavity mode.

Theoretically, it is predicted that when polaritons, these composite exciton-photon quasiparticles, are confined in a small volume, the polariton-polariton interaction could be sufficient to reveal polariton blockade [40]. In the polariton blockade regime, a photon enters the cavity generating a polariton, preventing other photons from entering and converting to new polaritons. Different schemes were proposed to overcome the difficulty of attaining very small volume confinement. One is to use a system of two-coupled modes.

This unconventional photon blockade [141, 142] utilizes destructive quantum interference between two paths, which cancels the probability of having two photons in one of the modes. The other theoretical proposition is to use polaritonic Feshbach resonance [31, 47] in which the coupling between polariton and biexciton plays a role in the blockage [143]. Very recently, two different groups [144, 145] evidenced the first signs about strong interacting polaritons. They used a semi-integrated fiber cavity; the fiber's concave surface leads to lateral confinement of 2 μm diameter. They measured with this confinement an antibunching of 0.95 of the transmitted light across the cavity. Nevertheless, these findings offer encouraging perspectives regarding the realization of strongly interacting photonic systems; the demonstration of polariton blockade has to be still provided.

The polariton interaction strength depends on the polariton confinement. Stronger confinement favors an optimal overlap of the exciton wavefunctions, enhancing the nonlinearity of polaritons since their excitonic content mediates polariton interactions. The repulsive character of the polariton interactions induces an energy blueshift of the polariton resonance. The polariton blockade is possible when the photonic confinement volume is small enough to improve the nonlinearity of polaritons in the regime in which the presence of one polariton will block the resonant entering of a second one as the resonance energy shifts by an amount of the order of the linewidth. The nonlinear behavior of polaritons is due to their excitonic interactions; their photonic component allows detecting their emission in the polariton blockade regime as a single photon emitter.

The experiment's principle to investigate polariton blockade and study quantum correlations between polaritons is displayed in fig. 7.1. The fundamental polariton mode is resonantly excited by tuning the laser wavelength across one-polariton state $|1p\rangle$ energy from red to blue detuning. The energy renormalization brings the two-polariton state $|2p\rangle$ resonance to a higher energy than twice the one-polariton state's energy $2 \times |1p\rangle$. When a photon from the red detuned laser excites a polariton, a second photon cannot excite the two-polariton state during the polariton lifetime. However, with the blue detuned laser, a second photon can reach the two-polariton state. Therefore, the probability of generating a second polariton in the former (latter) situation is decreased (enhanced).

In order to characterize the polariton emission, the transmitted light is split into two and is sent to a Hanbury Brown and Twiss (HBT) set up for measuring photon correlations quantified by the behavior of the zero-delay second-order coherence function $g^{(2)}(\tau = 0)$. In a strong nonlinear regime, when the energy is renormalized by an amount more considerable than the polariton linewidth, by redshifted laser excitation, ideally, only a single photon will be emitted. Therefore, in this regime, the emitted light will be strongly anti-bunched, and the $g^{(2)}(\tau = 0) = 0$. The closer the measured value of the $g^{(2)}(\tau = 0)$ to zero gives the increase in the probability to generate only one polariton and,

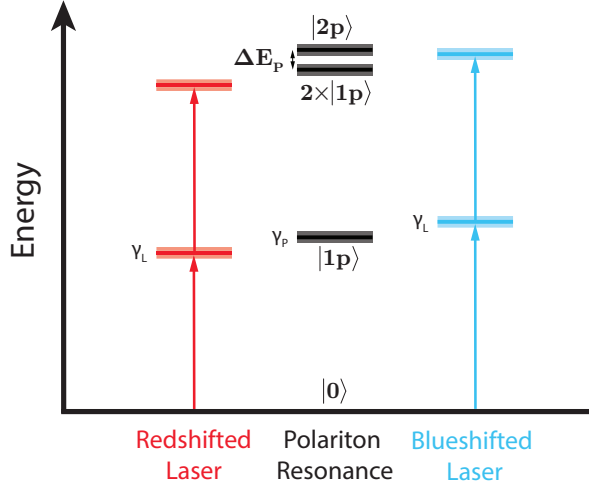


FIGURE 7.1: **Polariton excitation ladder.** The one-polariton mode $|1p\rangle$ is resonantly excited. Due to polariton-polariton repulsive interaction, the polariton energy renormalization ΔE_p brings the two-polariton state $|2p\rangle$ to higher energy than twice the energy of one-polariton state $2 \times |1p\rangle$. When $\Delta E_p \approx \gamma_p$, with photon excitation red detuned, a second photon with the same wavelength cannot excite $|2p\rangle$ state. However, with the blue detuned photon, a second photon with the same wavelength can reach the $|2p\rangle$ state. γ_p and γ_L are polariton linewidth and laser spectral width.

therefore, the reduction in the probability to generate simultaneously two polaritons. By considering only the lower polariton mode, the Hamiltonian in the polariton basis reads [145]

$$\mathcal{H} = \hbar\Delta\omega_L \hat{p}^\dagger \hat{p} + \frac{U_{pp}}{2} \hat{p}^\dagger \hat{p}^\dagger \hat{p} \hat{p} + F(t) \hat{p}^\dagger + F^*(t) \hat{p} \quad (7.1)$$

The energy of the one-polariton state is $\hbar\omega_p$ and the lasing detuning is given by $\Delta\omega_L = \omega_L - \omega_p$. \hat{p} (\hat{p}^\dagger) is the polariton annihilation (creation) operator $\hat{p} = \mathcal{C}\hat{c} + \mathcal{X}\hat{x}$ in which \mathcal{C} and \mathcal{X} are the Hopfield coefficients that give the photon and exciton fraction of the polariton. $U_{pp} = U\mathcal{X}^4$ is the strength of the polariton-polariton interaction, and U is the strength of the exciton-exciton interaction.

In a spatially confined mesa geometry, the interaction strength U_{pp} is quantified as $U_{pp} \propto (2r^2)^{-1}$ showing an inverse proportionality with the lateral

area of the photonic mode [40]. The second-order photon correlation function at zero-delay is

$$g^{(2)}(0) = \frac{\langle \hat{c}^\dagger \hat{c}^\dagger \hat{c} \hat{c} \rangle}{\langle \hat{c}^\dagger \hat{c} \rangle^2} = \frac{1}{\left(1 + 4 (U_{pp}/\gamma_p)^2\right)} \quad (7.2)$$

which quantifies the ratio of having two photons on a single site. The figure of merit of the anti-bunching is the ratio U_{pp}/γ_p , where γ_p is the linewidth of the polariton mode [146]. Therefore, strong polariton interaction strength and narrow polariton linewidth are crucial to accomplish the polariton blockade. Notably, strong confinement is necessitated, and it has been the principal technical obstacle preventing a genuine regime of strong nonlinearity of polaritons. We overcame this issue with the achievement of submicron-sized mesas to confine polaritons laterally.

7.2 SAMPLE

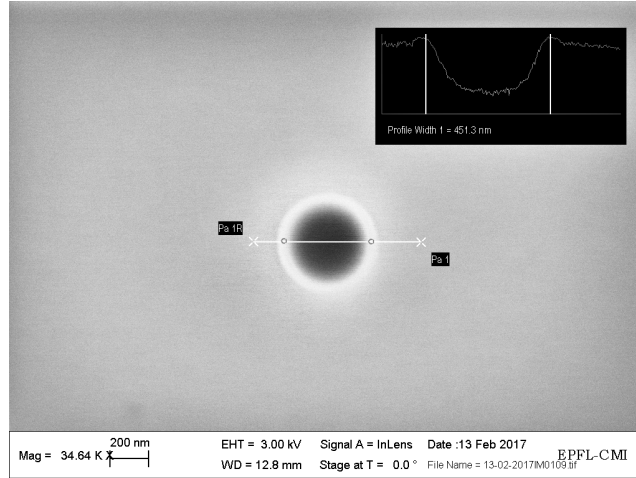


FIGURE 7.2: **SEM Image of the sample.** Scanning electron microscope image of the exposed pattern on the sample by electron beam lithography.

The sample was grown by molecular beam epitaxy. The microcavity is a GaAs λ -cavity made of 24/20 pairs of GaAs/AlAs distributed Bragg reflectors (DBR). A single $\text{In}_{0.04}\text{Ga}_{0.96}\text{As}$ quantum well is placed at the antinode position of the electromagnetic field in the middle of the microcavity. The spacer layer is patterned before the growth of the second DBR of the cavity [39]. We have used electron-beam lithography to write the patterned submicron-sized mesas. A scanning electron microscope (SEM) image of the exposed structure on a sample by electron-beam lithography is shown in fig. 7.2. The photon traps

are mesas, which consist of 400 nm to 2 μm in diameter and local elevation of 20 nm high of the spacer layer. The mesa elevation leads to a local decrease of the microcavity resonance and a photonic confinement potential of 30 meV. The strong coupling between the exciton and the confined photonic mode gives rise to a Rabi splitting of $\Omega_R = 3.1 \text{ meV}$ with the exciton energy of $E_X = 1.47759 \text{ eV}$.

7.2.1 Characterization

We probe the spectral emission of the sample for different mesa sizes at several detunings. We measure the luminescence of the sample under nonresonant excitation in reflection configuration to characterize the mesas. The experimental setup is displayed in fig. 7.3. The sample is placed in a cryostat with a

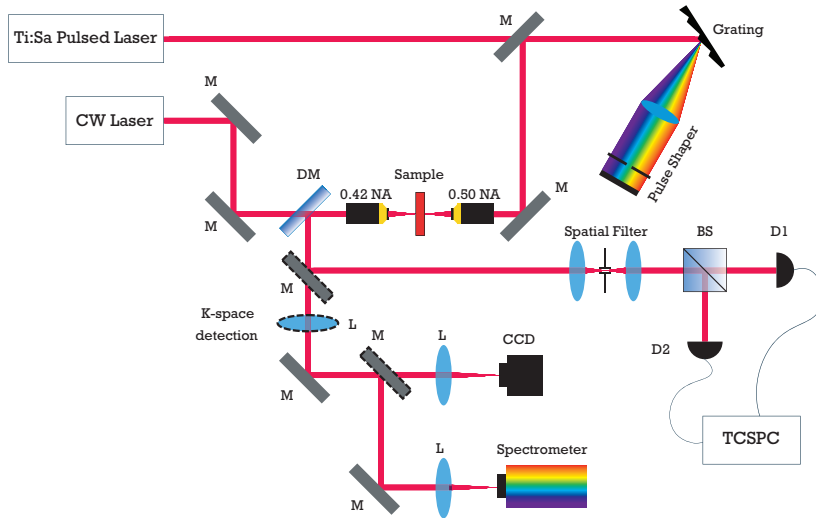


FIGURE 7.3: **Experimental setup.** The 660 nm CW laser is used to excite the sample nonresonantly. The broadband Ti:Sapphire pulsed laser is spectrally narrowed by a pulse shaper and sent to excite the sample resonantly at normal incidence. The mesa's transmitted signal passes through a real-space filter and is sent to the Hanbury Brown and Twiss (HBT) detection scheme for photon correlation measurements. Photon events are registered with time-correlated single-photon counting (TCSPC) coincidences and electronics treated in real-time. DM, dichroic mirror; M, mirror; L, lens; BS, beam splitter; D1 and D2, single-photon detectors. Movable parts (lenses and mirror) are drawn with dashed lines.

continuous-flow of liquid helium at a cryogenic temperature of 4 K. In order to measure the luminescence, we excite the sample on the top side nonresonantly with a CW laser operating at 660 nm with a spot size of 3 μm , which is larger than the mesa size to warranty homogeneous excitation of the mesa.

The laser beam is focused through a $\times 50$ objective and numerical aperture 0.42NA. The sample's emission is collected in reflection configuration with the before-mentioned objective. In order to control the position of the excitation and the stability of the measurements, the emission is focused with a lens of 400-mm focal length on a CCD camera, which results in a magnification of 100, for imaging the sample surface with the excitation laser spot. The spectrally resolved emission is obtained either in the near-field or in the far-field by imaging the sample surface plane or the Fourier plane of the microscope objective on the spectrometer's entrance slit coupled to a CCD camera.

In order to excite the sample resonantly, a broadband Ti:Sapphire pulsed laser is spectrally narrowed by a pulse shaper and focused on the back of the sample at normal incidence with a $\times 50$ objective (0.5 NA). The emission in transmission configuration is collected by a $\times 50$ objective (0.42NA) and send either to the spectrometer or to the Hanbury Brown and Twiss (HBT) detection part for the photon correlation measurements. The photon stream is split into two by a 50/50 beam splitter, and each separated beams enter in a fiber-coupled to a single-photon detector (ID Quantique 120) connected to a coincidence counter. The detector has a quantum efficiency of 65% (at 840 nm) and timing jitter of 400 ps (at 650 nm) plus a dead time of 1 μ s. Since the APDs (avalanche photo detectors) have a much larger timing jitter than the polariton lifetime, they cannot be used to measure under CW laser excitation, so we excite the system with pulse-width similar to the polariton lifetime. The normalized correlation function $g^{(2)}(0)$ is given by the ratio of the coincidence number of the peak at $\tau = 0$ to the average coincidence number of the side peaks. We considered 20 consecutive periods around the zero delay and used a binning time of 32 ps around each peak. The experiments are performed with different excitation pump powers and laser detuning. The cryostat is mounted on a three-dimensional translation stage with a base structure conceived to reduce the vibrations and the thermal drifts. The helium dewar is kept suspended by the optical table, which significantly reduces the sample's vibrations from the ground. The sample remains stable without drifting from its initial position during minutes.

We display in fig. 7.4 the confined lower polariton's ground state's energy for mesas with a diameter from 500 nm to 2 μ m. The measurements were done under nonresonant excitation and in real space. The pattern number corresponds to a sample position at a given detuning between exciton and two-dimensional cavity photon. Therefore, each mesa size has a different cavity detuning at the same pattern position. We can observe the variation of the polariton ground state energy for each mesa with detuning.

The emission spectrum from the 550 nm mesa (from pattern 3) is shown in fig. 7.5. The ground state confined polariton resonance is located at 1.47631 eV, and its linewidth is 550 μ eV. Due to the submicron-sized mesa, the precise energy and linewidth of the confined polariton are challenging to be measured

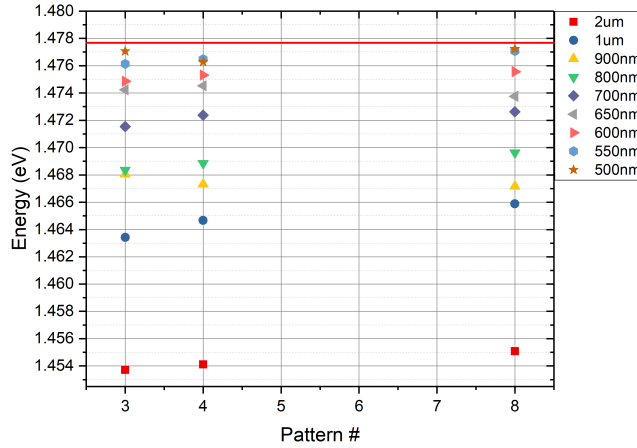


FIGURE 7.4: **Lower polariton's ground state's energy of different mesas.** Confined lower polariton's ground state's energy for mesas with a diameter from 500 nm to 2 μm . The measurement is done under nonresonant excitation in real space. Each pattern has the same structures but at a different detuning. We are working on the 550 nm mesa from pattern 3. The red line shows the exciton energy, which is $E_X = 1.47759 \text{ eV}$.

since the strong nonlinearity induces energy shift and, therefore, a broadening in the measured linewidth.

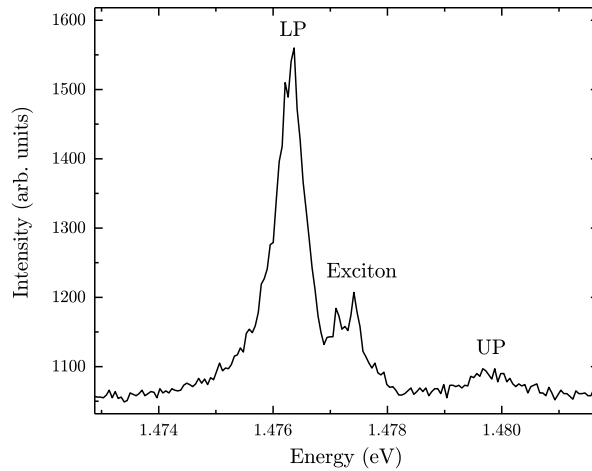


FIGURE 7.5: **The emission spectrum of the 550 nm mesa.** The emission spectrum of the 550 nm mesa and corresponding LP, UP, and exciton energies under nonresonant excitation of 10 μW .

We spectrally probe the lower and upper polariton resonance energy by measuring a broadband pulse's transmission spectrum. We observe the emission

from the confined upper and lower polariton's ground state and the emission from lower polariton first excited state of the mesas in real space (fig. 7.6). The broadening of the lower polariton's ground state with a linewidth of 0.9 meV accompanied by its asymmetric emission illustrates a large energy blueshift due to polariton's interaction.

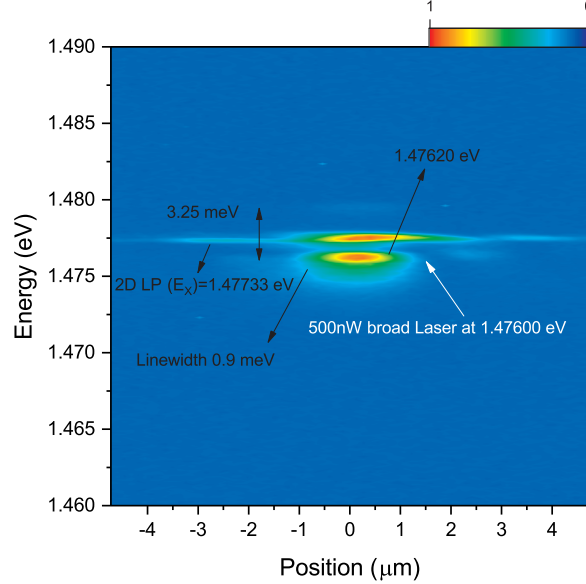


FIGURE 7.6: **The emission of the 550 nm mesa with broadband laser excitation in real space.** The sample is resonantly excited with a 500 nW broadband laser pulse (14 meV) centered at 1.47600 eV. The confined lower polariton's ground state is located at 1.47620 eV with 0.9 meV linewidth, and the upper polariton state 3.25 meV over it. The lower polariton's first excited state is assigned to the bright emission line in the central part. The extension of it outside the mesa corresponds to the emission from the 2D lower polariton at 1.47733 eV.

In fig. 7.7, we demonstrate the lower polariton emission in real space when excited resonantly by a spectrally narrowed laser pulse (170 μeV). In this configuration, we excite only the lower polariton's ground state at 100 nW. We have measured the polariton linewidth of 240 μeV with a blueshift of 85 μeV . Even at this low power, getting the exact linewidth is very challenging due to the inevitable blueshift. To find the lower polariton's ground state, we swept the resonance with different laser wavelengths and specified the actual energy to the one with a maximum blueshift, which is at 1.475925 eV. We send only the emission from the ground state to the correlation measurement within this condition, and we don't have any background emission from 2D.

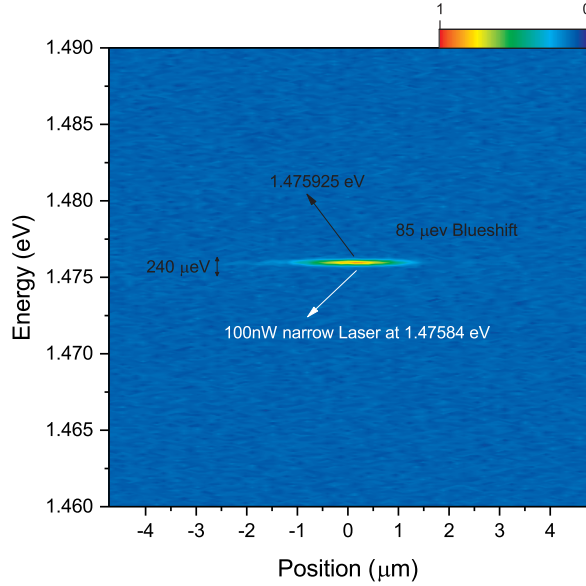


FIGURE 7.7: **The emission of the 550 nm mesa with narrowband laser excitation in real space.** The sample is resonantly excited with a 100 nW narrowband laser pulse (170 μeV) centered at 1.47584 eV (840.04 nm). The confined lower polariton's ground state is at 1.475925 eV with 240 μeV linewidth. The measured energy blueshift of the ground state with respect to the laser is 85 μeV .

7.3 POLARITONS QUANTUM CORRELATION

The polariton correlations are examined through the zero-delay second-order photon correlation function, as specified in eq. (7.2). In order to characterize the polariton emission, the transmitted light is sent to a Hanbury Brown and Twiss (HBT) setup (fig. 7.8) for measuring photon correlations quantified by the behavior of the zero-delay second-order coherence function. In the HBT experiment, the photon stream is split into two and sent to two detectors, then the coincidences between the photons arriving on the two detectors are measured. We can write the eq. (7.2) with a photon number operator as:

$$g^{(2)}(0) = \frac{\langle \hat{c}^\dagger (\hat{c} \hat{c}^\dagger + 1) \hat{c} \rangle}{\langle \hat{c}^\dagger \hat{c} \rangle^2} = \frac{\langle \hat{n}^2 \rangle - \langle \hat{n} \rangle}{\langle \hat{n} \rangle^2} = 1 + \frac{\langle (\Delta \hat{n})^2 \rangle - \langle \hat{n} \rangle}{\langle \hat{n} \rangle^2} \quad (7.3)$$

This representation gives an essential link between $g^{(2)}(0)$ and the photon number distribution. The sign of the term $\langle (\Delta n)^2 \rangle - \langle n \rangle$ depends on the photon number variance's width. It is positive for super-Poissonian statistics and

negative for the sub-Poissonian one. Consequently, this provides a benchmark for classification of light according to photon statistics and the value of $g^{(2)}(0)$.

- $g^{(2)}(0) < 1$ sub-Poissonian statistics (non-classical light)
- $g^{(2)}(0) = 1$ Poissonian statistics (perfectly coherent light)
- $g^{(2)}(0) > 1$ super-Poissonian statistics (chaotic or thermal light)

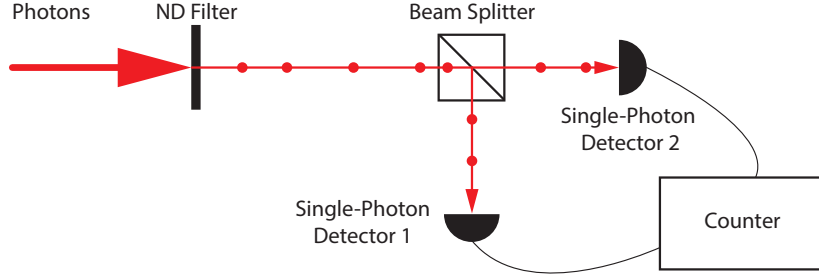


FIGURE 7.8: **Scheme of the Hanbury Brown and Twiss experiment.** The photon stream is split into two arms by a beam splitter; measuring the photons' coincidences arriving on two detectors gives the second-order coherence function.

The second-order correlation function can be measured classically in terms of intensity of the light beam at time t as

$$g^{(2)}(\tau) = \frac{\langle I(t)I(t+\tau) \rangle}{\langle I(t) \rangle \langle I(t+\tau) \rangle} \quad (7.4)$$

Since the number of counts registered on a photon-counting detector is proportional to the intensity, we can rewrite the classical definition of $g^{(2)}(\tau)$ as [147]

$$g^{(2)}(\tau) = \frac{\langle n_1(t)n_2(t+\tau) \rangle}{\langle n_1(t) \rangle \langle n_2(t+\tau) \rangle} \quad (7.5)$$

where $n_i(t)$ is the number of counts registered on detector i at time t .

For $\tau = 0$, we can rewrite the equation by inserting photon annihilation and creation operators for arbitrary photon number state $|n\rangle$

$$g^{(2)}(0) = \frac{\langle n | \hat{c}^\dagger \hat{c}^\dagger \hat{c} \hat{c} | n \rangle}{\langle n | \hat{c}^\dagger \hat{c} | n \rangle^2} = \frac{n^2 - n}{n^2} = 1 - \frac{1}{n} \quad (7.6)$$

A single photon goes to one of the detectors. This suggests that we can obtain the highly non-classical value of $g^{(2)}(0) = 0$ for a single-photon source that emits the photon number states of one.

For the coherent state eq. (7.6) equals to one. This agrees with the fact that the coherent light has the Poissonian statistics.

The thermal light or partially coherent light source are examples of light with the super-Poissonian distribution. The super-Poissonian light is also named bunched, considering photons' simultaneous detections by two detectors of the HBT setup. On contrast, sub-Poissonian light is associated with antibunched photons, indicating that the photons tend to propagate separately.

7.4 EXPERIMENTAL RESULTS

We use 550 nm diameter mesa for the confinement of polaritons to investigate polariton quantum correlations. Considering the recent results from the two groups [144, 145], an anti-bunching of 0.95 with lateral confinement of 2 μm in diameter, we might expect an enhancement of the nonlinearity $U_{pp} \propto (2r^2)^{-1}$ of a factor of 16 by decreasing the lateral confinement diameter to 550 nm by a factor of 4. Using the value of $U_{pp} \approx 13 \mu\text{eV}$ found in [145] we estimate in our sample $U_{pp} \approx 16 \times 13 \mu\text{eV} = 208 \mu\text{eV}$. With this confinement, we could attain high polariton nonlinearity, and we can estimate the figure of merit of the anti-bunching $U_{pp}/\gamma_p \approx 0.87$ when we consider an overestimate value for $\gamma_p = 240 \mu\text{eV}$. Therefore, we could expect the anti-bunching of $g^{(2)}(0) = 0.25$. The requirement to achieve the polariton blockade effect is that the nonlinearity U_{pp} exceeds the linewidth γ_p .

We consider the case of an applied optical field with frequency ω_L close to the frequency of the polariton mode ω_p for the measurements of photon correlation. The degree of antibunching or bunching is given by $g^{(2)}(\tau = 0)$. The dip and peak observation at $\tau = 0$ address the antibunching and bunching, respectively, at the zero-delay of the second-order coherence function. We use a short laser pulse that reduces multiple excitations, which could occur if the pulse duration exceeds the polariton lifetime. The disadvantage is that we need to apply a large enough laser detuning to minimize the spectral overlap of the laser pulse with the shifted resonance line when a second photon attempts to enter the microcavity. This can reduce the measured bunching and anti-bunching due to the lower overlap between the laser pulse and the resonance state [144].

We have performed a thorough series of experiments with different power, integration time, and laser detuning. We plot the normalized second-order correlation function under resonant excitation with 100 nW power at $\lambda = 839.6 \text{ nm}$ and $\lambda = 840.5 \text{ nm}$ in fig. 7.9 and fig. 7.10, respectively. The experiment's integration time is 300 s. We observe the expected behavior, a bunching $g^{(2)}(\tau = 0) = 1.35$ by having $\omega_L - \omega_p = +0.7 \text{ meV}$ (fig. 7.9) and an antibunching $g^{(2)}(\tau = 0) = 0.7$ with $\omega_L - \omega_p = -0.8 \text{ meV}$ (fig. 7.10). Still, the results are not replicable, and in most of the cases, we have a flat correlation function ($g^{(2)}(\tau = 0) = 1$). There are some candidates to address the issue. The laser

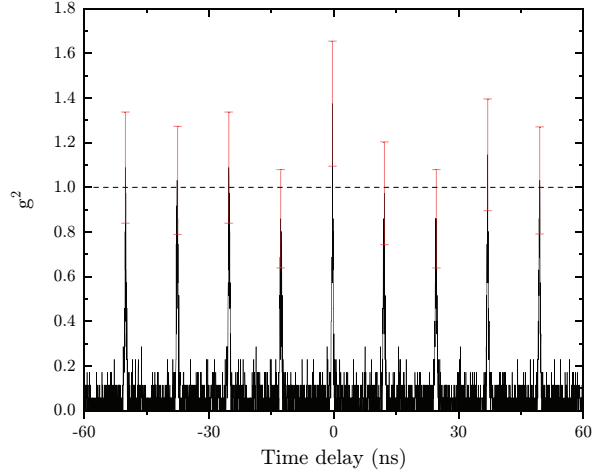


FIGURE 7.9: **Second order correlation function at $\lambda = 839.6 \text{ nm}$.** The bunching $g^{(2)}(0) = 1.35$ behavior with 100 nW excitation. The error bars indicate the square root of the number of coincidence events divided by the mean value of the non-zero events.

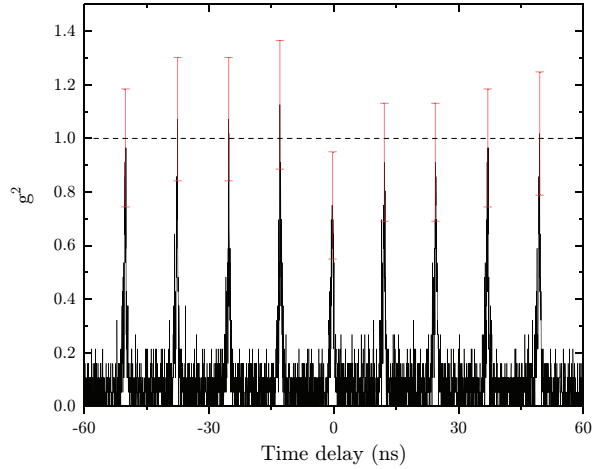


FIGURE 7.10: **Second order correlation function at $\lambda = 840.5 \text{ nm}$.** The antibunching $g^{(2)}(0) = 0.7$ behavior with 100 nW excitation. The error bars indicate the square root of the number of coincidence events divided by the mean value of the non-zero events.

linewidth is not narrow enough, and the amount of energy blueshift is not sufficient to overcome it. Using lower excitation powers, we should increase the experiment's integration time and the laser spot position's stability on the sample.

In conclusion, we've been able to fabricate submicron mesa to confine polaritons tightly and make characterization on different mesa sizes. We performed correlation measurements of 550 nm mesa's emission successfully. We were able, even yet not conclusive, to see some appealing results with our approach. These findings offer encouraging perspectives regarding the demonstration of the polariton blockade. Moreover, the possibility to engineer arrays of sub-micron sized mesas with the integration of strong nonlinearity and efficient intersite tunneling opens the route to the realization of strongly interacting photonic systems [146].

CONCLUSION

*Those who subdued all the wisdom and excellency,
And shone as beacons among their betters,
Out of darksome night could find no way,
Only told a tale, then they fell asleep.*

— Khayyam

The physics of polaritons has witnessed an enormous development since the first observation of polaritons in a semiconductor microcavity. The finding of Bose-Einstein condensation of polaritons in planar microcavity paved the way for studies of spatial coherence and superfluidity with interacting bosons. Nowadays, the polaritonic community focuses on studies of polariton gases confined in patterned potentials. This approach emerged as an attractive route to study the interplay between fundamental nonlinear, spin, and orbital phenomena in topological systems. Two-dimensional lattices are attracting deep interest as a platform for simulating many-body effects.

In the first part of the dissertation, we concentrated on the fundamental study of spinor polariton interaction across the two polaritonic branches, and we demonstrate the polaritonic cross Feshbach resonance. This demonstration will permit the control of the polariton interbranch scattering; it may also initiate studies of many-body physics with polaron quasiparticles and lead to entangled photon pairs generation via the biexciton state.

In the second part, we presented the research on the polaritonic lattices and their fabrication. First, we show the photonic localization due to the breaking of translational symmetry in a triangular lattice and the generation of localized photon lasing for which the lasing mode can be optically controlled. These results open the way for the realization of localized mode lasers of chosen geometry, in which the shape of the generated defect determines the lasing mode. In the second part, we manifest photonic localization by introducing controlled lattice disorder. We believe that the observed phenomenon could be generally achievable in other schemes of steady-state of driven-dissipative systems. Furthermore, we expect that the demonstration of a controlled localization in polaritonic structures could be used in novel optoelectronic devices and quantum information.

Finally, in the last section, we investigated tightly confined polaritons in the engineered microcavity structures with sub-micron size mesas. The analysis of polariton correlations through the second-order correlation measurement aims to approach the polariton blockade. Our results, even yet not conclusive for

polariton blockade, show that we can fabricate with success those structures to confine polaritons strongly. This finding offers promising perspectives concerning the realization of strongly interacting photonic systems.

Although the research's nature is fundamental, the studies presented in this thesis will undoubtedly shed light on exciting features that could be considered for future practical applications.

BIBLIOGRAPHY

1. Tiesinga, E., Mohr, P. J., Newell, D. B. & Taylor, B. N. *The 2018 CODATA Recommended Values of the Fundamental Physical Constants* <http://physics.nist.gov/constants>. (Online; accessed 24.11.2020).
2. Hopfield, J. Theory of the contribution of excitons to the complex dielectric constant of crystals. *Physical Review* **112**, 1555 (1958).
3. Agranovich, V. Dispersion of electromagnetic waves in crystals. *Sov. Phys. JETP* **10**, 307–313 (1960).
4. Weisbuch, C., Nishioka, M., Ishikawa, A. & Arakawa, Y. Observation of the coupled exciton-photon mode splitting in a semiconductor quantum microcavity. *Physical Review Letters* **69**, 3314 (1992).
5. Savona, V., Hradil, Z., Quattropani, A. & Schwendimann, P. Quantum theory of quantum-well polaritons in semiconductor microcavities. *Physical Review B* **49**, 8774 (1994).
6. Baumberg, J., Savvidis, P., Stevenson, R., Tartakovskii, A., Skolnick, M., Whittaker, D. & Roberts, J. Parametric oscillation in a vertical microcavity: A polariton condensate or micro-optical parametric oscillation. *Physical Review B* **62**, R16247 (2000).
7. Savvidis, P., Baumberg, J., Stevenson, R., Skolnick, M., Whittaker, D. & Roberts, J. Angle-resonant stimulated polariton amplifier. *Physical Review Letters* **84**, 1547 (2000).
8. Ciuti, C., Schwendimann, P., Deveaud, B. & Quattropani, A. Theory of the angle-resonant polariton amplifier. *Physical Review B* **62**, R4825 (2000).
9. Baas, A., Karr, J. P., Eleuch, H. & Giacobino, E. Optical bistability in semiconductor microcavities. *Physical Review A* **69**, 023809 (2004).
10. Amo, A., Liew, T., Adrados, C., Houdré, R., Giacobino, E., Kavokin, A. & Bramati, A. Exciton–polariton spin switches. *Nature Photonics* **4**, 361–366 (2010).
11. Kasprzak, J., Richard, M., Kundermann, S., Baas, A., Jeambrun, P., Keeling, J., Marchetti, F., Szymańska, M., André, R., Staehli, J., *et al.* Bose–Einstein condensation of exciton polaritons. *Nature* **443**, 409–414 (2006).
12. Wertz, E., Ferrier, L., Solnyshkov, D. D., Senellart, P., Bajoni, D., Miard, A., Lemaître, A., Malpuech, G. & Bloch, J. Spontaneous formation of a polariton condensate in a planar GaAs microcavity. *Applied Physics Letters* **95**, 051108 (2009).

13. Christopoulos, S., Von Högersthal, G. B. H., Grundy, A., Lagoudakis, P., Kavokin, A., Baumberg, J., Christmann, G., Butté, R., Feltin, E., Carlin, J.-F., *et al.* Room-temperature polariton lasing in semiconductor microcavities. *Physical Review Letters* **98**, 126405 (2007).
14. Bajoni, D., Senellart, P., Wertz, E., Sagnes, I., Miard, A., Lemaître, A. & Bloch, J. Polariton laser using single micropillar GaAs- GaAlAs semiconductor cavities. *Physical Review Letters* **100**, 047401 (2008).
15. Wertz, E., Ferrier, L., Solnyshkov, D., Johne, R., Sanvitto, D., Lemaître, A., Sagnes, I., Grousson, R., Kavokin, A. V., Senellart, P., *et al.* Spontaneous formation and optical manipulation of extended polariton condensates. *Nature physics* **6**, 860–864 (2010).
16. Kavokin, A., Baumberg, J. J., Malpuech, G. & Laussy, F. P. *Microcavities* (Oxford University Press, 2017).
17. Saleh, B. E. & Teich, M. C. *Fundamentals of photonics* (John Wiley & sons, 2019).
18. Deng, H., Haug, H. & Yamamoto, Y. Exciton-polariton Bose-Einstein condensation. *Reviews of Modern Physics* **82**, 1489 (2010).
19. Levinshtein, M. E. & Rumyantsev, S. L. *Handbook Series on Semiconductor Parameters "GALLIUM ARSENIDE (GaAs)"* pp. 77–103 (World Scientific, 1996).
20. Savona, V., Piermarocchi, C., Quattropani, A., Schwendimann, P. & Tassone, F. Optical properties of microcavity polaritons. *Phase Transitions* **68**, 169–279 (1999).
21. Haug, H. & Koch, S. W. *Quantum theory of the optical and electronic properties of semiconductors: fifth edition* (World Scientific Publishing Company, 2009).
22. Zhang, B., Kano, S. S., Shiraki, Y. & Ito, R. Reflectance study of the oscillator strength of excitons in semiconductor quantum wells. *Physical Review B* **50**, 7499 (1994).
23. Savona, V., Andreani, L., Schwendimann, P. & Quattropani, A. Quantum well excitons in semiconductor microcavities: Unified treatment of weak and strong coupling regimes. *Solid State Communications* **93**, 733–739 (1995).
24. Benisty, H., Weisbuch, C., Gérard, J.-M., Houdré, R. & Rarity, J. *Confined Photon Systems: Fundamentals and Applications: Lectures from the Summerschool Held in Cargèse, Corsica, 3-15 August 1998* p. 210 (Springer, 1999).
25. Khitrova, G., Gibbs, H., Kira, M., Koch, S. W. & Scherer, A. Vacuum Rabi splitting in semiconductors. *Nature Physics* **2**, 81–90 (2006).

26. Ciuti, C., Savona, V., Piermarocchi, C., Quattropani, A. & Schwendimann, P. Role of the exchange of carriers in elastic exciton-exciton scattering in quantum wells. *Physical Review B* **58**, 7926 (1998).
27. Wouters, M. Resonant polariton-polariton scattering in semiconductor microcavities. *Physical Review B* **76**, 045319 (2007).
28. Rochat, G., Ciuti, C., Savona, V., Piermarocchi, C., Quattropani, A. & Schwendimann, P. Excitonic Bloch equations for a two-dimensional system of interacting excitons. *Physical Review B* **61**, 13856 (2000).
29. Combescot, M., Dupertuis, M. & Betbeder-Matibet, O. Polariton-polariton scattering: Exact results through a novel approach. *EPL (Europhysics Letters)* **79**, 17001 (2007).
30. Takemura, N., Anderson, M. D., Trebaol, S., Biswas, S., Oberli, D., Portella-Oberli, M. T. & Deveaud, B. Dephasing effects on coherent exciton-polaritons and the breakdown of the strong coupling regime. *Physical Review B* **92**, 235305 (2015).
31. Takemura, N., Trebaol, S., Wouters, M., Portella-Oberli, M. T. & Deveaud, B. Polaritonic Feshbach resonance. *Nature Physics* **10**, 500–504 (2014).
32. Takemura, N., Anderson, M., Navadeh-Toupchi, M., Oberli, D., Portella-Oberli, M. & Deveaud, B. Spin anisotropic interactions of lower polaritons in the vicinity of polaritonic Feshbach resonance. *Physical Review B* **95**, 205303 (2017).
33. Parker, E. H. *The technology and physics of molecular beam epitaxy* (Plenum Press New York, 1985).
34. Yu, H., Roberts, C. & Murray, R. Influence of indium segregation on the emission from InGaAs/GaAs quantum wells. *Applied Physics Letters* **66**, 2253–2255 (1995).
35. Deveaud, B. *The physics of semiconductor microcavities* (John Wiley & Sons, 2007).
36. Negoita, V., Snoke, D. & Eberl, K. Stretching quantum wells: A method for trapping free carriers in GaAs heterostructures. *Applied Physics Letters* **75**, 2059–2061 (1999).
37. Gerard, J., Barrier, D., Marzin, J., Kuszelewicz, R., Manin, L., Costard, E., Thierry-Mieg, V. & Rivera, T. Quantum boxes as active probes for photonic microstructures: The pillar microcavity case. *Applied Physics Letters* **69**, 449–451 (1996).
38. El Daïf, O., Baas, A., Guillet, T., Brantut, J.-P., Kaitouni, R. I., Staehli, J.-L., Morier-Genoud, F. & Deveaud, B. Polariton quantum boxes in semiconductor microcavities. *Applied Physics Letters* **88**, 061105 (2006).

39. Kaitouni, R. I., El Daïf, O., Baas, A., Richard, M., Paraiso, T., Lugan, P., Guillet, T., Morier-Genoud, F., Ganière, J., Staehli, J., *et al.* Engineering the spatial confinement of exciton polaritons in semiconductors. *Physical Review B* **74**, 155311 (2006).
40. Verger, A., Ciuti, C. & Carusotto, I. Polariton quantum blockade in a photonic dot. *Physical Review B* **73**, 193306 (2006).
41. Imamoğlu, A., Schmidt, H., Woods, G. & Deutsch, M. Strongly interacting photons in a nonlinear cavity. *Physical Review Letters* **79**, 1467 (1997).
42. Paraïso, T., Wouters, M., Léger, Y., Morier-Genoud, F. & Deveaud-Plédran, B. Multistability of a coherent spin ensemble in a semiconductor microcavity. *Nature Materials* **9**, 655–660 (2010).
43. Cerna, R., Léger, Y., Paraïso, T. K., Wouters, M., Morier-Genoud, F., Portella-Oberli, M. T. & Deveaud, B. Ultrafast tristable spin memory of a coherent polariton gas. *Nature Communications* **4**, 1–8 (2013).
44. Abbaspour, H., Trebaol, S., Morier-Genoud, F., Portella-Oberli, M. & Deveaud, B. Spinor stochastic resonance. *Physical Review B* **91**, 155307 (2015).
45. Wouters, M., Paraïso, T., Léger, Y., Cerna, R., Morier-Genoud, F., Portella-Oberli, M. T. & Deveaud-Plédran, B. Influence of a nonradiative reservoir on polariton spin multistability. *Physical Review B* **87**, 045303 (2013).
46. Takemura, N., Trebaol, S., Anderson, M., Kohnle, V., Léger, Y., Oberli, D., Portella-Oberli, M. T. & Deveaud, B. Two-dimensional Fourier transform spectroscopy of exciton-polaritons and their interactions. *Physical Review B* **92**, 125415 (2015).
47. Navadeh-Toupchi, M., Takemura, N., Anderson, M., Oberli, D. & Portella-Oberli, M. Polaritonic cross Feshbach resonance. *Physical Review Letters* **122**, 047402 (2019).
48. Oka, H. & Ishihara, H. Highly efficient generation of entangled photons by controlling cavity bipolariton states. *Physical Review Letters* **100**, 170505 (2008).
49. Oka, H., Oohata, G. & Ishihara, H. Efficient generation of energy-tunable entangled photons in a semiconductor microcavity. *Applied Physics Letters* **94**, 111113 (2009).
50. Levinsen, J., Marchetti, F. M., Keeling, J. & Parish, M. M. Spectroscopic signatures of quantum many-body correlations in polariton microcavities. *Physical Review Letters* **123**, 266401 (2019).
51. Sidler, M., Back, P., Cotlet, O., Srivastava, A., Fink, T., Kroner, M., Demler, E. & Imamoğlu, A. Fermi polaron-polaritons in charge-tunable atomically thin semiconductors. *Nature Physics* **13**, 255–261 (2017).

52. Stanley, R., Houdre, R., Oesterle, U., Gailhanou, M. & Ilegems, M. Ultrahigh finesse microcavity with distributed Bragg reflectors. *Applied Physics Letters* **65**, 1883–1885 (1994).
53. Inouye, S., Andrews, M., Stenger, J., Miesner, H.-J., Stamper-Kurn, D. & Ketterle, W. Observation of Feshbach resonances in a Bose–Einstein condensate. *Nature* **392**, 151–154 (1998).
54. Donley, E. A., Claussen, N. R., Cornish, S. L., Roberts, J. L., Cornell, E. A. & Wieman, C. E. Dynamics of collapsing and exploding Bose–Einstein condensates. *Nature* **412**, 295–299 (2001).
55. Greiner, M., Regal, C. A. & Jin, D. S. Emergence of a molecular Bose–Einstein condensate from a Fermi gas. *Nature* **426**, 537–540 (2003).
56. Bloch, I., Dalibard, J. & Zwirger, W. Many-body physics with ultracold gases. *Reviews of Modern Physics* **80**, 885 (2008).
57. Lopes, R., Eigen, C., Navon, N., Clément, D., Smith, R. P. & Hadzibabic, Z. Quantum depletion of a homogeneous Bose–Einstein condensate. *Physical Review Letters* **119**, 190404 (2017).
58. Birkedal, D., Singh, J., Lyssenko, V., Erland, J. & Hvam, J. M. Binding of quasi-two-dimensional biexcitons. *Physical Review Letters* **76**, 672 (1996).
59. Szczytko, J., Kappei, L., Berney, J., Morier-Genoud, F., Portella-Oberli, M. & Deveaud, B. Determination of the exciton formation in quantum wells from time-resolved interband luminescence. *Physical Review Letters* **93**, 137401 (2004).
60. Takemura, N., Anderson, M., Biswas, S., Navadeh-Toupchi, M., Oberli, D., Portella-Oberli, M. & Deveaud, B. Coherent and incoherent aspects of polariton dynamics in semiconductor microcavities. *Physical Review B* **94**, 195301 (2016).
61. Vladimirova, M., Cronenberger, S., Scalbert, D., Nawrocki, M., Kavokin, A., Miard, A., Lemaître, A. & Bloch, J. Polarization controlled nonlinear transmission of light through semiconductor microcavities. *Physical Review B* **79**, 115325 (2009).
62. Kwong, N.-H., Takayama, R., Rumyantsev, I., Kuwata-Gonokami, M. & Binder, R. Third-order exciton-correlation and nonlinear cavity-polariton effects in semiconductor microcavities. *Physical Review B* **64**, 045316 (2001).
63. Bastarrachea-Magnani, M., Camacho-Guardian, A., Wouters, M. & Bruun, G. Strong interactions and biexcitons in a polariton mixture. *Physical Review B* **100**, 195301 (2019).
64. Landau, L. & Pekar, S. Effective mass of a polaron. *Zh. Eksp. Teor. Fiz* **18**, 419–423 (1948).

65. Jørgensen, N. B., Wacker, L., Skalmstang, K. T., Parish, M. M., Levinsen, J., Christensen, R. S., Bruun, G. M. & Arlt, J. J. Observation of attractive and repulsive polarons in a Bose-Einstein condensate. *Physical Review Letters* **117**, 055302 (2016).
66. Hu, M.-G., Van de Graaff, M. J., Kedar, D., Corson, J. P., Cornell, E. A. & Jin, D. S. Bose polarons in the strongly interacting regime. *Physical Review Letters* **117**, 055301 (2016).
67. Savasta, S., Martino, G. & Girlanda, R. Entangled photon pairs from the optical decay of biexcitons. *Solid State Communications* **111**, 495–500 (1999).
68. Ciuti, C. Branch-entangled polariton pairs in planar microcavities and photonic wires. *Physical Review B* **69**, 245304 (2004).
69. Bouwmeester, D. & Zeilinger, A. *The Physics of Quantum Information: Basic Concepts* (Springer, 2000).
70. Gisin, N., Ribordy, G., Tittel, W. & Zbinden, H. Quantum cryptography. *Reviews of Modern Physics* **74**, 145 (2002).
71. Ivanov, A., Borri, P., Langbein, W. & Woggon, U. Radiative corrections to the excitonic molecule state in GaAs microcavities. *Physical Review B* **69**, 075312 (2004).
72. Tassone, F., Piermarocchi, C., Savona, V., Quattropani, A. & Schwendimann, P. Bottleneck effects in the relaxation and photoluminescence of microcavity polaritons. *Physical Review B* **56**, 7554 (1997).
73. Navadeh-Toupchi, M., Jabeen, F., Oberli, D. & Portella-Oberli, M. Localized Photon Lasing in a Polaritonic Lattice Landscape. *Physical Review Applied* **14**, 024055 (2020).
74. Sturges, T. J., Anderson, M. D., Buraczewski, A., Navadeh-Toupchi, M., Adiyatullin, A. F., Jabeen, F., Oberli, D. Y., Portella-Oberli, M. T. & Stobińska, M. Anderson localisation in steady states of microcavity polaritons. *Scientific Reports* **9**, 1–6 (2019).
75. Balili, R., Hartwell, V., Snoke, D., Pfeiffer, L. & West, K. Bose-Einstein condensation of microcavity polaritons in a trap. *Science* **316**, 1007–1010 (2007).
76. Cerda-Méndez, E., Sarkar, D., Krizhanovskii, D., Gavrilov, S., Biermann, K., Skolnick, M. & Santos, P. Exciton-polariton gap solitons in two-dimensional lattices. *Physical Review Letters* **111**, 146401 (2013).
77. Lai, C., Kim, N., Utsunomiya, S., Roumpos, G., Deng, H., Fraser, M., Byrnes, T., Recher, P., Kumada, N., Fujisawa, T., *et al.* Coherent zero-state and π -state in an exciton-polariton condensate array. *Nature* **450**, 529–532 (2007).

78. Bloch, J., Boeuf, F., Gérard, J., Legrand, B., Marzin, J., Planel, R., Thierry-Mieg, V. & Costard, E. Strong and weak coupling regime in pillar semiconductor microcavities. *Physica E: Low-dimensional Systems and Nanostructures* **2**, 915–919 (1998).
79. Wallace, P. R. The band theory of graphite. *Physical Review* **71**, 622 (1947).
80. McKinnon, B. & Choy, T. Significance of nonorthogonality in tight-binding models. *Physical Review B* **52**, 14531 (1995).
81. Schmitt-Rink, S., Chemla, D. & Miller, D. Theory of transient excitonic optical nonlinearities in semiconductor quantum-well structures. *Physical Review B* **32**, 6601 (1985).
82. J. D. Joannopoulos, R. B. M. & Winn, J. N. *Photonic crystals: Molding the flow of light* 1995.
83. Christodoulides, D. N., Lederer, F. & Silberberg, Y. Discretizing light behaviour in linear and nonlinear waveguide lattices. *Nature* **424**, 817–823 (2003).
84. Fleischer, J. W., Segev, M., Efremidis, N. K. & Christodoulides, D. N. Observation of two-dimensional discrete solitons in optically induced nonlinear photonic lattices. *Nature* **422**, 147–150 (2003).
85. Lederer, F., Stegeman, G. I., Christodoulides, D. N., Assanto, G., Segev, M. & Silberberg, Y. Discrete solitons in optics. *Physics Reports* **463**, 1–126 (2008).
86. Chen, Z., Segev, M. & Christodoulides, D. N. Optical spatial solitons: historical overview and recent advances. *Reports on Progress in Physics* **75**, 086401 (2012).
87. Mingaleev, S. F. & Kivshar, Y. S. Self-trapping and stable localized modes in nonlinear photonic crystals. *Physical Review Letters* **86**, 5474 (2001).
88. Christodoulides, D. & Joseph, R. Discrete self-focusing in nonlinear arrays of coupled waveguides. *Optics letters* **13**, 794–796 (1988).
89. Dowling, J. P., Scalora, M., Bloemer, M. J. & Bowden, C. M. The photonic band edge laser: A new approach to gain enhancement. *Journal of Applied Physics* **75**, 1896–1899 (1994).
90. Inoue, K., Sasada, M., Kawamata, J., Sakoda, K. & Haus, J. W. A two-dimensional photonic crystal laser. *Japanese Journal of Applied Physics* **38**, L157 (1999).
91. Meier, M., Mekis, A., Dodabalapur, A., Timko, A., Slusher, R., Joannopoulos, J. & Nalamasu, O. Laser action from two-dimensional distributed feedback in photonic crystals. *Applied Physics Letters* **74**, 7–9 (1999).
92. Boutami, S., Bakir, B. B., Regreny, P., Leclercq, J. & Viktorovitch, P. Compact 1.55 μm room-temperature optically pumped photonic crystal mirror-VCSEL in *The European Conference on Lasers and Electro-Optics* (2007), CB4_3.

93. Ryu, H.-Y., Kwon, S.-H., Lee, Y.-J., Lee, Y.-H. & Kim, J.-S. Very-low-threshold photonic band-edge lasers from free-standing triangular photonic crystal slabs. *Applied Physics Letters* **80**, 3476–3478 (2002).
94. Painter, O., Lee, R., Scherer, A., Yariv, A., O’Brien, J., Dapkus, P. & Kim, I. Two-dimensional photonic band-gap defect mode laser. *Science* **284**, 1819–1821 (1999).
95. Park, H.-G., Hwang, J.-K., Huh, J., Ryu, H.-Y., Lee, Y.-H. & Kim, J.-S. Nondegenerate monopole-mode two-dimensional photonic band gap laser. *Applied Physics Letters* **79**, 3032–3034 (2001).
96. Martínez, L. J., Alén, B., Prieto, I., Fuster, D., González, L., González, Y., Dotor, M. L. & Postigo, P. A. Room temperature continuous wave operation in a photonic crystal microcavity laser with a single layer of InAs/InP self-assembled quantum wires. *Optics Express* **17**, 14993–15000 (2009).
97. Amo, A. & Bloch, J. Exciton-polaritons in lattices: A non-linear photonic simulator. *Comptes Rendus Physique* **17**, 934–945 (2016).
98. Jacqmin, T., Carusotto, I., Sagnes, I., Abbarchi, M., Solnyshkov, D., Malpuech, G., Galopin, E., Lemaître, A., Bloch, J. & Amo, A. Direct observation of Dirac cones and a flatband in a honeycomb lattice for polaritons. *Physical Review Letters* **112**, 116402 (2014).
99. Tanese, D., Flayac, H., Solnyshkov, D., Amo, A., Lemaître, A., Galopin, E., Braive, R., Senellart, P., Sagnes, I., Malpuech, G., *et al.* Polariton condensation in solitonic gap states in a one-dimensional periodic potential. *Nature Communications* **4**, 1–9 (2013).
100. Milicevic, M., Bleu, O., Solnyshkov, D. D., Sagnes, I., Lemaître, A., Gratiot, L., Harouri, A., Bloch, J., Malpuech, G. & Amo, A. Lasing in optically induced gap states in photonic graphene. *SciPost Phys* **5**, 64 (2018).
101. Winkler, K., Fischer, J., Schade, A., Amthor, M., Dall, R., Geßler, J., Emmerling, M., Ostrovskaya, E. A., Kamp, M., Schneider, C., *et al.* A polariton condensate in a photonic crystal potential landscape. *New Journal of Physics* **17**, 023001 (2015).
102. Winkler, K., Egorov, O. A., Savenko, I., Ma, X., Estrecho, E., Gao, T., Müller, S., Kamp, M., Liew, T. C. H., Ostrovskaya, E., *et al.* Collective state transitions of exciton-polaritons loaded into a periodic potential. *Physical Review B* **93**, 121303 (2016).
103. Pier, H., Kapon, E. & Moser, M. Strain effects and phase transitions in photonic resonator crystals. *Nature* **407**, 880–883 (2000).
104. Lundeborg, L., Boiko, D. & Kapon, E. Coupled islands of photonic crystal heterostructures implemented with vertical-cavity surface-emitting lasers. *Applied Physics Letters* **87**, 241120 (2005).

105. Mutter, L., Iakovlev, V., Caliman, A., Mereuta, A., Sirbu, A. & Kapon, E. 1.3 μm -wavelength phase-locked VCSEL arrays incorporating patterned tunnel junction. *Optics Express* **17**, 8558–8566 (2009).
106. Song, D.-S., Kim, S.-H., Park, H.-G., Kim, C.-K. & Lee, Y.-H. Single-fundamental-mode photonic-crystal vertical-cavity surface-emitting lasers. *Applied Physics Letters* **80**, 3901–3903 (2002).
107. Raftery Jr, J. J., Danner, A. J., Lee, J. C. & Choquette, K. D. Coherent coupling of two-dimensional arrays of defect cavities in photonic crystal vertical cavity surface-emitting lasers. *Applied Physics Letters* **86**, 201104 (2005).
108. Griffin, B. G., Arbabi, A., Tan, M. P., Kasten, A. M., Choquette, K. D. & Goddard, L. L. Demonstration of enhanced side-mode suppression in metal-filled photonic crystal vertical cavity lasers. *Optics letters* **38**, 1936–1938 (2013).
109. Nyakas, P. Honeycomb photonic crystal vertical-cavity surface-emitting lasers: coupled cavities enhancing the single-mode range. *JOSA B* **30**, 3284–3290 (2013).
110. Kappei, L., Szczytko, J., Morier-Genoud, F. & Deveaud, B. Direct observation of the Mott transition in an optically excited semiconductor quantum well. *Physical Review Letters* **94**, 147403 (2005).
111. Aitchison, J. S., Hutchings, D., Kang, J., Stegeman, G. & Villeneuve, A. The nonlinear optical properties of AlGaAs at the half band gap. *IEEE Journal of Quantum Electronics* **33**, 341–348 (1997).
112. Anderson, P. W. Absence of diffusion in certain random lattices. *Physical Review* **109**, 1492 (1958).
113. Lee, P. A. & Ramakrishnan, T. Disordered electronic systems. *Reviews of Modern Physics* **57**, 287 (1985).
114. Sheng, P. *Introduction to Wave Scattering, Localization and Mesoscopic Phenomena* (Springer-Verlag Berlin Heidelberg, 2006).
115. Wiersma, D. S., Bartolini, P., Lagendijk, A. & Righini, R. Localization of light in a disordered medium. *Nature* **390**, 671–673 (1997).
116. Anderson, P. W. The question of classical localization A theory of white paint? *Philosophical Magazine B* **52**, 505–509 (1985).
117. Kaveh, M. Localization of photons in disordered systems. *Philosophical Magazine B* **56**, 693–703 (1987).
118. Schwartz, T., Bartal, G., Fishman, S. & Segev, M. Transport and Anderson localization in disordered two-dimensional photonic lattices. *Nature* **446**, 52–55 (2007).
119. Wouters, M. & Carusotto, I. Excitations in a nonequilibrium Bose-Einstein condensate of exciton polaritons. *Physical Review Letters* **99**, 140402 (2007).

120. Zambon, N. C., St-Jean, P., Milićević, M., Lemaître, A., Harouri, A., Le Gratiet, L., Bleu, O., Solnyshkov, D., Malpuech, G., Sagnes, I., *et al.* Optically controlling the emission chirality of microlasers. *Nature Photonics* **13**, 283–288 (2019).
121. Noda, S., Chutinan, A. & Imada, M. Trapping and emission of photons by a single defect in a photonic bandgap structure. *Nature* **407**, 608–610 (2000).
122. Akahane, Y., Asano, T., Song, B.-S. & Noda, S. Investigation of high-Q channel drop filters using donor-type defects in two-dimensional photonic crystal slabs. *Applied Physics Letters* **83**, 1512–1514 (2003).
123. Notomi, M. & Taniyama, H. On-demand ultrahigh-Q cavity formation and photon pinning via dynamic waveguide tuning. *Optics Express* **16**, 18657–18666 (2008).
124. Rüter, C. E., Makris, K. G., El-Ganainy, R., Christodoulides, D. N., Segev, M. & Kip, D. Observation of parity–time symmetry in optics. *Nature physics* **6**, 192–195 (2010).
125. Konotop, V. V., Yang, J. & Zezyulin, D. A. Nonlinear waves in PT-symmetric systems. *Reviews of Modern Physics* **88**, 035002 (2016).
126. Rahimzadeh Kalaleh Rodriguez, S., Amo, A., Carusotto, I., Sagnes, I., Le Gratiet, L., Galopin, E., Lemaître, A. & Bloch, J. Nonlinear polariton localization in strongly coupled driven-dissipative microcavities. *ACS Photonics* **5**, 95–99 (2018).
127. Liew, T., Kavokin, A. & Shelykh, I. Optical circuits based on polariton neurons in semiconductor microcavities. *Physical Review Letters* **101**, 016402 (2008).
128. Ouellet-Plamondon, C., Sallen, G., Morier-Genoud, F., Oberli, D., Portella-Oberli, M. & Deveaud, B. Spatial multistability induced by cross interactions of confined polariton modes. *Physical Review B* **93**, 085313 (2016).
129. Werner, M. J. & Imamoglu, A. Photon-photon interactions in cavity electromagnetically induced transparency. *Physical Review A* **61**, 011801 (1999).
130. Rebic, S., Tan, S., Parkins, A. & Walls, D. Large Kerr nonlinearity with a single atom. *Journal of Optics B: Quantum and Semiclassical Optics* **1**, 490 (1999).
131. Rebić, S., Parkins, A. & Tan, S. Polariton analysis of a four-level atom strongly coupled to a cavity mode. *Physical Review A* **65**, 043806 (2002).
132. Rebić, S., Parkins, A. & Tan, S. Photon statistics of a single-atom intracavity system involving electromagnetically induced transparency. *Physical Review A* **65**, 063804 (2002).

133. Tian, L. & Carmichael, H. Quantum trajectory simulations of two-state behavior in an optical cavity containing one atom. *Physical Review A* **46**, R6801 (1992).
134. Brecha, R., Rice, P. & Xiao, M. N two-level atoms in a driven optical cavity: Quantum dynamics of forward photon scattering for weak incident fields. *Physical Review A* **59**, 2392 (1999).
135. Birnbaum, K. M., Boca, A., Miller, R., Boozer, A. D., Northup, T. E. & Kimble, H. J. Photon blockade in an optical cavity with one trapped atom. *Nature* **436**, 87–90 (2005).
136. Faraon, A., Fushman, I., Englund, D., Stoltz, N., Petroff, P. & Vučković, J. Coherent generation of non-classical light on a chip via photon-induced tunnelling and blockade. *Nature Physics* **4**, 859–863 (2008).
137. Volz, T., Reinhard, A., Winger, M., Badolato, A., Hennessy, K. J., Hu, E. L. & Imamoglu, A. Ultrafast all-optical switching by single photons. *Nature Photonics* **6**, 605–609 (2012).
138. Reinhard, A., Volz, T., Winger, M., Badolato, A., Hennessy, K. J., Hu, E. L. & Imamoglu, A. Strongly correlated photons on a chip. *Nature Photonics* **6**, 93–96 (2012).
139. Lang, C., Bozyigit, D., Eichler, C., Steffen, L., Fink, J., Abdumalikov Jr, A., Baur, M., Filipp, S., Da Silva, M., Blais, A., *et al.* Observation of resonant photon blockade at microwave frequencies using correlation function measurements. *Physical Review Letters* **106**, 243601 (2011).
140. Carusotto, I. Nonlinear atomic Fabry-Perot interferometer: From the mean-field theory to the atom blockade effect. *Physical Review A* **63**, 023610 (2001).
141. Liew, T. & Savona, V. Single photons from coupled quantum modes. *Physical Review Letters* **104**, 183601 (2010).
142. Bamba, M., Imamoglu, A., Carusotto, I. & Ciuti, C. Origin of strong photon antibunching in weakly nonlinear photonic molecules. *Physical Review A* **83**, 021802 (2011).
143. Carusotto, I., Volz, T. & Imamoglu, A. Feshbach blockade: Single-photon nonlinear optics using resonantly enhanced cavity polariton scattering from biexciton states. *EPL (Europhysics Letters)* **90**, 37001 (2010).
144. Muñoz-Matutano, G., Wood, A., Johnsson, M., Vidal, X., Baragiola, B. Q., Reinhard, A., Lemaître, A., Bloch, J., Amo, A., Nogues, G., *et al.* Emergence of quantum correlations from interacting fibre-cavity polaritons. *Nature Materials* **18**, 213–218 (2019).
145. Delteil, A., Fink, T., Schade, A., Höfling, S., Schneider, C. & Imamoglu, A. Towards polariton blockade of confined exciton-polaritons. *Nature Materials* **18**, 219–222 (2019).

- 146. Carusotto, I. & Ciuti, C. Quantum fluids of light. *Reviews of Modern Physics* **85**, 299 (2013).
- 147. Fox, M. *Quantum Optics: An Introduction* (OUP Oxford, 2006).

CURRICULUM VITAE

PERSONAL DATA

Name	Morteza NAVADEH TOUPCHI
Date of Birth	December 1, 1990
email	morteza@toupchi.com
LinkedIn	linkedin.com/in/mortezatoupchi

EDUCATION

2015 – 2020	Swiss Federal Institute of Technology (EPFL) Lausanne, Switzerland Ph.D. in Photonics
2013 – 2015	Sharif University of Technology Tehran, Iran M.Sc. in Physics
2009 – 2013	Sharif University of Technology Tehran, Iran B.Sc. in Physics

EXPERIENCE

Ph.D. Student/Research Engineer - LOEQ

2015 – 2020	<ul style="list-style-type: none">–Layout design and manufacture of state of the art confined cavity structures.–Developing a repeatable process for fabrication of below $1\mu\text{m}$ mesas on GaAs.–Modeling and simulation of polariton's interaction in cavity QED.–Characterization and optical spectroscopy.–Cryogenic CW and pulsed laser experiments of optoelectronic devices.–Second-order coherence and correlation measurement of single photons.
-------------	---

Master Student/Researcher

2013 – 2015	Theoretical study of Parity-Time symmetry and its application in multilevel atomic systems to mitigate loss in optical systems.
-------------	---

SKILLS

Laboratory	Semiconductor and Silicon Photonics, Cleanroom facilities, E-beam and photolithography, SEM and Optical microscopy, Cryogenics.
Software	Origin, Layout Editor, IPKISS, LabVIEW, Matlab, Mathematica, Illustrator, AutoCAD.
Programming	Python, C++, Data Analysis, Data visualisation.

HONORS

2015	Ranked 1st among Physics graduate students.
2013	Directly admitted to the Master program as an excellent student award.
2013	Exceptional talent scholarship of Iran's national elites foundation.

TEACHING EXPERIENCE

2015 – 2020	Optics III, Physics lab II and Physics lab III.
-------------	---

LANGUAGES

Persian (Native)
 English (Business Fluent - C1)
 French (B1)
 German (A2)

PUBLICATIONS

Articles in peer-reviewed journals:

1. Navadeh-Toupchi, M., Jabeen, F., Oberli, D. & Portella-Oberli, M. Localized Photon Lasing in a Polaritonic Lattice Landscape. *Physical Review Applied* **14**, 024055 (2020).
2. Sturges, T. J., Anderson, M. D., Buraczewski, A., Navadeh-Toupchi, M., Adiyatullin, A. F., Jabeen, F., Oberli, D. Y., Portella-Oberli, M. T. & Stobińska, M. Anderson localisation in steady states of microcavity polaritons. *Scientific Reports* **9**, 1–6 (2019).
3. Navadeh-Toupchi, M., Takemura, N., Anderson, M., Oberli, D. & Portella-Oberli, M. Polaritonic cross Feshbach resonance. *Physical Review Letters* **122**, 047402 (2019).
4. Takemura, N., Anderson, M., Navadeh-Toupchi, M., Oberli, D., Portella-Oberli, M. & Deveaud, B. Spin anisotropic interactions of lower polaritons in the vicinity of polaritonic Feshbach resonance. *Physical Review B* **95**, 205303 (2017).
5. Takemura, N., Anderson, M., Biswas, S., Navadeh-Toupchi, M., Oberli, D., Portella-Oberli, M. & Deveaud, B. Coherent and incoherent aspects of polariton dynamics in semiconductor microcavities. *Physical Review B* **94**, 195301 (2016).
6. Sadighi-Bonabi, R., Naseri, T. & Navadeh-Toupchi, M. Electromagnetically induced grating in the microwave-driven four-level atomic systems. *Applied Optics* **54**, 368–377 (2015).

Conference contributions:

7. Anderson, M., Takemura, N., Navadeh-Toupchi, M., Oberli, D., Portella-Oberli, M. & Deveaud, B. *Optical control of population dynamics in 8th International conference on spontaneous coherence in excitonic systems (ICSCE8)* Apr. 25–29, 2016 (Edinburgh, UK).
8. Navadeh-Toupchi, M., Anderson, M., Takemura, N., Oberli, D., Portella-Oberli, M. & Deveaud, B. *Branch dependant polariton dephasing mechanisms in 8th International conference on spontaneous coherence in excitonic systems (ICSCE8)* Apr. 25–29, 2016 (Edinburgh, UK).
9. Navadeh-Toupchi, M., Anderson, M., Takemura, N., Oberli, D., Deveaud, B. & Portella-Oberli, M. *Polaritonic cross Feshbach resonance in 18th International conference on physics of light-matter coupling in nanostructures (PLMCN18)* July 9–14, 2017 (Würzburg, Germany).

10. Navadeh-Toupchi, M., Anderson, M., Takemura, N., Oberli, D. & Portella-Oberli, M. *Experimental signature of cross Feshbach resonance* in 34th International conference on the physics of semiconductors (ICPS) July 29–Aug. 3, 2018 (Montpellier, France).
11. Navadeh-Toupchi, M., Takemura, N., Anderson, M., Oberli, D. & Portella-Oberli, M. *Generation of entangled photon pairs via the cross Feshbach resonance* in Annual meeting of the Swiss physical society Aug. 28–31, 2018 (Lausanne, Switzerland).